# JOURNAL OF MATHEMATICAL SCIENCES AND MODELLING

ISSN: 2636-8692

VOLUME VII
ISSUE I

VOLUME VII ISSUE I
ISSN 2636-8692

April 2024
http://dergipark.gov.tr/jmsm

# JOURNAL OF MATHEMATICAL SCIENCES AND MODELLING

# Contents

*Journal of Mathematical Sciences and Modelling*, 7(1) (2024) 1-13
*Research Article*

**Journal of Mathematical Sciences and Modelling**

*Journal Homepage: www.dergipark.gov.tr/jmsm*
*ISSN 2636-8692*
*DOI: http://dx.doi.org/10.33187/jmsm.1341741*

# Analyses of the SIR Epidemic Model Including Treatment and Immigration

**Özlem Ak Gümüş[1*], Amirtharaj George Maria Selvam[2], Narin Kilinç[3] and Rajendran Janagaraj[4]**

[1]*Department of Mathematics, Faculty of Arts and Sciences, Adıyaman University, Adiyaman, Türkiye.*
[2]*Department of Mathematics, Sacred Heart College, Tirupattur, Tamil Nadu, India.*
[3]*Department of Mathematics, Science Institute, Adıyaman University, Adiyaman, Türkiye.*
[4]*Department of Mathematics, Faculty of Engineering, Karpagam Academy of Higher Education, Coimbatore, Tamil Nadu, India.*
[*]*Corresponding author*

**Article Info**

***Keywords:*** *Flip bifurcation, Immigration, SIR model, Stability*
***2010 AMS:*** *39A13, 39A28, 39A30, 92D30*
***Received:*** *11 August 2023*
***Accepted:*** *12 December 2023*
***Available online:*** *5 February 2024*

**Abstract**

This paper aims to examine the dynamics of a variation of a nonlinear SIR epidemic model. We analyze the complex dynamic nature of the discrete-time SIR epidemic model by discretizing a continuous SIR epidemic model subject to treatment and immigration effects with the Euler method. First of all, we show the existence of equilibrium points in the model by reducing the three-dimensional system to the two-dimensional system. Next, we show the stability conditions of the obtained positive equilibrium point and the visibility of flip bifurcation. A feedback control strategy is applied to control the chaos occurring in the system after a certain period of time. We also perform numerical simulations to support analytical results. We do all these analyses for models with and without immigration and show the effect of immigration on dynamics.

## 1. Introduction

Mathematical models describing epidemics affecting population dynamics are often expressed with differential equations or difference equations [1–3]. The models of differential equations are used to describe situations where change is continuous. Analysis of continuous-time epidemic models has been studied by many researchers [4–9]. If the change is discrete, it would be more appropriate to use difference equations for modelling. Moreover, these equations provide a more realistic approach to describe events with different characteristic processes, while retaining the essential properties of the corresponding continuous time models, [10–29]. For this purpose, we provide more recent articles as references [30–32]. When a parameter of the model is changed, the stability behavior of the model may change. New stable points may emerge or existing points may disappear. Changes in the topological or qualitative structure of a dynamic system are determined using bifurcation theory [33, 34]. Sometimes, the existence of bifurcation behavior may be detected without the need for deep analysis [14, 22].
Wang [4] analyzed the following model, and showed that there is bifurcation depending on the size of the treatment capacity:

$$\begin{aligned} \frac{dS}{dt} &= A - dS - \lambda SI \\ \frac{dI}{dt} &= \lambda SI - (d+\gamma+\varepsilon)I - T(I) \\ \frac{dR}{dt} &= \gamma I + T(I) - dR. \end{aligned} \tag{1.1}$$

In this model (1.1), $S-$ sensitive individuals who have not been infected with the disease but are susceptible to the disease; $I-$ infected individuals who have contracted the disease and infect others; and $R-$ individuals who have the disease and but have recovered. $A, d, \gamma, \varepsilon, \lambda$ are positive parameters. $A-$ individuals added to the population by birth, $d-$ natural mortality rate in the population, $\gamma-$ natural recovery

***Email addresses and ORCID numbers*: akgumus@adiyaman.edu.tr, 0000-0003-2610-8565 (Ö. Ak Gümüş), agmshc@gmail.com, 0000-0003-2004-3537 (A. G. Maria Selvam), narinkurt85@hotmail.com, 0000-0002-6281-6780 (N. Kilinç), janagarajtk@gmail.com, 0000-0002-9811-078X (R. Janagaraj)**
**Cite as "Ö. Ak Gümüş, A. G. Maria Selvam, N. Kilinç, R. Janagaraj, *Analyses of the SIR epidemic model including treatment and immigration*, J. Math. Sci. Model., 7(1) (2024), 1-13"**

rate of infected individuals, $\varepsilon-$ disease-related mortality rate, $\lambda-$ infection coefficient. In study [35], local stability and bifurcation analyses were studied by transforming a continuous SIR epidemic model given in study [4] into a discrete-time system by using forward Euler method as follows:

$$\begin{aligned} S_{t+1} &= S_t + \delta\left(A - dS_t - \lambda S_t I_t\right) \\ I_{t+1} &= I_t + \delta\left(\lambda S_t I_t - zI_t - kI_t\right) \end{aligned} \tag{1.2}$$

where $z = d+\gamma+\varepsilon$ is the sum of natural death, recovery, and death from disease, respectively. $T(I) = kI$ is the treatment function such that $0 \le I \le I_0$ and $k$ is a positive parameter. In this study, we will consider the following discrete-time model that we developed under the given immigration effect:

$$\begin{aligned} S_{t+1} &= S_t + \delta\left(A - dS_t - \lambda S_t I_t + pS_t\right) \\ I_{t+1} &= I_t + \delta\left(\lambda S_t I_t - zI_t - kI_t + qI_t\right) \end{aligned} \tag{1.3}$$

where $pS_t-$ immigration effect on susceptible individuals and $qI_t-$ immigration effect on infected individuals. In this article, our aim is to examine the dynamics of model (1.3) subject to immigration by briefly recalling the analysis of the model (1.2) without immigration, and then to compare dynamics of these models in order to see the effect of the immigration factor on the system (1.2). We can give references to some studies that are necessary for the basic concepts used in the analyses made throughout the study [36–38].
This article is organized as follows: Section 2 briefly mentions from the analysis of the positive equilibrium point of the model (1.2), which does not include the immigration factor. In Section 3, the equilibrium points of the model (1.3) created by including the immigration factor were obtained; and stability analyses of the obtained equilibrium points are made. Then, the flip bifurcation conditions are obtained for the positive equilibrium point. The resulting chaos was controlled in Section 4. Section 5 presents numerical simulations that validate the criteria obtained. A brief summary of the results is presented in Section 6.

## 2. Analysis of the SIR Epidemic Model (1.2)

Let us briefly recall the existence of equilibrium points of the system (1.2), stability of the positive equilibrium point, and flip bifurcation condition (see [35]).

**Remark 2.1.** *The model (1.2) has two equilibrium points such that* $(S_*, I_*) = \left(\frac{A}{d}, 0\right)$ *and* $(S^*, I^*) = \left(\frac{k+z}{\lambda}, \frac{A}{k+z} - \frac{d}{\lambda}\right)$.

**Remark 2.2.** *Assume that* $\frac{A\lambda}{k+z} > d$. *Regarding the dynamics of the positive equilibrium point* $(S^*, I^*) = \left(\frac{k+z}{\lambda}, \frac{A}{k+z} - \frac{d}{\lambda}\right)$, *the followings are true:*

**Proposition 2.3.** *If* $\delta < \frac{A\lambda}{(k+z)(A\lambda - d(k+z))} - \sqrt{\frac{4d(k+z)^3 + A\lambda(-4(k+z)^2 + A\lambda)}{(k+z)^2(d(k+z) - A\lambda)^2}}$ *is provided such that* $\frac{A\lambda(4(k+z)^2 - A\lambda)}{4(k+z)^3} < d$, *the* $(S^*, I^*)$ *is locally asymptotically stable.*

**Proposition 2.4.** *For* $\delta = \frac{4(k+z)}{A\lambda + \sqrt{4d(k+z)^3 + A\lambda(-4(k+z)^2 + A\lambda)}}$, *there can be flip bifurcation such that* $B = \frac{\delta\lambda A}{k+z} \neq 2, 4$.

## 3. Analysis of the SIR Epidemic Model (1.3)

In this section, the aim is to discretize by adding immigration parameters to the model discussed in [4]; and then to examine the dynamics of the obtained discrete-time model. Thus, the continuous SIR epidemic model, based on different rates of immigration of both susceptible and diseased individuals, is as follows:

$$\begin{aligned} \frac{dS}{dt} &= A - dS - \lambda SI + pS \\ \frac{dI}{dt} &= \lambda SI - (d+\gamma+\varepsilon)I - T(I) + qI \\ \frac{dR}{dt} &= \gamma I - kI - dR. \end{aligned}$$

It is sufficient to consider the following model reduced to $2-$dimensions, since the first two variables are independent of the variable $R$

$$\begin{aligned} \frac{dS}{dt} &= A - dS - \lambda SI + pS \\ \frac{dI}{dt} &= \lambda SI - (d+\gamma+\varepsilon)I - T(I) + qI. \end{aligned}$$

Now, if we use the forward Euler method in the continuous SIR epidemic model such that, $z = d+\gamma+\varepsilon$ and $T(I) = kI$; we get discretized the system as follows:

$$\begin{aligned} S_{t+1} &= S_t + \delta\left(A - dS_t - \lambda S_t I_t + pS_t\right) \\ I_{t+1} &= I_t + \delta\left(\lambda S_t I_t - zI_t - kI_t + qI_t\right) \end{aligned}$$

with $\frac{dS}{dt} \approx \frac{S_{t+1} - S_t}{\delta}$ and $\frac{dI}{dt} \approx \frac{I_{t+1} - I_t}{\delta}$. The following Lemma is useful for analysis of the positive equilibrium point.

**Lemma 3.1.** *[9, 25] Let $F(\lambda)=\lambda^2+B\lambda+C$ be a quadratic polynomial with real coefficients. Suppose that this polynomial has roots $\lambda_1$, $\lambda_2$, and $F(1)>0$. Then the following statements apply:*

*(i)* $|\lambda_1|<1$ *and* $|\lambda_2|<1 \Leftrightarrow F(-1)>0$, *and* $C<1$. *(In this case, the equilibrium point is stable.)*
*(ii)* $\lambda_1=-1$ *and* $\lambda_2\neq 1 \Leftrightarrow F(-1)=0$ *and* $B\neq 0,2$. *(In this case, flip bifurcation may occur.)*

Then we can give the following analyses for this model.

### 3.1. Local stability

We see that the model (1.3) has two equilibrium points $(S_*,I_*)=\left(\frac{A}{d-p},0\right)$ and $(S_*,I_*)=\left(\frac{k+z-q}{\lambda},\frac{A\lambda+(p-d)(k+z-q)}{(k+z-q)\lambda}\right)$. Let us now examine the local asymptotic stability conditions of the positive equilibrium point $(S^*,I^*)$. For this, let us take

$$f(S)=S+\delta\left(A-dS-\lambda SI+pS\right)$$
$$g(I)=I+\delta\left(\lambda SI-zI-kI+qI\right).$$

So we can write the following Jacobian matrix:

$$J(S,I)=\begin{bmatrix} f_S(S,I) & f_I(S,I)\\ g_S(S,I) & g_I(S,I)\end{bmatrix}=\begin{bmatrix} 1+\delta\left(-d-\lambda I+p\right) & -\delta\lambda S\\ \delta\lambda I & 1+\delta\left(\lambda S-z-k+q\right)\end{bmatrix}.$$

The Jacobian matrix evaluated around the positive equilibrium point $(S^*,I^*)$ is given by

$$\begin{aligned} J(S^*,I^*)&=J\left(\frac{k+z-q}{\lambda},\frac{A\lambda+(p-d)(k+z-q)}{(k+z-q)\lambda}\right)\\ &=\begin{bmatrix} 1-\dfrac{\delta\lambda A}{k+z-q} & -\delta(k+z-q)\\ \delta\left(\dfrac{A\lambda+(k+z-q)(p-d)}{k+z-q}\right) & 1\end{bmatrix},\end{aligned}$$

where $det(J)=1-\frac{\delta\lambda A}{k+z-q}+\delta^2\lambda A+\delta^2(p-d)(k+z-q)$ and $Trace(J)=2-\frac{\delta\lambda A}{k+z-q}$. Then the characteristic polynomial corresponding to the Jacobian matrix has the form:

$$F(\mu)=\mu^2-\left(2-\frac{\delta\lambda A}{k+z-q}\right)\mu+1-\frac{\delta\lambda A}{k+z-q}+\delta^2(\lambda A+(p-d)(k+z-q))$$

and the roots of this polynomial are found:

$$\mu_{1,2}=1-\frac{\delta\lambda A}{2(k+z-q)}\pm\frac{\delta}{2(k+z-q)}\sqrt{4(d-p)(k-q+z)^3-4(k-q+z)^2A\lambda+A^2\lambda^2}.$$

For the stability of the equilibrium point, the magnitudes of these two eigenvalues must remain less than 1. To determine the conditions on the parameters, we first make use of the following conditions:

$$|\lambda_1|<1 \quad \text{and} \quad |\lambda_2|<1 \Leftrightarrow F(-1)>0, F(1)>0 \quad \text{and} \quad C<1.$$

**Proposition 3.2.** $F(1)>0\Rightarrow F(1)=\delta^2\left(A\lambda+(p-d)(k+z-q)\right)>0$. *Thus* $\frac{A\lambda}{k+z-q}>d-p>0$ *must be provided such that* $0<q\leq z$.

**Proposition 3.3.**

$$F(-1)>0\Rightarrow F(-1)=\frac{4(k+z-q)-2\delta\lambda A+\delta^2(\lambda A(k+z-q)+(k+z-q)^2(p-d))}{k+z-q}>0.$$

*If this inequality is solved, we have*

$$\delta_1<\frac{\lambda A}{(k+z-q)(\lambda A+(p-d)(k-q+z))}-\sqrt{\frac{4(d-p)(k-q+z)^3-4(k-q+z)^2A\lambda+A^2\lambda^2}{(k+z-q)^2((d-p)(k-q+z)-A\lambda)^2}}.$$

*or*

$$\delta_2>\frac{\lambda A}{(k+z-q)(\lambda A+(p-d)(k-q+z))}+\sqrt{\frac{4(d-p)(k-q+z)^3-4(k-q+z)^2A\lambda+A^2\lambda^2}{(k+z-q)^2((d-p)(k-q+z)-A\lambda)^2}}.$$

*such that* $\frac{A\lambda(4(k+z-q)^2-A\lambda)}{4(k+z-q)^3}+p<d$.

**Proposition 3.4.**

$$C<1\Rightarrow C=\frac{(k+z-q)-\delta\lambda A+\delta^2(\lambda A(k+z-q)+(k+z-q)^2(p-d))}{k+z-q}<1.$$

*If this inequality is solved, we have*

$$\delta<\frac{A\lambda}{(k+z-q)(A\lambda+(p-d)(k+z-q))}.$$

**Theorem 3.5.** *Assume that* $\frac{A\lambda}{k+z-q} > d-p > 0$. *If* $\frac{A\lambda(4(k+z-q)^2 - A\lambda)}{4(k+z-q)^3} + p < d$ *and*

$$\delta < \frac{\lambda A}{(k+z-q)(\lambda A + (p-d)(k-q+z))} - \sqrt{\frac{4(d-p)(k-q+z)^3 - 4(k-q+z)^2 A\lambda + A^2\lambda^2}{(k+z-q)^2((d-p)(k-q+z) - A\lambda)^2}}$$

*are provided, the positive equilibrium point of the model (1.3) is locally asymptotic stable.*

### 3.2. Flip bifurcation

Let's $\frac{A\lambda}{k+z-q} > d-p > 0$. We know that when $B \neq 0, 2$ and $F(-1) = 0$, flip bifurcation can occur. Therefore, we will consider these conditions such that $B = -trace(J)$, $C = det(J)$.

**Proposition 3.6.** *From the condition* $F(-1) = 0$, *we get the roots*

$$\delta_{1,2} = \frac{4(k-q+z)}{\lambda A \pm \sqrt{4(d-p)(k-q+z)^3 - 4(k-q+z)^2 A\lambda + A^2\lambda^2}}.$$

**Proposition 3.7.** *From the condition* $B \neq 0$, *we reach*

$$B = -trace(J) = -\left(2 - \frac{\delta\lambda A}{k+z-q}\right) \quad and \quad -trace(J) \neq 0 \Leftrightarrow \delta \neq \frac{2(k+z-q)}{\lambda A}.$$

**Proposition 3.8.** *From the condition* $B \neq 2$, *we obtain*

$$B = -trace(J) = -\left(2 - \frac{\delta\lambda A}{k+z-q}\right) \quad and \quad -trace(J) \neq 2 \Leftrightarrow \delta \neq \frac{4(k+z-q)}{\lambda A}.$$

**Theorem 3.9.** *If the condition*

$$\delta = \frac{4(k-q+z)}{\lambda A + \sqrt{4(d-p)(k-q+z)^3 - 4(k-q+z)^2 A\lambda + A^2\lambda^2}}$$

*are met, the model (1.3) has flip bifurcation such that* $\delta \neq \frac{2(k+z-q)}{\lambda A}$ *and* $\delta \neq \frac{4(k+z-q)}{\lambda A}$.

If

$$\delta = \delta_{FB} = \frac{4(k-q+z)}{\lambda A + \sqrt{4(d-p)(k-q+z)^3 - 4(k-q+z)^2 A\lambda + A^2\lambda^2}}$$

then $\lambda_1 = -1$ with

$$|\lambda_2| \neq 1. \tag{3.1}$$

These conditions can be presented by the following set

$$FB_{(S_*,I_*)} = \left\{ A, d, k, z, \lambda, p, q, \delta \in \mathbb{R}^+ : \delta = \delta_{FB} = \frac{4(k-q+z)}{\lambda A + \sqrt{4(d-p)(k-q+z)^3 - 4(k-q+z)^2 A\lambda + A^2\lambda^2}}, |\lambda_2| \neq 1 \right\}.$$

Using the transformation $u = x - \frac{k-q+z}{\lambda}$, $v = y - \frac{A}{k-q+z} - \frac{p-d}{\lambda}$, the fixed point $(S_*, I_*)$ is shifted to the origin. Therefore, we obtain

$$\begin{pmatrix} u \\ v \end{pmatrix} \to J_{(S_*,I_*)} \begin{pmatrix} u \\ v \end{pmatrix} + \begin{pmatrix} F_1(u,v) \\ F_2(u,v) \end{pmatrix}$$

where

$$F_1(u,v) = -\delta\lambda uv$$

$$F_2(u,v) = \delta\lambda uv$$

such that $U = (u,v)^T$. From there, the system (1.3) can be written as

$$(U_{n+1}) \to J_{(S_*,I_*)}(U_n) + \frac{1}{2}B(u_n,u_n) + \frac{1}{6}C(u_n,u_n,u_n) + O(\|u_n\|^4),$$

with the multilinear vector functions of $u, v, w \in \mathbb{R}^2$ :

$$B(u,v) = \begin{pmatrix} B_1(u,v) \\ B_2(u,v) \end{pmatrix}$$

and

$$C(u,v,w) = \begin{pmatrix} C_1(u,v,w) \\ C_2(u,v,w) \end{pmatrix}.$$

These vectors are expressed by

$$\begin{aligned} B_1(u,v) &= \sum_{j,k=1}^{2} \frac{\partial^2 F_1}{\partial\xi_j \partial\xi_k} |_{\xi=0}\, u_j v_k = -\delta\lambda(u_2 v_1 + u_1 v_2) \\ B_2(u,v) &= \sum_{j,k=1}^{2} \frac{\partial^2 F_2}{\partial\xi_j \partial\xi_k} |_{\xi=0}\, u_j v_k = \delta\lambda(u_2 v_1 + u_1 v_2) \end{aligned}$$

$$\begin{aligned} C_1(u,v,w) &= \sum_{j,k=1}^{2} \frac{\partial^3 F_1}{\partial\xi_j \partial\xi_k \xi_l} |_{\xi=0}\, u_j v_k w_l = 0 \\ C_2(u,v,w) &= \sum_{j,k=1}^{2} \frac{\partial^3 F_2}{\partial\xi_j \partial\xi_k \xi_l} |_{\xi=0}\, u_j v_k w_l = 0 \end{aligned}$$

and $\delta = \delta_{FB}$. Let $q, p \in \mathbb{R}^2$ be eigenvectors of $J_{(S_*,I_*)}(\delta_{FB})$ and transposed matrix $J^T_{(S_*,I_*)}(\delta_{FB})$ respectively for $\lambda_1(\delta_{FB}) = -1$. Then, we have $J_{(S_*,I_*)}(\delta_{FB})q = -q$ and $J^T_{(S_*,I_*)}(\delta_{FB})p = -p$. We use standard scalar product $< p, q >= p_1 q_1 + p_2 q_2$ in $\mathbb{R}^2$ in order to normalize $p$ with respect to $q$, such that $< p, q >= 1$. To determine the direction of the flip bifurcation, we need to get the sign of the coefficient $c(\delta_{FB})$ as follows:

$$c(\delta_{FB}) = \frac{1}{6} < p, C(q,q,q) > -\frac{1}{2} < p, B(q,(J-I)^{-1}B(q,q) > .$$

The following theorem gives the result on flip bifurcation regarding the coefficient of the critical normal form.

**Theorem 3.10.** *If (3.1) becomes valid, $c(\delta_{FB}) \neq 0$, and the parameter $a$ changes its value around $\delta_{FB}$, then the system (1.3) undergoes a flip bifurcation at positive coexistence fixed point $(S_*, I_*)$. Furthermore, if $c(\delta_{FB}) > 0$ ($c(\delta_{FB}) < 0$), then the period 2 orbits that bifurcate from $(S_*, I_*)$ are stable (unstable).*

## 4. Chaos Control

In this section, we will use the chaos control method to control the chaos that occurs in systems (1.2) and (1.3). Chaos theory, a method of qualitative and quantitative analysis for investigating the behavior of dynamic systems, explains how a small change in one state of a nonlinear system can lead to large differences in a later state. In some cases, long-term prediction of the behavior of a chaotic system may become impossible, especially due to sensitive dependence on initial conditions, and even the deterministic nature of the system does not make them predictable. Due to the infinite number of unstable periodic orbits, system behavior becomes unpredictable. Control of chaos is the stabilization of one of the selected unstable periodic orbits through small system perturbations. The aim is to make the chaotic behavior more stable and predictable by directing the trajectories towards the desired position by adding an appropriate control parameter to the system. A state feedback control method [16, 18, 36] is used to stabilize chaotic orbit at an unstable fixed point of the system (1.2) and (1.3).

### 4.1. Chaos control analysis for the (1.2) model

The controlled form of the system (1.2) is obtained by incorporating a feedback control parameter as the control force into system (1.2). So we define the controller of the system (1.2) as follows:

$$\begin{aligned} S_{t+1} &= S_t + \delta\,(A - dS_t - \lambda S_t I_t) + U_t \\ I_{t+1} &= I_t + \delta\,(\lambda S_t I_t - zI_t - kI_t) \end{aligned}$$

where $U_t$ is a control force such that $U_t = -p_1\,(S_t - S^*) - p_2\,(I_t - I^*)$. The Jacobian matrix at the positive equilibrium point of this system is

$$J(S^*, I^*) = J\left(\frac{k+z}{\lambda}, \frac{A\lambda - (k+z)d}{(k+z)\lambda}\right) = \begin{bmatrix} 1 - \dfrac{\delta A\lambda}{k+z} - p_1 & -\delta(k+z) - p_2 \\ \delta\left(\dfrac{A\lambda - (k+z)d}{k+z}\right) & 1 \end{bmatrix}$$

and the characteristic equation obtained through the Jacobian matrix is written as;

$$F(\mu) = \mu^2 - \left(2 - \frac{\delta A\lambda}{k+z} - p_1\right)\mu + 1 - \frac{\delta A\lambda}{k+z} - p_1 + \delta^2(A\lambda - d(k+z)) + \delta p_2\left(\frac{A\lambda - d(k+z)}{k+z}\right)$$

and $\mu_{1,2}$ be the eigenvalues of this characteristic equation. Then we have

$$\mu_1 + \mu_2 = 2 - \frac{\delta A\lambda}{k+z} - p_1$$

and

$$\mu_1\mu_2 = 1 - \frac{\delta A\lambda}{k+z} - p_1 + \delta^2(A\lambda - d(k+z)) + \delta p_2\left(\frac{A\lambda - d(k+z)}{k+z}\right).$$

We must solve the equations $\mu_1\mu_2 = 1, \mu_1 = 1$ and $\mu_1 = -1$. So, we get the marginal line $I_1, I_2$ and $I_3$ as follows:

$$\begin{aligned}
\mu_1\mu_2 = det(J) = 1 \Rightarrow I_1 &= -\frac{\delta A\lambda}{k+z} - p_1 + \delta^2(A\lambda - d(k+z)) + \delta p_2\left(\frac{A\lambda - d(k+z)}{k+z}\right)\\
\mu_1 = 1 \Rightarrow I_2 &= \delta^2(A\lambda - d(k+z)) + \delta p_2\left(\frac{A\lambda - d(k+z)}{k+z}\right)\\
\mu_1 = -1 \Rightarrow I_3 &= 4 - \frac{2\delta A\lambda}{k+z} - 2p_1 + \delta^2(A\lambda - d(k+z)) + \delta p_2\left(\frac{A\lambda - d(k+z)}{k+z}\right)
\end{aligned}$$

The region bounded by $I_1, I_2$ and $I_3$ gives stable eigenvalues of magnitude less than 1.

### 4.2. Chaos control analysis for the (1.3) model

We define the controller of the system (1.3) as follows:

$$\begin{aligned}
S_{t+1} &= S_t + \delta\left(A - dS_t - \lambda S_t I_t + pS_t\right) + U_t\\
I_{t+1} &= I_t + \delta\left(\lambda S_t I_t - zI_t - kI_t + qI_t\right)
\end{aligned}$$

where $U_t$ is a control force such that $U_t = -p_1\left(S_t - S^*\right) - p_2\left(I_t - I^*\right)$. The Jacobian matrix at the positive equilibrium point of this system is

$$\begin{aligned}
J(S^*, I^*) &= J\left(\frac{k+z-q}{\lambda}, \frac{A\lambda - (p-d)(k+z-q)}{(k+z-q)\lambda}\right)\\
&= \begin{bmatrix} 1 - \dfrac{\delta A\lambda}{k+z-q} - p_1 & -\delta(k+z-q) - p_2\\ \delta\left(\dfrac{A\lambda - (p-d)(k+z-q)}{k+z-q}\right) & 1 \end{bmatrix}.
\end{aligned}$$

The characteristic equation we get by means of the Jacobian matrix is

$$F(\mu) = \mu^2 - trace(J) + det(J),$$

where,

$$trace(J) = 2 - \frac{\delta A\lambda}{k+z-q} - p_1$$

and

$$det(J) = 1 - \frac{\delta A\lambda}{k+z-q} - p_1 + \delta^2(A\lambda - (p-d)(k+z-q)) + \delta p_2\left(\frac{A\lambda - (p-d)(k+z-q)}{k+z-q}\right).$$

The eigenvalues of the characteristic equation $F(\mu)$ are $\mu_1$ and $\mu_2$. By providing the conditions $\mu_1\mu_2 = 1$, $\mu_1 = 1$ and $\mu_1 = -1$, we have the marginal line $I_1, I_2$ and $I_3$ as follows:

$$\begin{aligned}
I_1 &= -\frac{\delta A\lambda}{k+z-q} - p_1 + \delta^2(A\lambda - (p-d)(k+z-q)) + \delta p_2\left(\frac{A\lambda - (p-d)(k+z-q)}{k+z-q}\right)\\
I_2 &= \delta^2(A\lambda - (p-d)(k+z-q)) + \delta p_2\left(\frac{A\lambda - (p-d)(k+z-q)}{k+z-q}\right)\\
I_3 &= 4 - \frac{2\delta A\lambda}{k+z-q} - 2p_1 + \delta^2(A\lambda - (p-d)(k+z-q)) + \delta p_2\left(\frac{A\lambda - (p-d)(k+z-q)}{k+z-q}\right).
\end{aligned}$$

The region bounded by $I_1, I_2$ and $I_3$ gives stable eigenvalues of magnitude less than 1.

## 5. Numerical Simulations

We give the following examples to verify our theoretical results. Time series, phase and bifurcation graphs are presented by using Matlab program (see also the Mathematical Software program [39, 40]).

**Example 5.1.** *We can write system (1.2) as*

$$\begin{aligned}
S_{t+1} &= S_t + \delta\left(3 - 0.1S_t - S_t I_t\right)\\
I_{t+1} &= I_t + \delta I_t\left(S_t - 0.3 - 0.2\right)
\end{aligned} \tag{5.1}$$

*with parameter values $A = 3, \lambda = 1, k = 0.2, z = 0.3, d = 0.1$. The presented graphs show the dynamic behavior of the system (5.1) with the initial condition $(S_0, I_0) = (2.1, 0.9)$.*

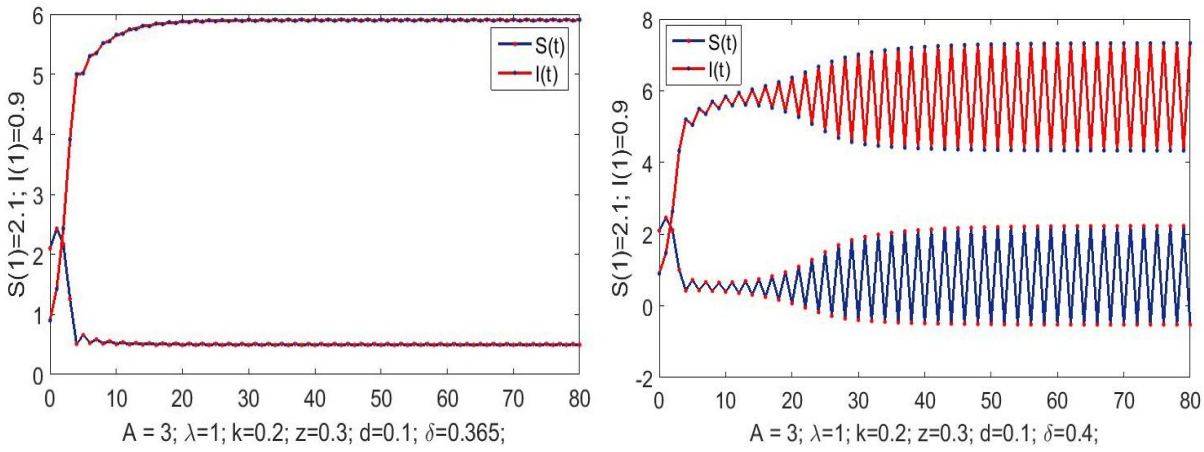


**Figure 5.1:** Time Series Graph of System (5.1) when (a) $\delta = 0.365$ (b) $\delta = 0.4$

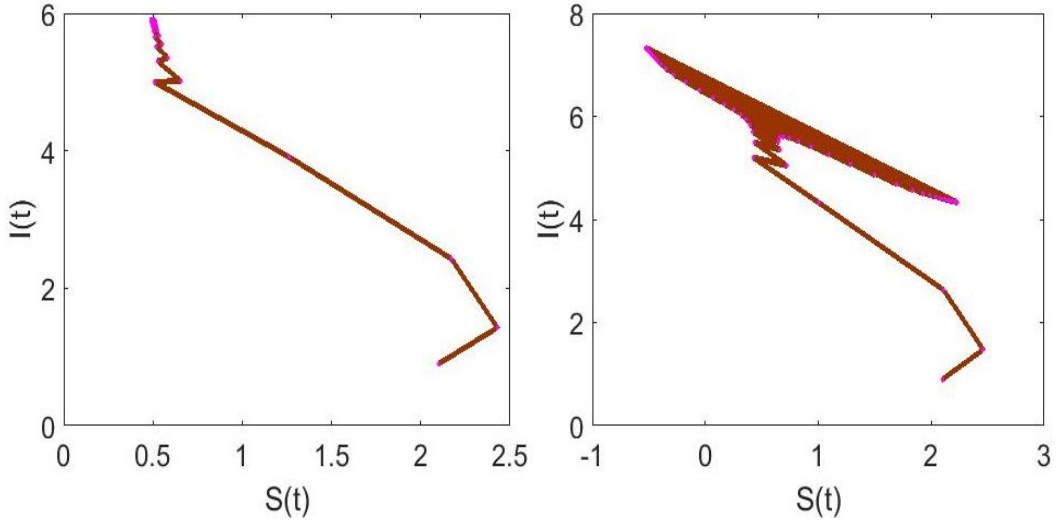


**Figure 5.2:** Phase Graph of System (5.1)

While we observe that the system (5.1) is locally asymptotic stable ($\delta = 0.365 < 0.366$) with the appropriate parameter values in Figure 5.1-(a), we see that the system (5.1) is unstable ($\delta = 0.4 > 0.366$) when the value $\delta$ is increased in Figure 5.1-(b). Figure 5.2, corresponding to Figure 5.1 with the same parameter values, is the phase portraits of the system (5.1).
Also, in Figure 5.3, we present the flip bifurcation graph of the system (5.1) for the parameter values $A = 3, \lambda = 1, k = 0.2, z = 0.3, d = 0.1$ and $0.3 < \delta < 0.5$. Here, we can see that flip bifurcation occurs at $(S_*, I_*)$ when the parameter changes in a small neighborhood of $\delta_{FB} = 0.366322$. The computation yields $(S_*, I_*) = (0.5, 5.9)$. The Jacobian matrix is $J = \begin{bmatrix} -1.19793 & -0.183161 \\ 2.1613 & 1 \end{bmatrix}$. The eigenvalues are $\lambda_1 = -1$, and $\lambda_2 = 0.802067$ such that $|\lambda_2| \neq 1$. This defines that the fixed point $(S_*, I_*)$ is stable for $\delta < 0.366322$, and there exists a period doubling phenomena for $\delta > 0.366322$. By direct calculations, we can write

$$\begin{aligned} F_1(u,v) &= -0.366322uv \\ F_2(u,v) &= 0.366322uv \\ B_1(u,v) &= -0.366322(u_2v_1 + u_1v_2) \\ B_2(u,v) &= 0.366322(u_2v_1 + u_1v_2) \\ C_1(u,v,w) &= 0 \\ C_2(u,v,w) &= 0 \end{aligned}$$

$$\begin{aligned} B(q,q) &= \begin{pmatrix} 0.365223 \\ -0.365223 \end{pmatrix} \\ C(q,q,q) &= \begin{pmatrix} 0 \\ 0 \end{pmatrix}. \end{aligned}$$

and $p \sim (-0.733965, -0.679187)^T$, $q \sim (-0.679187, 0.733965)^T$. Here, $p \sim (-4.40731.10^{15}, -4.07838.10^{15})^T$ is obtained as normalized vector according to $q$, such that $< p, q >= 1$. Upon the necessary calculations, we obtain $c(\delta_{FB}) = 0.000285917 > 0$. The period-2 orbits that bifurcate from $(S_*, I_*)$ are stable.

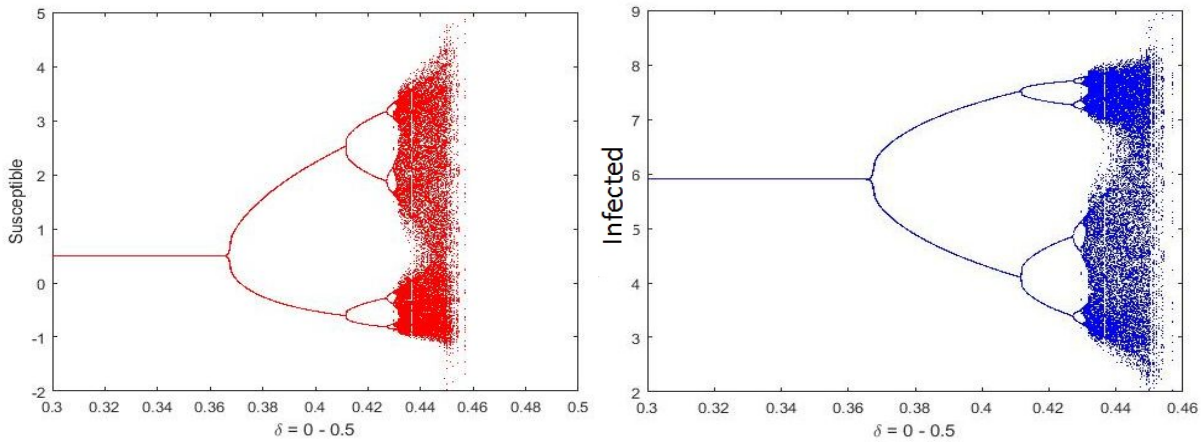


**Figure 5.3:** Flip Bifurcation Graph of System (5.1).

**Example 5.2.** *We can write system (1.3) as*

$$\begin{aligned} S_{t+1} &= S_t + \delta\,(3 - 0.1S_t - S_tI_t + 0.01S_t) \\ I_{t+1} &= I_t + \delta I_t\,(S_t - 0.3 - 0.2 + 0.1) \end{aligned} \tag{5.2}$$

*with parameter values* $A = 3, \lambda = 1, k = 0.2, z = 0.3, d = 0.1, q = 0.1, p = 0.01$. *The following graphs are obtained for the dynamic behavior of the system (5.2) with* $(S_0, I_0) = (2.1, 0.9)$. *The time series and phase diagram graphs are displayed in Figures 5.4 & 5.5. In Figure 5.8, we present the flip bifurcation graph of the system (5.2) for the parameter values* $A = 3, \lambda = 1, k = 0.2, z = 0.3, d = 0.1, p = 0.01, q = 0.1$ *and* $0.25 < \delta < 0.35$. *Here, it can seen that flip bifurcation occurs at* $(S_*, I_*)$ *when the parameter changes in a small neighborhood of* $\delta_{FB} = 0.282428$. *The computation yields* $(S_*, I_*) = (0.4, 7.41)$. *The Jacobian matrix is* $J = \begin{bmatrix} -1.1181 & -0.112971 \\ 2.08279 & 1 \end{bmatrix}$. *The eigenvalues are* $\lambda_1 = -1$, *and* $\lambda_2 = 0.881788$ *such that* $|\lambda_2| \neq 1$. *So, the fixed point* $(S_*, I_*)$ *is stable for* $\delta < 0.282428$ *and there exists a period doubling phenomena for* $\delta > 0.282428$. *By direct calculations, we obtain*

$$\begin{aligned} F_1(u,v) &= -0.282428uv \\ F_2(u,v) &= 0.282428uv \end{aligned}$$

$$\begin{aligned} B_1(u,v) &= -0.282428(u_2v_1 + u_1v_2) \\ B_2(u,v) &= 0.282428(u_2v_1 + u_1v_2) \\ C_1(u,v,w) &= 0 \\ C_2(u,v,w) &= 0 \\ B(q,q) &= \begin{pmatrix} 0.0318047 \\ -0.0318047 \end{pmatrix} \\ C(q,q,q) &= \begin{pmatrix} 0 \\ 0 \end{pmatrix} \end{aligned}$$

*and* $p \sim (-0.998408, -0.0563957)^T$, $q \sim (0.0563957, -0.998408)^T$. *Here,* $p \sim (-7.19429.10^{16}, -4.06374.10^{15})^T$ *is obtained as normalized vector according to q, such that* $< p, q >= 1$. *Upon the necessary calculations, we obtain* $c(\delta_{FB}) = -0.00204406 < 0$. *The period-2 orbits that bifurcate from* $(S_*, I_*)$ *are unstable.*

**Example 5.3.** *We can write system (1.3) as*

$$\begin{aligned} S_{t+1} &= S_t + \delta\,(3 - 0.1S_t - S_tI_t + 0.2S_t) \\ I_{t+1} &= I_t + \delta I_t\,(S_t - 0.3 - 0.2 + 0.1) \end{aligned} \tag{5.3}$$

*with parameter values* $A = 3, \lambda = 1, k = 0.2, z = 0.3, d = 0.1, q = 0.1, p = 0.2$. *The following graphs are obtained for the dynamic behavior of the system (5.2) with* $(S_0, I_0) = (2.1, 0.9)$. *The time series and phase diagram graphs are displayed in Figures 5.6 & 5.7.*

The flip bifurcation graph of the system (5.3) for the parameter values $A = 3, \lambda = 1, k = 0.2, z = 0.3, d = 0.1, p = 0.2, q = 0.1$ and $0.25 < \delta < 0.32$ exhibited in Figure 5.9. The flip bifurcation emerges at $(S_*, I_*)$ when the parameter changes in a small neighborhood of $\delta_{FB} = 0.282885$. The computation yields $(S_*, I_*) = (0.4, 7.6)$. The Jacobian matrix is $J = \begin{bmatrix} -1.12164 & -0.113154 \\ 2.14992 & 1 \end{bmatrix}$. The eigenvalues are $\lambda_1 = -1$, and $\lambda_2 = 0.878364$ such that $|\lambda_2| \neq 1$. This defines that the fixed point $(S_*, I_*)$ is stable for $\delta < 0.282885$, and there exists a period

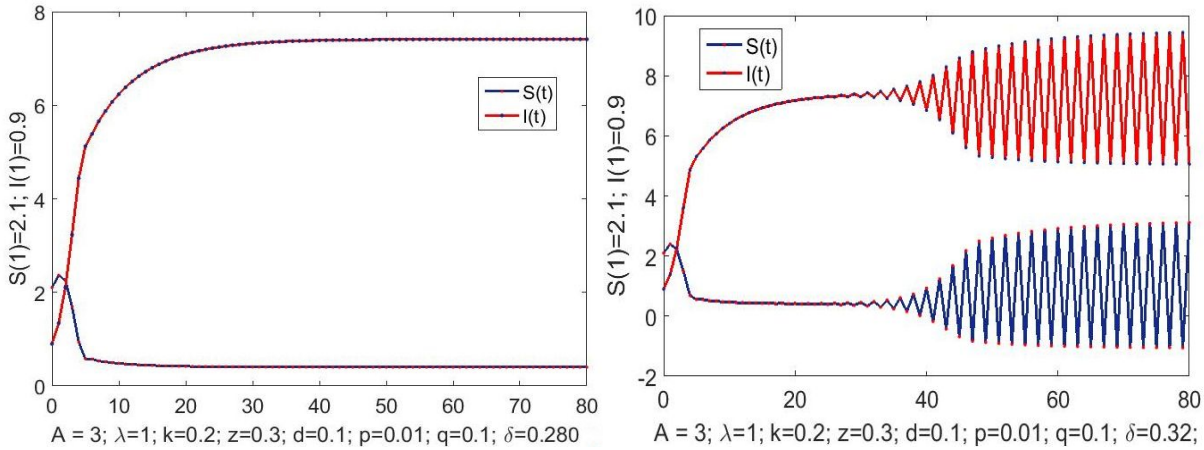


**Figure 5.4:** Time Series Graph of System (5.2) when (a) $\delta = 0.28$ (b) $\delta = 0.32$

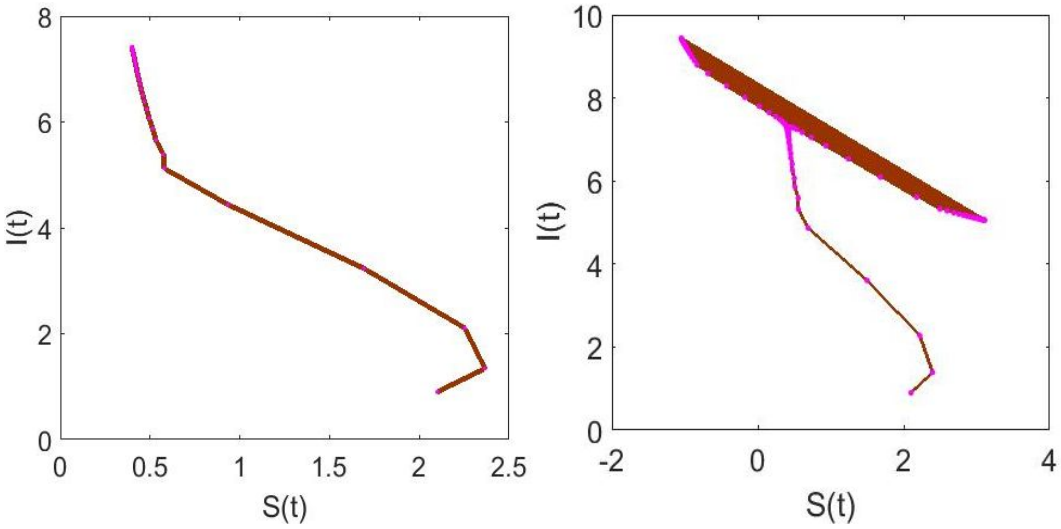


**Figure 5.5:** Phase Graph of System (5.2)

doubling phenomena for $\delta > 0.282885$. By direct calculations, we can write

$$\begin{aligned}
F_1(u,v) &= -0.282885uv \\
F_2(u,v) &= 0.282885uv \\
B_1(u,v) &= -0.282885(u_2v_1 + u_1v_2) \\
B_2(u,v) &= 0.282885(u_2v_1 + u_1v_2) \\
C_1(u,v,w) &= 0 \\
C_2(u,v,w) &= 0 \\
B(q,q) &= \begin{pmatrix} 0.0319074 \\ -0.0319074 \end{pmatrix} \\
C(q,q,q) &= \begin{pmatrix} 0 \\ 0 \end{pmatrix}.
\end{aligned}$$

and $p \sim (-0.998403, -0.0564866)^T$, $q \sim (0.0564866, -0.998403)^T$. Here, $p \sim (1.43885.10^{17}, 8.14058.10^{15})^T$ is obtained as normalized vector according to $q$, such that $< p,q >= 1$. Upon the necessary calculations, we obtain $c(\delta_{FB}) = -0.00904053 < 0$. The period-2 orbits that bifurcate from $(S_*, I_*)$ are unstable.

**Example 5.4.** *For controlled system (5.1) with parameter values* $A = 3; \lambda = 1; z = 0.3; d = 0.1; k = 0.2$ *and* $\delta = 0.44$*, we get the marginal lines are*

$$\begin{aligned}
I_1 &= -2.06888 - p_1 + 2.596p_2 \\
I_2 &= 0.57112 + 2.596p_2 \\
I_3 &= -0.70888 - 2p_1 + 2.596p_2.
\end{aligned}$$

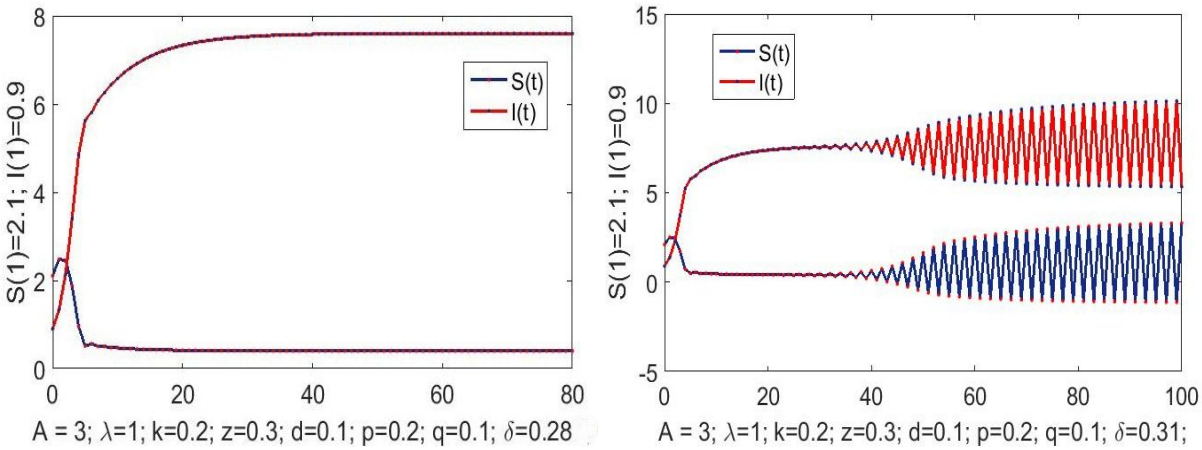


**Figure 5.6:** Time Series Graph of System (5.3) when (a) $\delta = 0.287$ (b) $\delta = 0.31$

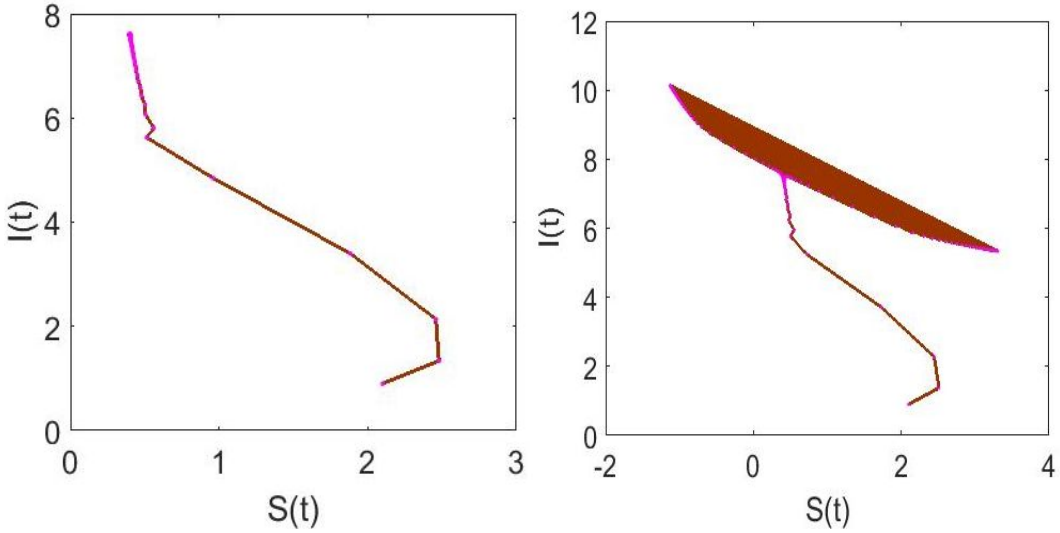


**Figure 5.7:** Phase Graph of System (5.3)

**Example 5.5.** *For controlled system (5.2) with parameter values* $A = 3; \lambda = 1; k = 0.2; z = 0.3; d = 0.1; p = 0.01; q = 0.1$ *and* $\delta = 0.34$*, we get the marginal lines are*

$$I_1 = -2.71223 - p_1 + 3.3396p_2$$
$$I_2 = 0.5877 + 3.3396p_2$$
$$I_3 = -2.01223 + 2p_1 + 3.3396p_2.$$

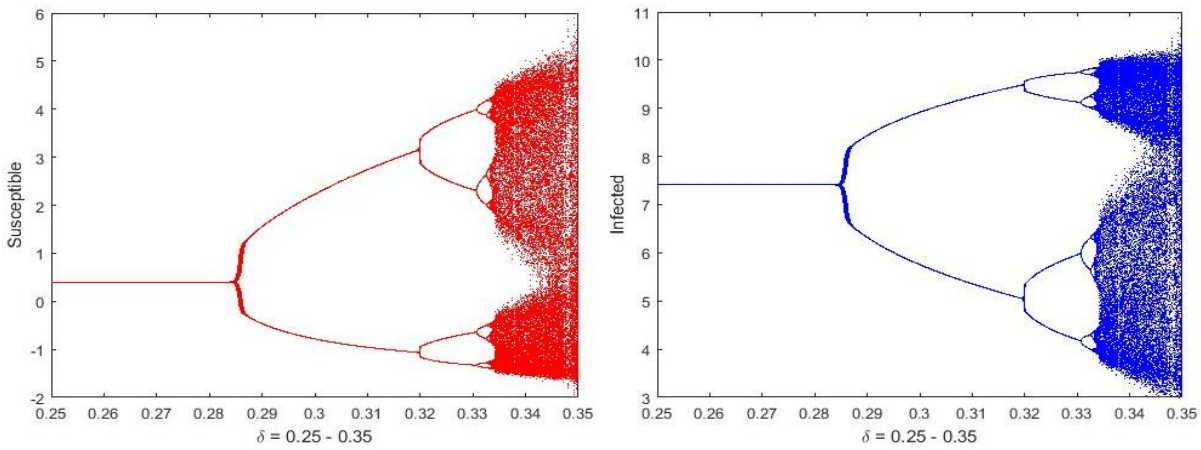


**Figure 5.8:** Flip Bifurcation Graph of System (5.2) for $0.25 < \delta < 0.35$.

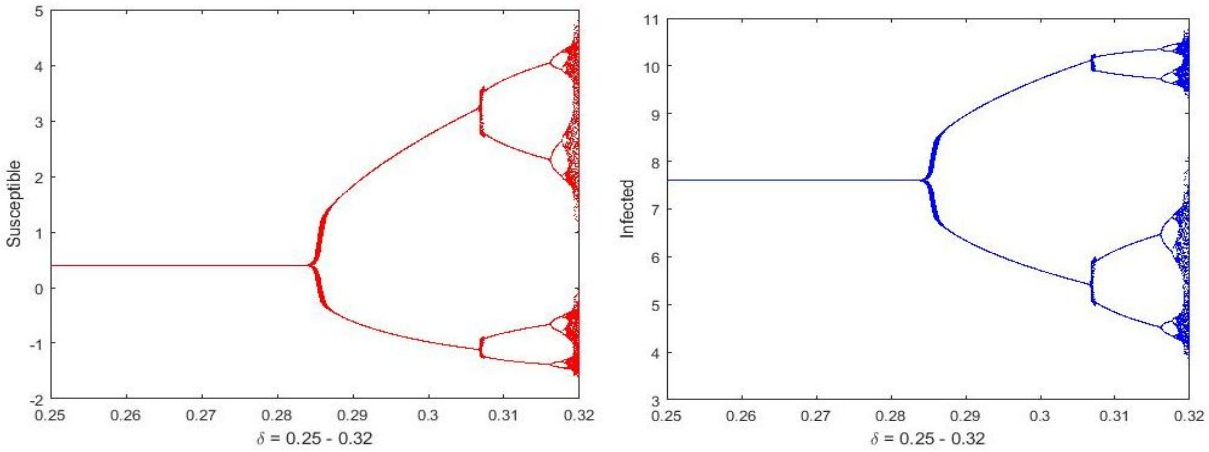


**Figure 5.9:** Flip Bifurcation Graph of System (5.3) for $0.25 < \delta < 0.32$.

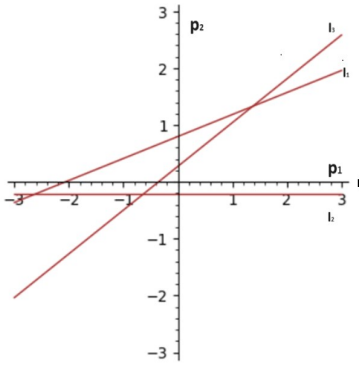


**Figure 5.10:** Chaos control lines of the system (5.1).

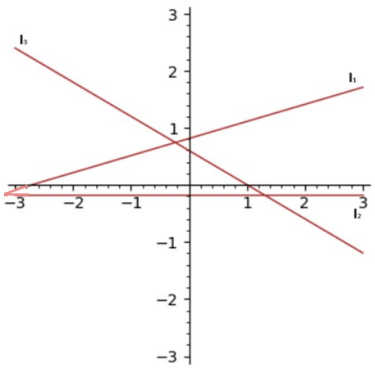

**Figure 5.11:** Chaos control lines of the system (5.2).

## 6. Conclusion

In this study, first of all, the existence of the equilibrium points of the discrete-time system (1.2), the local stability of the equilibrium points, the conditions of flip bifurcation are summarized analytically. The model (1.3) is created by adding the immigration effect to the model (1.2); and the dynamics of model (1.3) are examined. A comparison is presented for the dynamic behavior of model (1.2) and model (1.3). Finally, numerical simulations are included to support the theoretical results obtained.
Figure 5.4 and Figure 5.6 are time series graphs with immigration parameters added at different rates to susceptible individuals. Note that and bifurcation values are calculated $\delta = 0.366322$ and $\delta = 0.282428$ for without immigration and with immigration, respectively (see Figures 5.3 and 5.8). Considering Figures 5.3 and 5.8, we see that immigration parameters lead the system to faster flip bifurcation.
Finally, Figure 5.8 and Figure 5.9 show that flip bifurcation will be delayed as the number of immigration added to susceptible individuals increases. Also, Example 5.4 and Example 5.5 give chaos control lines of the system (5.1) and (5.2), respectively. The stable triangular region is determined by these marginal lines.

## Article Information

**Acknowledgements:** The authors would like to express their sincere thanks to the editor and the anonymous reviewers for their helpful comments and suggestions.

**Authors contributions:** All authors contributed equally to the writing of this paper. All authors read and approved the final manuscript.

**Conflict of interest disclosure:** No potential conflict of interest was declared by the author.



**Supporting/Supporting organizations:** No grants were received from any public, private or non-profit organizations for this research.

**Ethical approval and participant consent:** It is declared that during the preparation process of this study, scientific and ethical principles were followed and all the studies benefited from are stated in the bibliography.

**Plagiarism statement:** This article was scanned by the plagiarism program. No plagiarism detected.

**Availability of data and materials:** Not applicable.

## References

[1] F. Brauer, C. Castillo-Cavez, *Mathematical Models in Population Biology and Epidemology*, Texts in Applied Mathematics, 2001.
[2] R. M. Anderson, R. M. May, *Infectious Diseases of Humans: Dynamics and Control*, Oxford University Press, 1992.
[3] M. Martcheva, *An Introduction to Mathematical Epidemiology*, Springer, New York, 2015.
[4] W. Wang, *Backward bifurcation of an epidemic model with treatment*, Math. Biosci., **201** (2006), 58-71.
[5] A. G. Perez, E. Avila-Vales, G. E. Garcia-Almeida, *Bifurcation analysis of an SIR model with logistic growth, nonlinear incidence, and saturated treatment*, Complexity, (2019), 1–21.
[6] G. Li, W. Wang, Z. Jin, *Global stability of an SEIR epidemic model with constant immigration*, Chaos Solitons Fractals, **30** (4) (2006), 1012-1019.
[7] L. Jian-quan, Z. Juan, M. Zhi-en, *Global analysis of some epidemic models with general contact rate and constant immigration*, Appl. Math. Mech., **25** (4) (2004), 396-404.
[8] Z. A. Khan, A. L. Alaoui, A. Zeb, M. Tilioua, S. Djilali, *Global dynamics of a SEI epidemic model with immigration and generalized nonlinear incidence functional*, Results Phys., **27** (2021), 104477.
[9] A. Zeb, S. Djilali, T. Saeed, M. S. Alhodaly, N. Gul, *Global proprieties of an SIR epidemic model with nonlocal diffusion and immigration*, Results Phys., **39** (2022), 105758.
[10] A. G. M. Selvam, R. Janagaraj, S. Britto Jacob, D. Vignesh, *Stability and bifurcations of a discrete-time Prey–predator system with constant prey refuge*, J. Phys. Conf. Ser., **2070** 012068 (2021), 1-13.
[11] A. G. M. Selvam, R. Janagaraj, A. Hlafta, *Bifurcation behaviour of a discrete differential algebraic Prey-predator system with Holling type II functional response and prey refuge*, AIP Conf. Proc., **2282**, 020011 (2020), 1-13.
[12] A. G. M. Selvam, R. Janagaraj, M. Jacintha, *Stability, bifurcation, chaos: discrete prey predator model with step size*, Int. J. Eng. Innov. Technol., **9** (1) (2019), 3382-3387.
[13] O. A. Gumus¸, A. G. M. Selvam, R. Janagaraj, *Stability of modified Host-Parasitoid model with Allee effect*, Appl. Appl. Math., **15** (2) (2020), 1032-1045.
[14] O. A. Gumus, A. G. M. Selvam, D. A. Vianny, *Bifurcation and stability analysis of a discrete time SIR epidemic model with vaccination*, Int. J. Anal. Appl., **17** (5) (2019), 809-820.
[15] O. A. Gumus, S. Acer, *Period-doubling bifurcation analysis and stability of epidemic model*, J. Sci. Arts, **49** (4) (2019), 905-914.
[16] O. A. Gumus, M. Feckan, *Stability, Neimark-Sacker bifurcation and chaos control for a prey-predator system with harvesting effect on predator*, Miskolc Math. Notes, **22** (2) (2021), 663-679.
[17] O. A. Gumus, *Neimark-Sacker bifurcation and stability of a prey-predator model*, Miskolc Math. Notes, **21** (2) (2020), 873-885.
[18] Q. Din, O. A. Gumus, H. Khalil, *Neimark-sacker bifurcation and chaotic behaviour of a modified host parasitoid model*, Z. Naturforsch. A, **72** (1) (2017), 25-37.
[19] Q. Din, *Stability, Bifurcation analysis and chaos control for a predator-prey system*, J. Vib. Control, **25** (3) (2019), 612-626.
[20] O. A. Gumus, A.G.M. Selvam, R. Dhineshbabu, *Bifurcation analysis and Chaos control of the population model with harvest*, Int. J. Nonlinear Anal. Appl., **13** (1) (2021), 115-125.
[21] O. A. Gumus, Q. Cui, A.G.M.Selvam, D.A. Vianny, *Global stability and bifurcation analysis of a discrete-time sir epidemic model*, Miskolc Math. Notes, **22** (2023), 193-210.
[22] O. A. Gumus, A.G.M. Selvam, R. Janagaraj, *Dynamics of the mathematical model related to COVID-19 pandemic with treatment*, Thai J. Math, **20** (2) (2022), 957-970.
[23] O. A. Gumus, H. Baran, *Dynamics of SIR Epidemic model with treatment function*, Int. Battalgazi Sci. Stud. Cong., (2021), 140-153.
[24] Y. Enatsu, Y. Nakata, Y. Muroya, *Global stability for a discrete SIS epidemic model with immigration of infectives*, J. Difference Equ. Appl., **18** (2012), 1913-1924.
[25] S. Yildiz, S. Bilazeroglu, H. Merdan, *Stability and bifurcation analyses of a discrete Lotka–Volterra type predator–prey system with refuge effect*, J. Comput. Appl. Math., **422** (2023) 114910.
[26] O. A. Gumus, A.G.M. Selvam, D. Vignesh, *The effect of allee factor on a nonlinear delayed population model with harvesting*, J. Sci. Arts, **22** (1) (2022), 159-176.
[27] Z. Hu, Z. Teng, L. Zhang, *Stability and flip bifurcation of a discrete SIS epidemic model*, J. Xinjiang Univ. (Natural Sci. Edit.), **28** (2011), 446-453.
[28] Z. Teng, H. Jiang, *Stability analysis in a class of discrete SIRS epidemic models*, Nonlinear Anal. RWA, **13** (2012), 2017-2033.

[29] Q. Chen, Z. Teng, L. Wang, H. Jiang, *The existence of codimension-two bifurcation in a discrete SIS epidemic model with standard incidence*, Nonlinear Dynam., **71** (2013), 55-73.
[30] A.Q. Khan, M. Tasneem, B. Younis, T.F. Ibrahim, *Dynamical analysis of a discrete-time COVID-19 epidemic model*, Math. Meth. Appl. Sci., **46** (2022), 4789–4814.
[31] M.H. DarAssi, S. Damrah, Y. AbuHour, *A mathematical study of the omicron variant in a discrete-time Covid-19 model*, Eur. Phys. J. Plus, **138** (2023), 601.
[32] R. George, N. Gul, A. Zeb, Z. Avazzadeh, S. Djilali, S. Rezapour, *Bifurcations analysis of a discrete time SIR epidemic model with nonlinear incidence function*, Results Phys., **38** (2022), 105580.
[33] Y. A. Kuznetsov, *Elements of Applied Bifurcation Theory*, Springer, 1998.
[34] S. Wiggins, *Introduction to Applied Nonlinear Dynamical Systems and Chaos*, Springer-Verlag, 2003.
[35] N. Kilinc, O.A. Gumus, *Analysis of the epidemic model depending on saturated and mass action incidence rates with treatment*, $7^{th}$ Int. Erciyes Sci. Res. Cong., (2022), 229-316.
[36] S. N. Elaydi, *An Introduction to Difference Equations*, Springer-Verlag, New York, 1996.
[37] X. Liu, D. Xiao, *Complex dynamic behaviors of a discrete time predator–prey system*, Chaos Solitons Fractals, **32** (2007), 80-94.
[38] Q. Din, *Dynamics of a discrete lotka-volterra model*, Adv. Difference Equ., **2013** (2013), 1-13.
[39] S. Kapcak, *Discrete dynamical systems with sage math*, The Electron. J. Math. & Tech., **12**(2) (2018), 292-308.
[40] U. Ufuktepe, S. Kapcak, *Applications of discrete dynamical systems with mathematica*, Kurenai, **1909** (2014), 207-216.

*Journal of Mathematical Sciences and Modelling*, 7(1) (2024) 14-19
*Research Article*

**Journal of Mathematical Sciences and Modelling**

*Journal Homepage: www.dergipark.gov.tr/jmsm*
*ISSN 2636-8692*
*DOI: http://dx.doi.org/10.33187/jmsm.1396368*

# A Difference Equation of Banking Loan with Nonlinear Deposit Interest Rate

**Moch. Fandi Ansori**[1] **and F. Hilal Gümüş**[2*]

[1]*Department of Mathematics, Faculty of Science and Mathematics, Universitas Diponegoro, Semarang, Indonesia*
[2]*Department of Finance and Banking, School of Applied Sciences, Zonguldak Bulent Ecevit University, Zonguldak, Turkey*
[*]*Corresponding author*

**Article Info**

***Keywords:*** *Banking loan dynamics, Nonlinear interest rate, Stability*
***2010 AMS:*** *39A33, 39A60*
***Received:*** *26 November 2023*
***Accepted:*** *5 February 2024*
***Available online:*** *25 February 2024*

**Abstract**

This paper considers a banking loan model using a difference equation with a nonlinear deposit interest rate. The construction of the model is based on a simple bank balance sheet composition and a gradient adjustment process. The model produces two unstable loan equilibriums and one stable equilibrium when the parameter corresponding to the deposit interest rate is situated between its transcritical and flip bifurcations. Some numerical simulations are presented to align with the analytical findings, such as the bifurcation diagram, Lyapunov exponent, cobweb diagram, and contour plot sensitivity. The significance of our result is that the banking regulator may consider the lower and upper bounds for setting the nonlinear interest rate regulation and provide a control regulation for other banking factors to maintain loan stability.

## 1. Introduction

In recent years, several researchers have used difference equations to study the dynamics of banking loans with various factors appearing in the banking system. For monopoly cases, authors in [1, 2] study the effect of banking deposit and loan costs on banking loan dynamics, authors in [3, 4] investigate the influence of capital policy and dividend payment on banking loan dynamics by incorporating economies and dis-economies of scope, authors in [5] explore the dynamics of the loan with reserve requirement policy, authors in [6] inspect the banking loan dynamics with a macro-prudential policy in Indonesia in the form of reserve requirement based on loan-to-deposit ratio, authors in [7] research the impact of the amount of premium and membership contribution policy from the Indonesia deposit insurance corporation on banking loan dynamics, and authors in [8] analyze loan benchmark interest rates in banking loan dynamics. For duopoly cases, the study is initiated by Fanti [9] where capital regulation is considered under heterogeneous and homogeneous models, and it is followed by authors in [10, 11] where they study capital regulation with banking cost under the case of Italian banks.

In this paper, we consider a monopoly model to analyze the dynamics of a single bank's loan when its deposit interest rate is assumed to be nonlinear. The nonlinear interest rate is induced in paper [11], but in the paper, the nonlinear aspect arises in loan interest rate. In economic analysis, nonlinear interest rates have been studied for decades. For example, the study in [12] investigates nonlinear dynamics in the US short-term interest rate time series, authors in [13] focus on Spanish banks' nonlinear interest rate sensitivity, the study in [14] shows that a stabilizing influence on interest rates is compatible with a nonlinear process, and authors in [15, 16] evaluate nonlinear interest rate response functions for South Africa and the United Kingdom.

In the next section, we construct the banking loan model with the nonlinear deposit interest rate, and it is followed by the analysis of its equilibrium. The following section presents several numerical simulations to confirm the analysis. The last section concludes.

***Email addresses and ORCID numbers*: mochfandiansori@lecturer.undip.ac.id, 0000-0002-4588-3885 (M. F. Ansori), gumus@beun.edu.tr, 0000-0002-6329-7142 (F. H. Gümüş),**
**Cite as "M. F. Ansori, F. H. Gümüş, *A difference equation of banking loan with nonlinear deposit interest rate*, J. Math. Sci. Model., 7(1) (2024), 14-19"**

## 2. Model Construction

Consider a bank with the following simple balance sheet components: loan $(L)$, capital $(E)$, and deposit $(D)$. The bank balance sheet's identification offers

$$L = D + E$$

The capital regulation requires every bank should maintain its capital not less than a certain percentage of its assets. Since in this model, we only consider loan as the only asset, thus we have $E \geq \kappa L$, where $0 < \kappa < 1$. For the purpose of simplification of the model's analysis, suppose that $E = \kappa L$. Thus, we obtain

$$D = (1-\kappa)L$$

Usually, the loan interest is subtracted by the banking expenses to find the bank's profit. The costs contain deposit interest, capital dividend, and operating costs. In this paper, we use a simpler profit calculation as follows

$$\pi = rL - r_D D \tag{2.1}$$

where $\pi$ is profit, $r$ is the loan interest rate, and $r_D$ is the deposit interest rate. We assume that $r > 0$ is a constant rate, meanwhile, $r_D$ is a nonlinear rate

$$r_D = \frac{1}{a-D} \tag{2.2}$$

where $a > D > 0$. The nonlinear deposit interest rate formulation in (2.2) still meets the condition in the well-known Monti-Klein model [17, 18], that it must have a slope. We have

$$\frac{dr_D}{dD} = \frac{1}{(a-D)^2} > 0$$

Substituting (2.2) into (2.1) produces

$$\pi = rL - \frac{1}{a-D}D = rL - \frac{(1-\kappa)L}{a-(1-\kappa)L}$$

Next, we calculate the profit marginal as follows

$$\frac{\partial \pi}{\partial L} = r - \frac{(1-\kappa)a}{[a-(1-\kappa)L]^2}$$

To model the dynamics of banking loans, we follow the gradient adjustment process [19], that is

$$L_{t+1} = L_t + \alpha L_t \frac{\partial \pi_t}{\partial L_t}$$

where $\alpha > 0$. The final model is provided below

$$L_{t+1} = f(L_t) := L_t + \alpha L_t \left( r - \frac{(1-\kappa)a}{[a-(1-\kappa)L_t]^2} \right) \tag{2.3}$$

## 3. Analysis

The map (2.3) has three equilibrium points, namely

$$L_0^* = 0, \quad L_1^* = \frac{a + \sqrt{\frac{(1-\kappa)a}{r}}}{1-\kappa}, \quad \text{and} \quad L_2^* = \frac{a - \sqrt{\frac{(1-\kappa)a}{r}}}{1-\kappa}$$

It can be seen that $L_1^* > 0$. But, for the case of $L_2^*$, we need a condition that will guarantee $L_2^* > 0$, that is

$$a > \frac{1-\kappa}{r} \tag{3.1}$$

To study the stability of the equilibriums, we will use the following lemma. But, before that, first, we need to calculate $f'(L_t)$. We have

$$f'(L_t) = 1 + \alpha r - \alpha a(1-\kappa)\left( \frac{a + (1-\kappa)L_t}{[a-(1-\kappa)L_t]^3} \right)$$

**Lemma 3.1** ([20]). *Let $x^*$ be an equilibrium point of the difference equation*

$$x_{n+1} = f(x_n)$$

*where $f$ is continuously diffrentiable at $x^*$. The following statements then hold true:*

*i. If $\left| f'(x^*) \right| < 1$, then $x^*$ is locally asymptotically stable.*

*ii. If $\left| f'(x^*) \right| > 1$, then $x^*$ is locally unstable.*

The case when $f'(L^*)=1$, there happens a transcritical bifurcation, meanwhile, a flip bifurcation happens if $f'(L^*)=-1$ [21]. The following theorems provide information about each equilibrium's stability.

**Theorem 3.2.** *The equilibrium point $L_0^*=0$ of the model (2.3) is unstable for all parameters.*

*Proof.* By substituting $L_0^*=0$ into $f'(L^*)$, we have

$$f'(0)=1+\alpha\left(r-\frac{1-\kappa}{a}\right)$$

From condition in (3.1), we have $r-\frac{1-\kappa}{a}>0$. Thus, $f'(0)>1$. This means that $L_0^*=0$ is unstable. □

**Theorem 3.3.** *For all parameters, the equilibrium point $L_1^*=\frac{a+\sqrt{\frac{(1-\kappa)a}{r}}}{1-\kappa}$ of the model (2.3) is unstable.*

*Proof.* Substituting $L_1^*=\frac{a+\sqrt{\frac{(1-\kappa)a}{r}}}{1-\kappa}$ into $f'(L^*)$ produces

$$f'\left(\frac{a+\sqrt{\frac{(1-\kappa)a}{r}}}{1-\kappa}\right)=1+2\alpha r\left(\sqrt{\frac{ar}{1-\kappa}}+1\right)$$

It is clear that $f'\left(\frac{a+\sqrt{\frac{(1-\kappa)a}{r}}}{1-\kappa}\right)>1$, since all parameters are positive and $0<\kappa<1$. Thus, $L_1^*$ is unstable. □

**Theorem 3.4.** *The equilibrium point $L_2^*=\frac{a-\sqrt{\frac{(1-\kappa)a}{r}}}{1-\kappa}$ of the model (2.3) is locally asymptotically stable if*

$$\frac{1-\kappa}{r}<a<\left(\frac{1-\kappa}{r}\right)\left(\frac{1+\alpha r}{\alpha r}\right)^2$$

*Proof.* We have

$$f'\left(\frac{a-\sqrt{\frac{(1-\kappa)a}{r}}}{1-\kappa}\right)=1+2\alpha r\left(1-\sqrt{\frac{ar}{1-\kappa}}\right)<1$$

if $a>\frac{1-\kappa}{r}$. This condition has already appeared in (3.1). Next, we have

$$f'\left(\frac{a-\sqrt{\frac{(1-\kappa)a}{r}}}{1-\kappa}\right)=1+2\alpha r\left(1-\sqrt{\frac{ar}{1-\kappa}}\right)>-1$$

if $a<\left(\frac{1-\kappa}{r}\right)\left(\frac{1+\alpha r}{\alpha r}\right)^2$. Thus, $|f'(L_2^*)|<1$ if $\frac{1-\kappa}{r}<a<\left(\frac{1-\kappa}{r}\right)\left(\frac{1+\alpha r}{\alpha r}\right)^2$. □

From Theorem 3.4, we have the following corollary.

**Corollary 3.5.** *The equilibrium $L_2^*$ might become unstable due to transcritical and flip bifurcations when $a=a^T:=\frac{1-\kappa}{r}$ and $a=a^F:=\left(\frac{1-\kappa}{r}\right)\left(\frac{1+\alpha r}{\alpha r}\right)^2$.*

Based on Theorem 3.4 and Corollary 3.5, we can say that the stable region of $(\alpha,a)$-parameter space lies in between the spaces $\{(\alpha,a):a<\frac{1-\kappa}{r}\}$ and $\{(\alpha,a):a>(\frac{1-\kappa}{r})(\frac{1+\alpha r}{\alpha r})^2\}$. This result is illustrated in Figure 4.1.

## 4. Numerical Simulation

For simulation purposes, we use parameter values $r=0.2$, $\kappa=0.08$, and $\alpha=50$, while $a$ varies across the simulations. The reason for choosing the parameter values is only to display the existence of transcritical and flip bifurcations, and also the complex dynamics of the map (2.3).

The bifurcation diagram of parameter $a$ for $a\in[4.6;6.1]$ is shown in Figure 4.2a. When $a$ gets bigger, the loan equilibrium goes up until it reaches the flip bifurcation point, and then it produces a period-doubling and leads to chaos. The confirmation of the existence of chaotic behavior can be seen also in the Lyapunov exponent of map (2.3) as shown in Figure 4.2b by the red marker, as we know that the positive Lyapunov exponent can show the existence of chaos.

Another way to depict the complex dynamics of map (2.3) is by presenting the cobweb diagram. In Figure 4.3, we simulate four scenarios for the cobweb diagram and the respected time series of $L_t$. First, a stable banking loan is presented in Figure 4.3a for $a=5$. Second, a display of two-period of banking loan is depicted in Figure 4.3b for $a=5.6$. Third, a four-period banking loan dynamics for $a=5.85$ as shown in Figure 4.3c. The last is for $a=6$ which shows the chaotic dynamics of banking loan, see Figure 4.3d.

The next simulation is a numerical sensitivity analysis to see the effect of changes of two parameters simultaneously on the stability of a banking loan. Before that, we define a function $S=\left(\frac{ar}{1-\kappa}\right)\left(\frac{\alpha r}{1+\alpha r}\right)^2$. Then, the stability condition in Theorem 3.4 can seen as $\left(\frac{\alpha r}{1+\alpha r}\right)^2<S<1$. We perform a contour plot $S$ to see the impact of a combination of two parameters on banking loan stability by looking at the region where $S$ has a value less than 1. The contour plot of $S$ is displayed in Figure 4.4. This enables us to observe which region can guarantee a stable banking loan, and also it can be used for controlling the stability of banking loan.

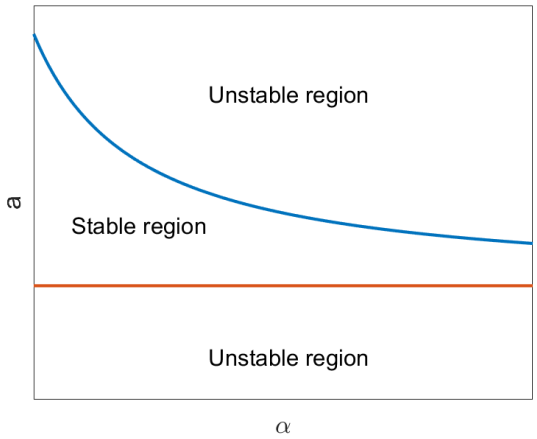


**Figure 4.1:** Stability region of $(\alpha, a)$-parameter space for map (2.3).

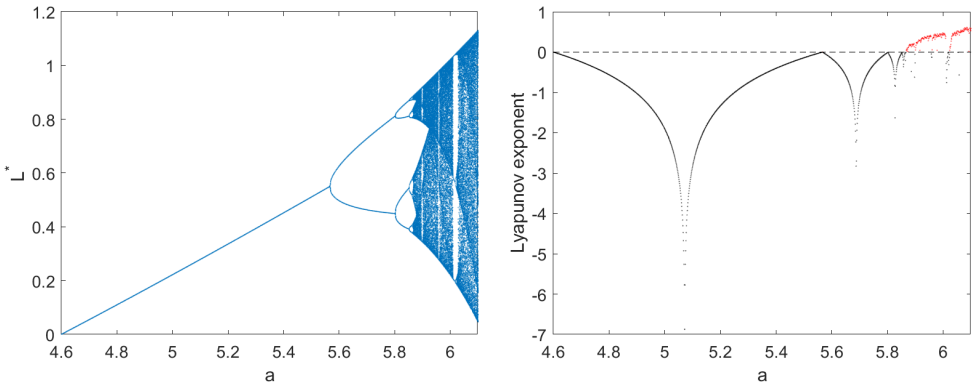


**Figure 4.2:** (a) The parameter $a$ bifurcation diagram, and (b) the associated Lyapunov exponent.

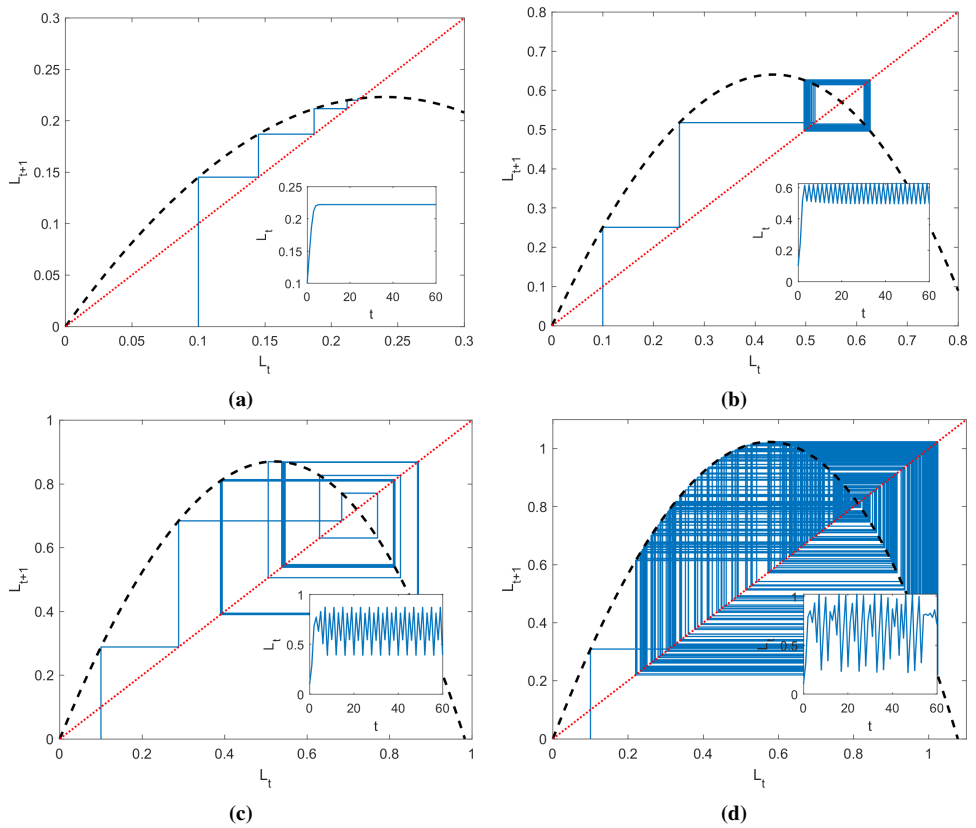


**Figure 4.3:** Cobweb diagram of map (2.3) and time series of $L_t$ when (a) $a = 5$, (b) $a = 5.6$, (c) $a = 5.85$, and (d) $a = 6$.

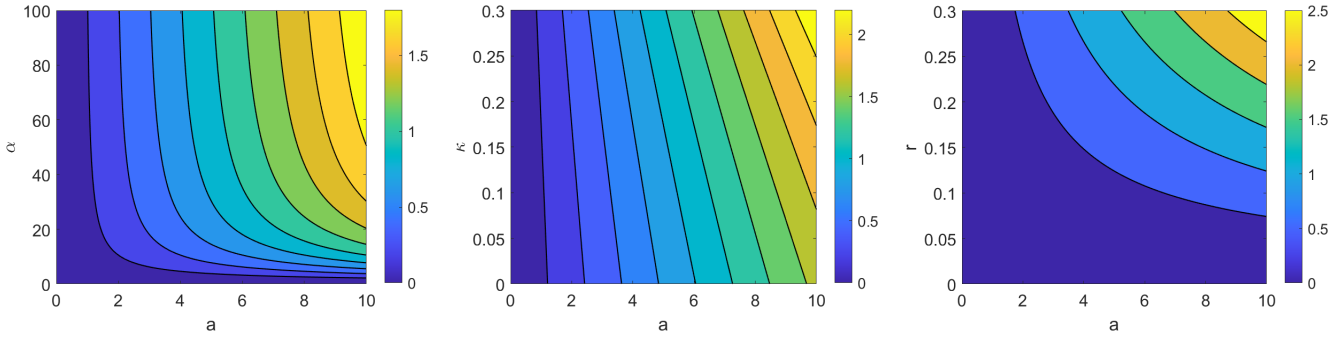


**(a)** **(b)** **(c)**

**Figure 4.4:** Contour plot of $S$ for different parameter spaces.

## 5. Discussion and Conclusion

The introduction of nonlinear deposit interest rate in the banking system can produce rich dynamics. The result shows that the bifurcation parameter is crucial to affect the banking loan dynamics. A higher bifurcation parameter means that the deposit interest rate becomes lower. When this happens, it can cause a period-doubling banking loan and even lead to chaos. To control this phenomenon, we can use the other parameters to reduce the risk of unstable banking loans by observing the sensitivity analysis. In our analysis, we can draw a comparison to the linear deposit interest rate that has been examined in previous research [22]. The authors of these studies analyze a deposit benchmark interest rate that is incorporated into the linear interest rate. They demonstrate that a decrease in the linear deposit interest rate can lead to periodic or even chaotic dynamics in banking loans. Our findings align with the fact that a greater value of the nonlinear interest rate parameter (equal to a lower interest rate) may indicate the presence of periodic or chaotic dynamics in banking loans. The model described in [22] can be reformulated as a logistic map. However, our present model cannot be converted into a logistic map, while it still yields comparable findings. This study only uses a very simple model that consists of deposit, equity, and loan, and of course, it is a monopoly model. Thus, for upcoming research, the addition of other bank balance sheet variables such as reserve requirement policy and/or the case of the duopoly model can be considered.

## Article Information

**Acknowledgements:** The authors would like to express their sincere thanks to the editor and the anonymous reviewers for their helpful comments and suggestions.

**Author's contributions:** All authors contributed equally to the writing of this paper. All authors read and approved the final manuscript.

**Conflict of Interest Disclosure:** No potential conflict of interest was declared by the author.



**Supporting/Supporting Organizations:** No grants were received from any public, private or non-profit organizations for this research.

**Ethical Approval and Participant Consent:** It is declared that during the preparation process of this study, scientific and ethical principles were followed and all the studies benefited from are stated in the bibliography.

**Plagiarism Statement:** This article was scanned by the plagiarism program. No plagiarism detected.

## References

[1] M. F. Ansori, S. Hariyanto, *Analysis of banking deposit cost in the dynamics of loan: Bifurcation and chaos perspectives*, BAREKENG: J. Math. App., **16**(4) (2022), 1283-1292, doi:10.30598/barekengvol16iss4pp1283-1292.

[2] M. F. Ansori, S. Khabibah, *The role of cost of loan in banking loan dynamics: Bifurcation and chaos analysis*, BAREKENG: J. Math. App., **16**(3) (2022), 1031-1038, doi:10.30598/barekengvol16iss3pp1031-1038.

[3] N. Y. Ashar, M. F. Ansori, H. K. Fata, *The effects of capital policy on banking loan dynamics: A difference equation approach*, Int. J. Differ. Equations (IJDE), **18**(1) (2023), 267-279.

[4] H. K. Fata, N. Y. Ashar, M. F. Ansori, *Banking loan dynamics with dividen payments*, Adv. Dyn. Syst. Appl. (ADSA), **18**(2) (2023), 87-99.

[5] M. F. Ansori, G. Theotista, Winson, *Difference equation-based banking loan dynamics with reserve requirement policy*, Int. J. Differ. Equations (IJDE), **18**(1) (2023), 35-48.

[6] M. F. Ansori, N. Sumarti, K. A. Sidarto, I. Gunadi, *Analyzing a macroprudential instrument during the COVID-19 pandemic using border collision bifurcation*, Rect@: Rev. Electron. Commun. y Trabajos de ASEPUMA, **22**(2) (2022), 113-125, doi: 10.24309/recta.2021.22.2.04.

[7] M. F. Ansori, G. Theotista, M. Febe, *The influence of the amount of premium and membership of IDIC on banking loan procyclicality: A mathematical model*, Adv. Dyn. Syst. Appl. (ADSA), **18**(2) (2023), 111-123.

[8] M. F. Ansori, N. Y. Ashar, *Analysis of loan benchmark interest rate in banking loan dynamics: bifurcation and sensitivity analysis*, J. Math. Model. Finance, **3**(1) (2023), 191-202, doi: 10.22054/jmmf.2023.74976.1098.

[9] L. Fanti, *The dynamics of a banking duopoly with capital regulations*, Econ. Model., **37** (2014), 340-349, doi: 10.1016/j.econmod.2013.11.010.

[10] S. Brianzoni, G. Campisi, *Dynamical analysis of a banking duopoly model with capital regulation and asymmetric costs*, Discrete Contin. Dyn. Syst. - B, **26** (2021), 5807-5825, doi: 10.3934/dcdsb.2021116.

[11] S. Brianzoni, G. Campisi, A. Colasante, *Nonlinear banking duopoly model with capital regulation: The case of Italy*, Chaos Solitons Fractals, **160** (2022), 112209, doi: 10.1016/j.chaos.2022.112209.

[12] G. A. Pfann, P. C. Schotman, R. Tschernig, *Nonlinear interest rate dynamics and implications for the term structure*, J. Econom., **74**(1) (1996), 149-176, doi: 10.1016/0304-4076(95)01754-2.
[13] L. Ballester, R. Ferrer, C. González, *Linear and nonlinear interest rate sensitivity of Spanish banks*, The Spanish Rev. Financ. Econ., **9**(2) (2011), 35-48, doi: 10.1016/j.srfe.2011.09.002.
[14] P. A. Shively, *Threshold nonlinear interest rates*, Econ. Lett., **88**(3) (2005), 313-317, doi: 10.1016/j.econlet.2004.12.032.
[15] Y. Baaziz, M. Labidi, A. Lahiani, *Does the South African reserve bank follow a nonlinear interest rate reaction function?*, Econ. Model., **35** (2005), 272-282, doi: 10.1016/j.econmod.2013.07.014.
[16] R. Brüggemann, J. Riedel, *Nonlinear interest rate reaction functions for the UK*, Econ. Model., **28** (2011), 1174-1185, doi: 10.1016/j.econmod.2010.12.005.
[17] M. A. Klein, *A theory of the banking firm*, J. Money Credit Banking, **3** (1971), 205-218.
[18] M. Monti, *Deposit, credit and interest rates determination under alternative objective functions*, G. P. Szego, K. Shell (Eds.), Math. Methods Investment Finance, Amsterdam, 1972.
[19] M. G. I. Bischi, C. Chiarella, M. Kopel, F. Szidarovszky, *Nonlinear Oligopolies: Stability and Bifurcations*, Berlin: Springer-Verlag, 2010.
[20] S. Elaydi, *An Introduction to Difference Equations*, New York, NY, USA: Springer, 1996.
[21] K. Alligood, T. Sauer, J. Yorke, *Chaos: An Introduction to Dynamical Systems*, New York: Springer-Verlag, 1996.
[22] M. F. Ansori, N. Y. Ashar, H. K. Fata, *Logistic map-based banking loan dynamics with central bank policies*, J. Appl. Nonlinear Dyn., (2024), (in press).

*Journal of Mathematical Sciences and Modelling*, 7(1) (2024) 20-32
*Research Article*

**Journal of Mathematical Sciences and Modelling**

*Journal Homepage: www.dergipark.gov.tr/jmsm*
*ISSN 2636-8692*
*DOI: http://dx.doi.org/10.33187/jmsm.1289684*

# A Metapopulation Model for Cholera with Variable Media Efficacy and Imperfect Vaccine

**Phoebe Amadi[1], George Lawi[2] and Job Bonyo[3*]**

[1]*Department of Pure and Applied Mathematics, Maseno University, P.O. Box 133- 40105, Maseno, Kenya*
[2]*Department of Mathematics, Masinde Muliro University of Science and Technology, P.O. Box 190 - 50100, Kakamega, Kenya*
[3]*Department of Mathematics, Multimedia University of Kenya, P.O. Box 15653 - 00503, Nairobi, Kenya*
[*]*Corresponding author*

**Article Info**

***Keywords:*** *Cholera, Imperfet vaccine, Media awareness, Metapopulation, Migration*
***2010 AMS:*** *34C60, 34D20, 37N25*
***Received:*** *29 April 2023*
***Accepted:*** *8 November 2023*
***Available online:*** *25 February 2024*

**Abstract**

In this paper, a metapopulation model has been developed and analysed to describe the transmission dynamics of cholera between two communities linked by migration, in the presence of an imperfect vaccine and a varying media awareness impact. Stability analysis shows that the disease-free equilibrium is both locally and globally asymptotically stable when the vaccine reproduction number is less than unity. The endemic equilibria have also been shown to be locally asymptotically stable when the vaccine reproduction number is greater than unity. The simulation results show that with an imperfect vaccine and efficient media awareness, cholera transmission is reduced. The transmission rates have also been shown to be nonidentical in the two communities. It is therefore advisable, that health practitioners embrace the use of both vaccination and media awareness when designing and implementing community-specific cholera intervention strategies.

## 1. Introduction

Cholera is a diarrheal infection caused by ingestion of food or water contaminated with a gram-negative bacterium known as *Vibrio cholerae*. Humans and the aquatic environments are its main reservoirs. Majority of the infected individuals do not manifest any symptom [1]. Most of the cholera cases are presumptively diagnosed based on clinical suspicion in patients who present with severe acute watery diarrhea due to its high morbidity. If left untreated, cholera can kill within hours [1]. Its treatment depends on the severity of the illness and level of dehydration. Oral and intravenous rehydration are used to replace the lost fluids. Antibiotics are used in patients with severe volume depletion. An estimated 1.3m to 4m cholera cases with 21000 to 143000 mortalities occur annually [2, 3].
World Health Organization (WHO) recommends oral cholera vaccines as part of the integrated control program in areas at risk of cholera outbreak [4]. Two internationally-licensed oral cholera vaccines are available. Shanchol and Dukarol oral cholera vaccines have efficacies between 53% - 67% [5] and about 78% [6] respectively with Dukarol not being effective against *V. cholerae* 0139.
A multifaceted approach is key to control of cholera and to reduce related deaths. Actions targeting environmental conditions include the implementation of adapted long-term sustainable water sanitation and hygiene solutions to ensure use of safe water, basic sanitation and good hygiene practices to populations most at risk of cholera.
Cholera is more common in developing countries especially in Africa, parts of Asia and South and Central America where there is inadequate access to safe drinking water and poor sanitation facilities. In the 21$^{st}$ C, Sub-Saharan Africa bears the brunt of global cholera [7] where the countries face the dual challenges of improving both cholera treatment and access to basic health care, prevention and improved water and sanitation systems.
In Kenya, cholera is endemic in many parts of the country with sporadic outbreaks especially during rainy seasons and in informal settlements. Currently there has been cholera outbreaks in Wajir, Mandera, Machakos, Garissa, Migori and Kisumu counties. Evidently, socio-economic differences between regions would determine the efficacy of some strategies especially those targeting sanitation and hygiene.
A number of mathematical models have been developed to analyze the disease transmission dynamics.The dynamics and optimal control

***Email addresses and ORCID numbers*: amadiphoebe12@gmail.com, 0000-0002-5314-8688 (P. Amadi), glawi@mmust.ac.ke, 0000-0002-4699-558X (G. Lawi), jbonyo@mmu.ac.ke, 0000-0002-6442-4211 (J. Bonyo)**
**Cite as "P. Amadi, G. Lawi, J. Bonyo, *A Metapopulation model for cholera with variable media efficacy and imperfect vaccine*, J. Math. Sci. Model., 7(1) (2024), 20-32"**

strategies for cholera epidemics was developed and analysed in [8] under the interventions; vaccination, treatment and education awareness. The analysis indicates that vaccination and education campaigns should be applied from the start of an outbreak followed by treatment. However, the effects of vaccination and education campaigns could be affected by migration of especially the asymptomatically infected individuals.
The impact of media coverage on the spread of cholera was investigated in [9]. The numerical analysis shows that the disease dies out faster in the presence of media coverage. It's noteworthy that a combination of preventive and therapeutic strategies is likely to lead to a better outcome. A metapopulation model for cholera dynamics between two communities, in the presence of controls was developed and analysed in [10]. A model investigating the influence of cultural practices on the dynamics of cholera is presented in [3]. Modeling optimal intervention strategies for cholera is presented in [11]. A cost-effective balance of multiple intervention methods is compared for two endemic populations. The impact of spatial arrangements on epidemic disease dynamics and intervention strategies for cholera is investigated in [12]. The effects of vaccination, water chlorination and proper hygiene is investigated. The analysis shows that the infection may be eight times less devastating in the presence of controls. This model assumes uniform efficacy of the control strategies in the communities involved, and that vaccinated individuals are fully protected against the infection. These assumptions may not be entirely realistic since cholera vaccines are not 100% efficacious and the socio-economic differences between communities connected via migration is likely to determine the efficacy of control strategies. This work is largely part of the thesis [13].

### 1.1. Mathematical approaches in analyzing cholera transmission dynamics

A stochastic mathematical model with the rate of contact with the environment and the untreated individuals rate of recovery being subjected to some random interference was developed in [14]. The model investigates the behavior of solutions of a stochastic cholera model near the disease-free equilibrium and its corresponding deterministic endemic equilibrium. A mathematical model based on the general form of the Caputo fractional derivative is investigated for a real-world cholera outbreak in [2].
Mehmet et al [15] incorporated the random effects to the parameters of a deterministic model for the transmission dynamics of cholera to study the change of findings for Laplacian and Triangular distributions. Using Fuzzy set theory, [16] developed a cholera model in which all of the parameters were fuzzy numbers. The model study reveals that the imprecise parameter values have had a significant impact on both human and bacterial populations. In this paper, the dynamics of cholera transmission in two communities connected via migration when vaccination and media awareness are at different efficacy levels is explored.

## 2. Model Formulation and Description

To develop the metapopulation model, the general population considered is divided into two main communities and each community divided into four compartments with reference to vaccination of the susceptible individuals, impact of media awareness, *Vibrios* transmission and the disease states of the individuals. This model assumes that each community is homogeneous in the sense that there are no socio-economic barriers to interaction and a special heterogeneity which is accounted for by the immigrations. The compartments involve individuals who are susceptible $(S_i)$, the susceptible individuals who have been vaccinated against cholera $(V_i)$, those infected symptomatically and asymptomatically $(I_i)$ and those individuals who have recovered $(R_i)$ from the infection. The total population $N_i$, $(i = 1,2)$, of this model is given by;

$$N_i = S_i + V_i + I_i + R_i.$$

This model accounts for movement of asymptomatically infected individuals from one community to another. This group plays a vital role in metapopulation transmission modeling of cholera since they contribute to the disease transmission for a relatively long time. The role played by the asymptomatically infected individuals range from person to person transmission as well as shedding of the pathogens into the aquatic reservoirs. The symptomatically infected individuals are assumed to be quarantined in hospitals for treatment as soon as they are identified. The recruitment of the susceptible individuals into the communities are at the rates $\Lambda_1$ and $\Lambda_2$ for the first and the second communities respectively. This intrinsic difference rate is mainly the difference of births, deaths and immigrations at the time of modeling. Vaccination of the susceptible individuals is at the rates $\omega_1$ and $\omega_2$ for the first and second communities respectively, with $0 < \sigma_i < 1$, for $i = 1,2$ denoting the vaccine efficacy. This implies that when $\sigma$ is close to one, the vaccine is very effective and the disease transmission is low and when $\sigma$ is close to zero, the vaccine is not effective and the disease transmission is high. Considering the relatively long vaccine protection period [1], this model excludes vaccinated individuals whose immunity has waned off to become susceptible.
The concentration of *Vibrios* in the environment is denoted by $B_1$ and $B_2$ for the first and second communities respectively. The susceptible individuals acquire cholera infection through ingestion of environmental *Vibrios* from contaminated water reservoirs at the rates $\lambda_{ei}$ and through human-to-human transmission after ingestion of hyperinfectious *Vibrios* at the rates $\lambda_{hi}$ for $i = 1,2$, where;

$$\lambda_{ei} = (1-\rho_i)\frac{\beta_{ei}B_i}{k+B_i}, \text{ and } \lambda_{hi} = (1-\rho_i)\frac{\beta_{hi}I_i}{m+I_i}.$$

The susceptible population is infected following ingestion of *Vibrios* from aquatic reservoirs at the rate $\beta_{ei}$ and $(1-\rho_i)\beta_{ei}$, is the reduced rate of ingestion of *Vibrios* from the environment due to media awareness, where $0 < \rho_i < 1$ measures the efficacy of media awareness. The half saturation constant of the pathogen population, enough to make an individual to contract the infection is denoted by $k > 0$. The saturation incidence function $\frac{\beta_{ei}B_i}{k+B_i}$ ensures boundedness of the incidence rate of infection from the environment and indicates that the incidence rate is gradual rather than linear. $\beta_{hi}$ is the effective contact rate for human-to-human transmission. The minimum contact rate with an infected person that can cause about 50% chance of contracting the infection is denoted by $m$. $\frac{I_i}{m+I_i}$ is a continuous bounded function which takes into account the disease saturation.
The natural death rates in the first and second communities are denoted by $\mu_1$ and $\mu_2$ respectively. The infected individuals recover from the infection at the rates $\gamma_1$ and $\gamma_2$ and suffer disease induced mortality at the rates $\delta_1$ and $\delta_2$ for the first and second communities respectively. The recovered individuals are assumed to develop some immunity after recovery, and cannot be infected again in one outbreak [17]. The movement of asymptomatically infected individuals across the communities is at the rates $a_1$ and $a_2$ for the first and second communities

respectively. Infected individuals shed bacteria into the environment at the rates $\xi_1$ and $\xi_2$ in the first and second communities respectively. The decay rates of the pathogens is denoted by $\mu_{1p}$ and $\mu_{2p}$ while the multiplication rates of pathogens in the aquatic reservoirs is denoted by $g_1$ and $g_2$ in the first and second communities respectively.
The above description is captured in the flow chart diagram in Figure 2.1. A mathematical equivalent is given in terms of system of ordinary differential equations (2.1).

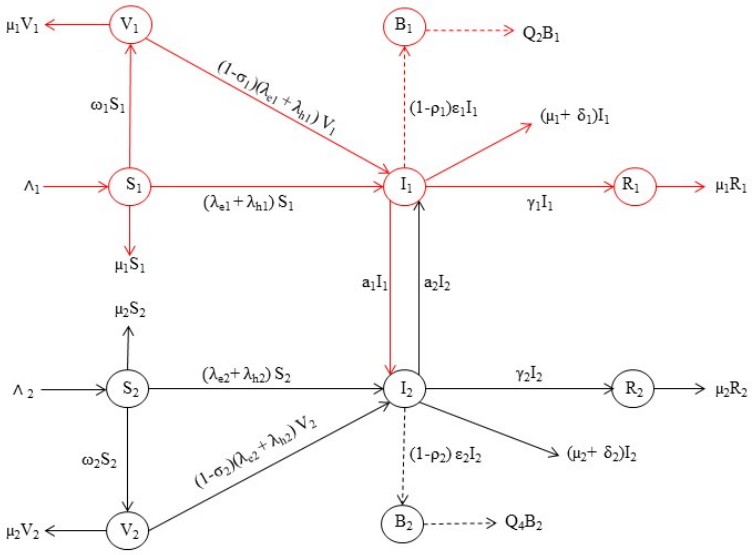


**Figure 2.1:** The Flow Diagram for the Metapopulation Model.

$$
\begin{aligned}
\frac{dS_1}{dt} &= \Lambda_1 - \omega_1 S_1 - [\lambda_{e1} + \lambda_{h1}]S_1 - \mu_1 S_1 \\
\frac{dV_1}{dt} &= \omega_1 S_1 - (1-\sigma_1)[\lambda_{e1} + \lambda_{h1}]V_1 - \mu_1 V_1 \\
\frac{dI_1}{dt} &= [\lambda_{e1} + \lambda_{h1}]S_1 + (1-\sigma_1)[\lambda_{e1} + \lambda_{h1}]V_1 + a_2 I_2 - Q_1 I_1 \\
\frac{dR_1}{dt} &= \gamma_1 I_1 - \mu_1 R_1 \\
\frac{dB_1}{dt} &= (1-\rho_1)\xi_1 I_1 - Q_2 B_1 \\
\frac{dS_2}{dt} &= \Lambda_2 - \omega_2 S_2 - [\lambda_{e2} + \lambda_{h2}]S_2 - \mu_2 S_2 \\
\frac{dV_2}{dt} &= \omega_2 S_2 - (1-\sigma_2)[\lambda_{e2} + \lambda_{h2}]V_2 - \mu_2 V_2 \\
\frac{dI_2}{dt} &= [\lambda_{e2} + \lambda_{h2}]S_2 + (1-\sigma_2)[\lambda_{e2} + \lambda_{h2}]V_2 + a_1 I_1 - Q_3 I_2 \\
\frac{dR_2}{dt} &= \gamma_2 I_2 - \mu_2 R_2 \\
\frac{dB_2}{dt} &= (1-\rho_2)\xi_2 I_2 - Q_4 B_2,
\end{aligned}
$$

where $Q_1 = \mu_1 + \delta_1 + \gamma_1 + a_1$, $Q_2 = \mu_{1p} - g_1$, $Q_3 = \mu_2 + \delta_2 + \gamma_2 + a_2$, $Q_4 = \mu_{2p} - g_2$. $Q_2$ and $Q_4$ are positive such that in the presence of improved hygiene and sanitation and reduced shedding rate of the pathogens by the infected individuals, the bacteria cannot sustain themselves in the aquatic environment [18]. The equation for the recovered compartment is decoupled in equation (2.1), thus it is enough to

consider the following reduced system of equations:

$$\begin{aligned}
\frac{dS_1}{dt} &= \Lambda_1 - \omega_1 S_1 - [\lambda_{e1} + \lambda_{h1}]S_1 - \mu_1 S_1 \\
\frac{dV_1}{dt} &= \omega_1 S_1 - (1-\sigma_1)[\lambda_{e1} + \lambda_{h1}]V_1 - \mu_1 V_1 \\
\frac{dI_1}{dt} &= [\lambda_{e1} + \lambda_{h1}]S_1 + (1-\sigma_1)[\lambda_{e1} + \lambda_{h1}]V_1 + a_2 I_2 - Q_1 I_1 \\
\frac{dB_1}{dt} &= (1-\rho_1)\xi_1 I_1 - Q_2 B_1 \\
\frac{dS_2}{dt} &= \Lambda_2 - \omega_2 S_2 - [\lambda_{e2} + \lambda_{h2}]S_2 - \mu_2 S_2 \\
\frac{dV_2}{dt} &= \omega_2 S_2 - (1-\sigma_2)[\lambda_{e2} + \lambda_{h2}]V_2 - \mu_2 V_2 \\
\frac{dI_2}{dt} &= [\lambda_{e2} + \lambda_{h2}]S_2 + (1-\sigma_2)[\lambda_{e2} + \lambda_{h2}]V_2 + a_1 I_1 - Q_3 I_2 \\
\frac{dB_2}{dt} &= (1-\rho_2)\xi_2 I_2 - Q_4 B_2.
\end{aligned} \tag{2.1}$$

## 3. Model Analysis and Discussion

### 3.1. Positivity and boundedness of solutions

#### 3.1.1. Positivity of solutions

The well posedness of the model is established by showing that its solutions are positive and bounded. An assumption is made that the initial conditions of system (2.1) are non-negative since the model monitors populations. Therefore, $S_i(0) > 0, V_i(0) \geq 0, I_i(0) \geq 0, B_i(0) \geq 0$ for $i = 1,2$. The total population for each community satisfies $\frac{dNi(t)}{dt} = \Lambda_i - \mu i N_i - \delta_i$ and the total population size for the two communities is $N(t) = \sum_{i=1}^{2}(N_i(t))$.

**Theorem 3.1.** *Let the initial conditions be $S_i(0) > 0, V_i(0) \geq 0, I_i(0) \geq 0, B_i(0) \geq 0$, then the solution set $\{S_i(t), V_i(t), I_i(t), B_i(t)\}$ $(i = 1,2)$ of the model system (2.1) is positive for all $t > 0$.*

*Proof.* From the first equation of system (2.1);

$$\frac{dS_i}{dt} = \Lambda_i - \omega_i S_i - \lambda_{ei} S_i - \lambda_{hi} S_i - \mu_i S_i,$$

implying that

$$\frac{dS_i}{dt} \geq -[\omega_i + \lambda_{ei} + \lambda_{hi} + \mu_i]S_i.$$

Integration yields

$$S_i(t) \geq e^{-[\omega_i + \lambda_{ei} + \lambda_{hi} + \mu_i]t} e^C$$

for some constant C. Hence, $S_i(t) > 0$ for all $t \geq 0$. Similarly, it can also be shown that the other solutions are non-negative for all $t \geq 0$. □

#### 3.1.2. Boundedness of the solutions

The model solutions are shown to be bounded in the invariant region $\Omega$ where $\Omega = \{(S_1, V_1, I_1, B_1, S_2, V_2, I_2, B_2) : N_i \leq \frac{\Lambda_i}{\mu_i}\}$ for $i = 1,2$.

**Theorem 3.2.** *The solutions of the model system (2.1) are bounded in the feasible region $\Omega$.*

*Proof.* Since the initial conditions for system (2.1) are non-negative, $\Omega = \bigcup_{i=1}^{2} \Omega_i$ and that each community is a closed community with respect to the adjacent community, the time derivative of $N_i(t)$ for $(i = 1,2)$ is given by

$$\frac{dN_i}{dt} = \Lambda_i - \mu_i(S_i + V_i + I_i + R_i) - \delta_i I_i,$$

and therefore

$$\frac{dN_i}{dt} + \mu_i N_i \leq \Lambda_i.$$

By solving, we obtain $N_i(t) \leq \frac{\Lambda_i}{\mu_i} + e^{-\mu_i t} C$ for some positive constant $C$.

Thus $N_i(0) \leq \frac{\Lambda_i}{\mu_i} + C$ and $\lim_{t\to\infty} N_i(t) \leq \frac{\Lambda_i}{\mu_i} + C$. Hence $0 < N_i(t) \leq \frac{\Lambda_i}{\mu_i} + C$ $(i = 1,2)$ for all $t \geq 0$, which implies that the solutions of system (2.1) are bounded in the invariant region $\Omega$. Thus the model is mathematically well posed and biologically meaningful in the feasible region $\Omega$. □

### 3.2. Stability analysis

An equilibrium point is defined as a steady state solution of a model. The stability of model (2.1) is analysed in order determine the impact of imperfect vaccine and variable media awareness on the epidemiology of cholera between the two communities linked via migration. The existence of the equilibrium points of model (2.1) with respect to the basic reproduction number is derived using the next generation matrix approach.

#### 3.2.1. Disease free equilibrium $(E_0)$

The disease free equilibrium (DFE) is a steady state solution of a mode. It is obtained by setting the right hand side of equation (2.1) to zero and solving with $I_i = B_i = 0$ $(i = 1,2)$. This yields $E_0 = (S_1, V_1, 0, 0, S_2, V_2, 0, 0) \in \mathbb{R}^8_+$ which is equal to

$$E_0 = \left[\frac{\Lambda_1}{\mu_1+\omega_1}, \frac{\Lambda_1\omega_1}{\mu_1(\mu_1+\omega_1)}, 0, 0, \frac{\Lambda_2}{\mu_2+\omega_2}, \frac{\Lambda_2\omega_2}{\mu_2(\mu_2+\omega_2)}, 0, 0\right] \tag{3.1}$$

Suppose there is no infection in a given population such that there is no infective, the solution of the systems of equations (2.1) corresponding to this state is the disease free equilibrium given by equation (3.1). This provides a baseline for analyzing the long term dynamics of cholera infection in the two communities under study.

#### 3.2.2. Basic and vaccine reproduction numbers

Basic reproduction number $R_0$ is the average number of secondary infections caused by a single infected agent during his/her entire infectious period, in a completely susceptible population. It sets the threshold in the study of a disease both for predicting its outbreak and for evaluating its control strategies. Theoretically, if $R_0 < 1$, then every infectious individual will cause less than one secondary infection and hence the disease will die out and when $R_0 > 1$, then every infectious individual will cause more than one secondary infection, hence the disease will be persistent in the population. A larger value of $R_0$ may indicate the possibility of a major epidemic. The vaccine reproduction number for model (2.1) is determined using the next generation matrix approach by Driessche et al [19] as:

$$R_{V1} = \frac{(\mu_1+\eta_1\omega_1)(\alpha_1\beta_{h1}\Lambda_1 kQ_2 + \alpha_1^2\beta_{e1}\Lambda_1\xi_1 m)}{\mu_1(\mu_1+\omega_1)kQ_1Q_2m} \tag{3.2}$$

and

$$R_{V2} = \frac{(\mu_2+\eta_2\omega_2)(\alpha_2\beta_{h2}\Lambda_2 kQ_4 + \alpha_2^2\beta_{e2}\Lambda_2\xi_2 m)}{\mu_2(\mu_2+\omega_2)kQ_3Q_4m},$$

where $R_{V1}$ and $R_{V2}$ are the vaccine reproduction numbers for comunity one and two respectively with $\alpha_i = 1-\rho_i$ and $\eta_i = 1-\sigma_i$, $(i = 1,2)$. In the absence of the intervention strategies (vaccination and media awareness) and the parameters $\omega_i$ and $\rho_1$, $i = 1,2$ are set to zero, then the basic reproduction numbers for the two communities are determined as:

$$R_{01} = \frac{\beta_{h1}\Lambda_1 kQ_2 + \beta_{e1}\Lambda_1\xi_1 m}{\mu_1 kQ_1Q_2m} \tag{3.3}$$

and

$$R_{02} = \frac{\beta_{h2}\Lambda_2 kQ_4 + \beta_{e2}\Lambda_2\xi_2 m}{\mu_2 kQ_3Q_4m},$$

where $R_{01}$ and $R_{02}$ are the basic reproduction numbers for community one and two respectively. This basic reproduction number is used to analyze the stability of the equilibrium points of model (2.1).

#### 3.2.3. Local stability of the disease free equilibrium

To investigate the local stability of the disease free equilibrium $(E_0)$, the method described in [19] is employed to linearize the model system (2.1).

**Theorem 3.3.** *The disease free equilibrium $(E_0)$ is locally asymptotically stable if $R_{Vi} < 1$ $(i = 1,2)$ and unstable otherwise.*

*Proof.* The Jacobian matrix of system (2.1) evaluated at $E_0$ is given by;

$$J(E_0) = \begin{bmatrix} -(\omega_1+\mu_1) & 0 & -\frac{\alpha_1\beta_{h1}\Lambda_1}{(\mu_1+\omega_1)m} & -\frac{\alpha_1\beta_{e1}\Lambda_1}{(\mu_1+\omega_1)k} \\ \omega_1 & -\mu_1 & -\frac{\eta_1\alpha_1\beta_{h1}\Lambda_1\omega_1}{\mu_1(\mu_1+\omega_1)m} & -\frac{\eta_1\alpha_1\beta_{e1}\Lambda_1\omega_1}{\mu_1(\mu_1+\omega_1)k} \\ 0 & 0 & \frac{(\mu_1+\eta_1\omega_1)\alpha_1\beta_{h1}\Lambda_1}{\mu_1(\mu_1+\omega_1)m} - Q_1 & \frac{(\mu_1+\eta_1\omega_1)\alpha_1\beta_{e1}\Lambda_1}{\mu_1(\mu_1+\omega_1)k} \\ 0 & 0 & \alpha_1\xi_1 & -Q_2. \end{bmatrix}$$

An equilibrium point is locally asymptotically stable if its Jacobian matrix has a negative trace and a positive determinant or if all its eigenvalues have negative real parts [20]. The Jacobian matrix $J(E_0)$ has two distinct negative eigenvalues given by $-\mu_1$ and $-(\omega_1+\mu_1)$. The local stability of $E_0$ is studied by examining the trace and determinant of the reduced block matrix $J(E_0^*)$ defined by;

$$J(E_0^*) = \begin{bmatrix} \frac{(\mu_1+\eta_1\omega_1)\alpha_1\beta_{h1}\Lambda_1}{\mu_1(\mu_1+\omega_1)m} - Q_1 & \frac{(\mu_1+\eta_1\omega_1)\alpha_1\beta_{e1}\Lambda_1}{\mu_1(\mu_1+\omega_1)k} \\ \alpha_1\xi_1 & -Q_2 \end{bmatrix}.$$

Using the conditions outlined in [9], let $Tr$ be the Trace and $Det$ be the Determinant of the block matrix $J(E_0^*)$. For the eigenvalues of $J(E_0^*)$ to be negative, then $Det(J(E_0^*)) > 0$ and $Tr(J(E_0^*)) < 0$. The conditions that will make this to hold are thus determined.

For $Det(J(E_0^*)) > 0$, then;

$$\frac{(\mu_1+\eta_1\omega_1)(\alpha_1\beta_{h1}\Lambda_1 kQ_2 + \alpha_1^2\beta_{e1}\Lambda_1\xi_1 m)}{\mu_1(\mu_1+\omega_1)km} < Q_1Q_2. \tag{3.4}$$

Simplifying inequality (3.4) yields;

$$\frac{(\mu_1+\eta_1\omega_1)(\alpha_1\beta_{h1}\Lambda_1 kQ_2 + \alpha_1^2\beta_{e1}\Lambda_1\xi_1 m)}{\mu_1(\mu_1+\omega_1)kQ_1Q_2m} < 1. \tag{3.5}$$

Since the LHS of inequality (3.5) equals to $R_{V1}$, the determinant of $J(E_0^*)$ can only be positive if $R_{V1} < 1$.

For $Tr(J(E_0^*)) < 0$, then;

$$\frac{\alpha_1\beta_{h1}\Lambda_1(\mu_1+\eta_1\omega_1)}{\mu_1(\mu_1+\omega_1)m} - Q_1 < 0. \tag{3.6}$$

Making $Q_1$ the subject of equation (3.2), yields;

$$Q_1 = \frac{(\mu_1+\eta_1\omega_1)(\alpha_1\beta_{h1}\Lambda_1 kQ_2 + \alpha_1^2\beta_{e1}\Lambda_1\xi_1 m)}{\mu_1(\mu_1+\omega_1)kQ_2mR_{V1}}. \tag{3.7}$$

Substituting equation (3.7) into inequality (3.6) gives;

$$\frac{\alpha_1\beta_{h1}\Lambda_1(\mu_1+\eta_1\omega_1)}{\mu_1(\mu_1+\omega_1)m} - \frac{(\mu_1+\eta_1\omega_1)(\alpha_1\beta_{h1}\Lambda_1 kQ_2 + \alpha_1^2\beta_{e1}\Lambda_1\xi_1 m)}{\mu_1(\mu_1+\omega_1)kQ_2mR_{V1}} < 0. \tag{3.8}$$

Simplifying inequality (3.8) yields;

$$\frac{\phi_1\alpha_1\Lambda_1}{\mu_1(\mu_1+\omega_1)m}\left[\beta_{h1}\left(1-\frac{1}{R_{V1}}\right) - \frac{\alpha_1\beta_{e1}\xi_1 m}{kQ_2R_{V1}}\right] < 0,$$

which can only hold if $R_{V1} < 1$, implying that the $Tr(J(E_0^*)) < 0$ if $R_{V1} < 1$. Hence, the disease free equilibrium is locally asymptotically stable if $R_{V1} < 1$. Similarly, it can also be shown that the disease free equilibrium of the second community is also locally asymptotically stable when $R_{V2} < 1$. □

### 3.2.4. Global stability of the disease free equilibrium

To investigate the global stability of the disease free equilibrium, Castillo-Chavez theorem [21] is employed. System (2.1) is rewritten in the form;

$$\begin{aligned} \frac{dX}{dt} &= F(X,Z) \\ \frac{dZ}{dt} &= G(X,Z), G(X,0) = 0, \end{aligned} \tag{3.9}$$

where $X = (S_1, V_1, S_2, V_2)$, $X \in \mathbb{R}^4$ denotes (its components) the uninfected individuals while $Z = (I_1, B_1, I_2, B_2)$, $Z \in \mathbb{R}^4$ denotes (its components) the infected individuals. $E_0 = (X^*, 0)$ is the disease free equilibrium of system (3.9). According to [21], the following conditions (H1) and (H2) must be met to guarantee local asymptotic stability of the system:
(H1) For $\frac{dX}{dt} = F(X,0)$, $X^*$ is globally asymptotically stable (g.a.s),
(H2) $G(X,Z) = AZ - \widehat{G}(X,Z)$, $\widehat{G}(X,Z) \geq 0$ for $(X,Z) \in \Omega$,
where $A = D_Z G(X^*, 0)$ is a Metzler Matrix (the off diagonal elements are nonnegative) and $\Omega$ is the region where the model makes biological sense. Castillo-Chavez theorem provides that $E_0$ will be globally asymptotically stable if it's locally asymptotically stable and satisfies (H1) and (H2).

**Theorem 3.4.** *The disease free equilibrium $(E_0)$ is locally asymptotically stable whenever $R_{Vi} < 1$ $(i = 1, 2)$.*

*Proof.* Using the above notation, we have

$$\frac{dX}{dt} = \begin{bmatrix} \frac{dS_1}{dt} = \Lambda_1 - (\omega_1+\mu_1)S_1 \\ \frac{dV_1}{dt} = \omega_1 S_1 - \mu_1 V_1 \\ \frac{dS_2}{dt} = \Lambda_2 - (\omega_2+\mu_2)S_2 \\ \frac{dV_2}{dt} = \omega_2 S_2 - \mu_2 V_2 \end{bmatrix}$$

and solving for $S_1$, $V_1$, $S_2$, $V_2$ yields $S_1(t) = \frac{\Lambda_1}{\omega_1+\mu_1} + Ce^{-(\omega_1+\mu_1)t}$; $V_1(t) = \frac{\omega_1\Lambda_1}{\mu_1(\omega_1+\mu_1)} + Ce^{-(\mu_1)t}$, $S_2 = \frac{\Lambda_2}{\omega_2+\mu_2} + Ce^{-(\omega_2+\mu_2)t}$ and $V_2(t) = \frac{\omega_2\Lambda_2}{\mu_2(\omega_2+\mu_2)} + Ce^{-(\mu_2)t}$. Therefore $\lim_{t\to\infty} X(t) = \left[\frac{\Lambda_1}{\mu_1+\omega_1}, \frac{\omega_1\Lambda_1}{\mu_1(\mu_1+\omega_1)}, \frac{\Lambda_2}{\mu_2+\omega_2}, \frac{\omega_1\Lambda_1}{\mu_1(\mu_1+\omega_1)}\right] = X^*$, implying that $X^*$ is globally asymptotically stable. Hence, condition (H1) is satisfied.
Now, the matrix $A$ is determined as:

$$A = \begin{bmatrix} \frac{\alpha_1\beta_{h1}d_1}{m} - Q_1 & \frac{\alpha_1\beta_{e1}d_1}{k} & a_2 & 0 \\ \alpha_1\xi_1 & -Q_2 & 0 & 0 \\ a_1 & 0 & \frac{\alpha_2\beta_{h2}d_2}{m} - Q_3 & \frac{\alpha_2\beta_{e2}d_2}{k} \\ 0 & 0 & \alpha_2\xi_2 & -Q_4 \end{bmatrix}$$

where $d_1 = S_1 + \eta_1 V_1$ and $d_2 = S_2 + \eta_2 V_2$;

$$AZ = \begin{bmatrix} \frac{\alpha_1\beta_{h1}d_1I_1}{m} - Q_1I_1 + \frac{\alpha_1\beta_{e1}d_1B_1}{k} + a_{21}I_2 \\ \alpha_1\xi_1I_1 - Q_2B_1 \\ a_{12}I_1 + \frac{\alpha_2\beta_{h2}d_2I_2}{m} - Q_3I_2 + \frac{\alpha_2\beta_{e2}d_2B_2}{k} \\ \alpha_2\xi_2I_2 - Q_4B_2 \end{bmatrix},$$

$$G(X,Z) = \begin{bmatrix} (\frac{\alpha_1\beta_{e1}B_1}{k+B_1} + \frac{\alpha_1\beta_{h1}I_1}{m+I_1})S_1 + \eta_1(\frac{\alpha_1\beta_{e1}B_1}{k+B_1} + \frac{\alpha_1\beta_{h1}I_1}{m+I_1})V_1 + a_{21}I_2 - Q_1I_1 \\ \alpha_1\xi_1I_1 - Q_2B_1 \\ (\frac{\alpha_2\beta_{e2}B_2}{k+B_2} + \frac{\alpha_2\beta_{h2}I_2}{m+I_2})S_2 + \eta_2(\frac{\alpha_2\beta_{e2}B_2}{k+B_2} + \frac{\alpha_2\beta_{h2}I_2}{m+I_2})V_2 + a_{12}I_1 - Q_3I_2 \\ \alpha_2\xi_2I_2 - Q_4B_2 \end{bmatrix},$$

and

$$\widehat{G}(X,Z) = \begin{bmatrix} \frac{\alpha_1\beta_{h1}I_1^2S_1}{m(m+I_1)} + \frac{\eta_1\alpha_1\beta_{h1}I_1^2V_1}{m(m+I_1)} + \frac{\alpha_1\beta_{e1}B_1^2S_1}{k(k+B_1)} + \frac{\eta_1\alpha_1\beta_{e1}B_1^2V_1}{k(k+B_1)} \\ 0 \\ \frac{\alpha_2\beta_{h2}I_2^2S_2}{m(m+I_2)} + \frac{\eta_2\alpha_2\beta_{h2}I_2^2V_2}{m(m+I_2)} + \frac{\alpha_2\beta_{e2}B_2^2S_2}{k(k+B_2)} + \frac{\eta_2\alpha_2\beta_{e2}B_2^2V_2}{k(k+B_2)} \\ 0 \end{bmatrix}.$$

Therefore $\widehat{G}(X,Z) = AZ - G(X,Z) \geq 0$ as all the parameters used are positive and $0 < \alpha_i, \eta_i < 1$ for $i = 1,2$; implying that the condition(H2) has been met as well. Since $E_0$ is locally asymptotically stable if $R_{Vi} < 1$ $(i = 1,2)$ and the conditions (H1) and (H2) are satisfied, it follows from Castillo-Chavez theorem that $E_0$ is globally asymptotically stable equilibrium of model (2.1) whenever $R_{Vi} < 1$. □

### 3.2.5. Boundary endemic steady state

The model has boundary endemic equilibrium point when the infection is persistent in one community but is absent in the other. The boundary endemic equilibrium points are obtained by setting the equations of system (2.1) to zero. Note that at the first boundary endemic equilibrium point $E_1 = (S_1^*, V_1^*, I_1^*, B_1^*, S_2, V_2, 0, 0)$, the disease is persistent only in the first community and at the second boundary endemic equilibrium point $E_2 = (S_1, V_1, 0, 0, S_2^*, V_2^*, I_2^*, B_2^*)$, the disease is persistent only in the second community.

**Theorem 3.5.** *The first boundary endemic equilibrium point $(E_1)$ exists provided that $R_{V1} > 1$.*

*Proof.* For the existence of the first boundary endemic equilibrium, the equations of system (2.1) at $E_1$ becomes;

$$\begin{aligned} 0 &= \Lambda_1 - \omega_1 S_1 - \lambda_{e1}S_1 - \lambda_{h1}S_1 - \mu_1 S_1 \\ 0 &= \omega_1 S_1 - \eta_1[\lambda_{e1}V_1 + \lambda_{h1}V_1] - \mu_1 V_1 \\ 0 &= \lambda_{e1}S_1 + \lambda_{h1}S_1 + \eta_1[\lambda_{e1}V_1 + \lambda_{h1}V_1] - Q_1I_1 \\ 0 &= \alpha_1\xi_1 I_1 - Q_2B_1 \\ 0 &= \Lambda_2 - \omega_2 S_2 - \mu_2 S_2 \\ 0 &= \omega_2 S_2 - \mu_2 V_2. \end{aligned} \tag{3.10}$$

From the fourth equation of system (3.10), we get;

$$B_1^* = \frac{\alpha_1\xi_1 I_1}{Q_2}. \tag{3.11}$$

Substituting equation (3.11) and the limiting values of $S_1$ and $V_1$ into the third equation of system (3.10) and solving yields;

$$AI_1^{*3} + BI_1^{*2} + CI_1^* = 0, \tag{3.12}$$

where

$$\begin{aligned} A &= -\alpha_1\xi_1\mu_1\tau_1Q_1 \\ B &= \phi_1(\alpha_1^2\beta_{e1}\Lambda_1\xi_1 + \alpha_1^2\beta_{h1}\Lambda_1\xi_1) - \mu_1\tau_1Q_1(kQ_2 + \alpha_1\xi_1 m) \\ C &= \phi_1(\alpha_1^2\beta_{e1}\Lambda_1\xi_1 m + \alpha_1\beta_{h1}\Lambda_1 kQ_2) - kQ_2m\mu_1Q_1\tau_1 \\ \tau_1 &= \mu_1 + \omega_1 \\ \phi_1 &= \mu_1 + \eta_1\omega_1. \end{aligned}$$

From equation (3.12), $I_1^* = 0$ is one of the solutions of system (2.1). This corresponds to the disease free equilibrium $E_0$ and the other solutions when $I_1^* \neq 0$ gives the relationship between the susceptible, the vaccinated and the infected individuals in the first community. Thus

$$AI_1^{*2} + BI_1^* + C = 0, \tag{3.13}$$

is now considered. The first boundary endemic equilibrium of the system exists if the roots of equation (3.13) are real and positive. Descartes' rule of signs is used to check the possible number of real roots of the polynomial. The number of positive real roots of a polynomial is equal to the number of sign changes in the coefficients of the terms. The coefficients of equation (3.13) are analyzed by first checking the sign of $A$. Since all the parameters used are positive, the sign of $A$ is negative. Next the sign of $C$ is checked by considering;

$$C = \phi_1(\alpha_1^2\beta_{e1}\Lambda_1\xi_1 m + \alpha_1\beta_{h1}\Lambda_1 kQ_2) - kQ_2 m\mu_1 Q_1\tau_1$$

which may be expressed as;

$$C = [\frac{\phi_1(\alpha_1^2\beta_{e1}\Lambda_1\xi_1 m + \alpha_1\beta_{h1}\Lambda_1 kQ_2)}{kQ_2 m\mu_1 Q_1\tau_1} - 1]kQ_2 m\mu_1 Q_1\tau_1. \tag{3.14}$$

Substituting equation (3.3) into equation (3.14) yields;

$$C = [R_{V1} - 1]kQ_2 m\mu_1 Q_1\tau_1.$$

Thus $C > 0$ iff $R_{V1} > 1$. Since $A$ is negative and $C$ is positive, it implies that there is at least one sign change regardless of the sign of $B$. Therefore, equation (3.13) has at least one positive real root. Hence, the first boundary endemic equilibrium point $E_1$ exists. Similarly, it can be shown that the second boundary endemic equilibrium point $(E_2)$, also exists when $R_{V2} > 1$. □

### 3.2.6. Local stability of the first boundary endemic steady state $(E_1)$

Cholera is endemic or persistent in the first community if $S_1^*, V_1^*, I_1^*, B_1^* > 0$ for all $t > 0$. The local stability of the first boundary endemic steady state analysis is given in the following theorem,

**Theorem 3.6.** *The first boundary endemic equilibrium of system* (2.1) *is locally asymptotically stable when* $R_{V1} > 1$.

*Proof.* For the first boundary endemic equilibrium point to be stable, then the eigenvalues of it's Jacobian matrix evaluated at $E_1$, must have negative real parts. The Jacobian matrix evaluated at $E_1$ is given by;

$$J(E_1) = \begin{bmatrix} -f_0 & 0 & -f_1 & -f_2 & 0 & 0 \\ \omega_1 & -f_3 & -f_4 & -f_5 & 0 & 0 \\ f_6 & f_7 & f_8 - Q_1 & f_9 & 0 & 0 \\ 0 & 0 & \alpha_1\xi_1 & -Q_2 & 0 & 0 \\ 0 & 0 & 0 & 0 & -(\mu_2+\omega_2) & 0 \\ 0 & 0 & 0 & 0 & \omega_2 & -\mu_2 \end{bmatrix},$$

where

$$f_0 = \omega_1 + \mu_1 + \frac{\alpha_1\beta_{e1}B_1}{k+B_1} + \frac{\alpha_1\beta_{h1}I_1}{m+I_1} \qquad f_1 = \frac{\alpha_1\beta_{h1}\Lambda_1 m}{(\mu_1+\omega_1)(m+I_1)^2}$$
$$f_2 = \frac{\alpha_1\beta_{e1}\Lambda_1 k}{(\mu_1+\omega_1)(k+B_1)^2} \qquad f_3 = \mu_1 + \frac{\eta_1\alpha_1\beta_{e1}B_1}{k+B_1} + \frac{\eta_1\alpha_1\beta_{h1}I_1}{m+I_1}$$
$$f_4 = \frac{\eta_1\alpha_1\beta_{h1}\Lambda_1\omega_1 m}{\mu_1(\mu_1+\omega_1)(m+I_1)^2} \qquad f_5 = \frac{\eta_1\alpha_1\beta_{e1}\Lambda_1\omega_1 k}{\mu_1(\mu_1+\omega_1)(k+B_1)^2}$$
$$f_6 = \frac{\alpha_1\beta_{e1}B_1}{k+B_1} + \frac{\alpha_1\beta_{h1}I_1}{m+I_1} \qquad f_7 = \frac{\eta_1\alpha_1\beta_{e1}B_1}{k+B_1} + \frac{\eta_1\alpha_1\beta_{h1}I_1}{m+I_1}$$
$$f_8 = \frac{\alpha_1\beta_{h1}\Lambda_1 m\phi_1}{\mu_1(\mu_1+\omega_1)(m+I_1^*)^2} \qquad f_9 = \frac{\alpha_1\beta_{e1}\Lambda_1\phi_1 k}{\mu_1(\mu_1+\omega_1)(k+B_1)^2}.$$

Clearly, the Jacobian matrix $J(E_1)$ has two distinct negative eigenvalues given by $-(\mu_2)$ and $-(\mu_2+\omega_2)$. The local stability is therefore established by computing its other eigenvalues which involves the solution of the system given by;

$$\begin{vmatrix} \lambda + f_0 & 0 & -f_1 & -f_2 \\ \omega_1 & \lambda + f_3 & -f_4 & -f_5 \\ f_6 & f_7 & \lambda - (f_8 + Q_1) & f_9 \\ 0 & 0 & \alpha_1\xi_1 & \lambda + Q_2 \end{vmatrix} = 0. \tag{3.15}$$

The characteristic equation of equation (3.15) is given by;

$$\lambda^4 + a_0\lambda^3 + a_1\lambda^2 + a_2\lambda + a_3 = 0, \tag{3.16}$$

where
$a_0 = f_0 + f_3 + Q_1 + Q_2 - f_8$

$$a_1 = f_0f_3 + f_1f_6 + f_4f_7 + f_0Q_1 + f_3Q_1 + f_0Q_2 + f_3Q_2 + Q_1Q_2 - f_8Q_2 - f_0f_8 - f_3f_8 - \alpha_1\xi_1f_9$$

$$a_2 = f_1f_3f_6 + f_0f_4f_7 - f_0f_3f_8 + f_0f_3Q_1 + f_0f_3Q_2 + f_1f_6Q_2 + f_4f_7Q_2 - f_0f_8Q_2 - f_3f_8Q_2 + f_0Q_1Q_2 + f_3Q_1Q_2 + \alpha_1\xi_1f_2f_6 + \alpha_1\xi_1f_5f_7 - \alpha_1\xi_1f_0f_9 - \alpha_1\xi_1f_3f_9 + \omega_1f_1f_7$$

$$a_3 = f_1f_3f_6Q_2 + f_0f_4f_7Q_2 - f_0f_3f_8Q_2 + f_0f_3Q_1Q_2 + \alpha_1\xi_1f_2f_3f_6 + \alpha_1\xi_1f_0f_5f_7 - \alpha_1\xi_1f_0f_3f_9 + \omega_1f_1f_7Q_2 + \alpha_1\xi_1\omega_1f_2f_7.$$

The number of possible negative zeros of equation (3.16) depends on the signs of $a_0$, $a_1$, $a_2$ and $a_3$. This can be analysed using Descartes' Rule of Signs of the polynomial given by;

$$P(\lambda) \quad = \quad a_0\lambda^3 + a_1\lambda^2 + a_2\lambda + a_3 = 0. \tag{3.17}$$

From this Rule, the number of negative real zeros of $P(\lambda)$ is either equal to the variations in sign of $P(-\lambda)$ or less than this by an even number. The possibilities of the negative roots of equation (3.17) is as summarized in Table 1.

**Table 3.1:** The Zeros of Characteristic equation (29).

| Cases | $a_0$ | $a_1$ | $a_2$ | $a_3$ | $R_{V1} > 1$ | Sign Change | No. of $-$ Roots |
|---|---|---|---|---|---|---|---|
| 1 | $+$ | $-$ | $-$ | $+$ | $R_{V1} > 1$ | 2 | 2,0 |
| 2 | $+$ | $-$ | $+$ | $+$ | $R_{V1} > 1$ | 2 | 2,0 |
| 3 | $-$ | $-$ | $+$ | $-$ | $R_{V1} > 1$ | 2 | 2,0 |
| 4 | $+$ | $+$ | $-$ | $-$ | $R_{V1} > 1$ | 1 | 0 |
| 5 | $-$ | $-$ | $+$ | $+$ | $R_{V1} > 1$ | 1 | 0 |
| 6 | $+$ | $+$ | $+$ | $-$ | $R_{V1} > 1$ | 1 | 0 |
| 7 | $-$ | $+$ | $-$ | $+$ | $R_{V1} > 1$ | 3 | 3,1 |
| 8 | $-$ | $-$ | $-$ | $-$ | $R_{V1} > 1$ | 0 | 0 |

From the table, the maximum number of variations of sign in $P(-\lambda)$ is three, hence, polynomial (3.17) has three negative roots. Thus, $J(E_1)$ has five negative real zeros. Therefore, system (2.1) is locally asymptotically stable if $R_{V2} < 1$. Clearly, the second boundary endemic steady state is also locally asymptotically stable if $R_{V1} < 1$. □

### 3.2.7. Interior endemic equilibrium point

The model system has a non-trivial equilibrium point in the presence of infection in both communities, known as Interior Endemic equilibrium point given by $E_3 = (S_1^*, V_1^*, I_1^*, B_1^*, S_2^*, V_2^*, I_2^*, B_2^*) \in \mathbb{R}_+^8$. This is the point when $I_i^* > 0$ and $B_i^* > 0$ for $i = 1, 2$, in the two communities.

**Theorem 3.7.** *The interior endemic equilibrium point exists provided $R_{Vi} > 1$ $(i = 1, 2)$.*

*Proof.* At the interior endemic equilibrium point;

$$\begin{aligned}
0 &< (\frac{\alpha_1\beta_{e1}B_1^*}{k+B_1^*} + \frac{\alpha_1\beta_{h1}I_1^*}{m+I_1^*})S_1 + \eta_1(\frac{\alpha_1\beta_{e1}B_1^*}{k+B_1^*} + \frac{\alpha_1\beta_{h1}I_1^*}{m+I_1^*})V_1 - Q_1I_1^* \\
0 &< \alpha_1\xi_1I_1^* - Q_2B_1^* \\
0 &< (\frac{\alpha_2\beta_{e2}B_2^*}{k+B_2^*} + \frac{\alpha_2\beta_{h2}I_2^*}{m+I_2^*})S_2 + \eta_2(\frac{\alpha_2\beta_{e2}B_2^*}{k+B_2^*} + \frac{\alpha_2\beta_{h2}I_2^*}{m+I_2^*})V_2 - Q_3I_2^* \\
0 &< \alpha_2\xi_2I_2^* - Q_4B_2^*.
\end{aligned} \tag{3.18}$$

From the second and fourth equations of inequality (3.18), we obtain;

$$\begin{aligned}
B_1^* &< \frac{\alpha_1\xi_1I_1^*}{Q_2} \\
B_2^* &< \frac{\alpha_2\xi_2I_2^*}{Q_4}.
\end{aligned}$$

Substituting equation (3.11) and the limiting values of $S_1$ and $V_1$ into the second equation of inequality (3.18) and solving for $I_1^*$ yields equation (3.12) which had been shown to have at least one positive real root in Theorem 3.3. Hence, $I_1^* > 0$ when $R_{V1} > 1$. It is also clear that $I_2^* > 0$ when $R_{V2} > 1$. These imply that $B_1^* > 0$ and $B_2^* > 0$. Therefore the interior endemic equilibrium point $(E_3)$ exists when $R_{V1} > 1$ and $R_{V2} > 1$. □

### 3.2.8. Local stability of the interior endemic steady state

The local stability of the interior endemic equilibrium point is given in the following theorem,

**Theorem 3.8.** *The interior endemic equilibrium of system (2.1) is locally asymptotically stable when $R_{Vi} > 1$ $(i = 1, 2)$.*

*Proof.* To investigate the local stability of the interior endemic equilibrium point $(E_3)$, the model system (2.1) is linearized at $E_3$. The Jacobian matrix at $E_3$ is given by;

$$J(E_3) = \begin{bmatrix} -f_0 & 0 & -f_1 & -f_2 & 0 & 0 & 0 & 0 \\ \omega_1 & -f_3 & -f_4 & -f_5 & 0 & 0 & 0 & 0 \\ f_6 & f_7 & f_8 - Q_1 & f_9 & 0 & 0 & a_2 & 0 \\ 0 & 0 & \alpha_1\xi_1 & -Q_2 & 0 & 0 & 0 & 0 \\ 0 & 0 & 0 & 0 & -g_0 & 0 & -g_1 & -g_2 \\ 0 & 0 & 0 & 0 & \omega_2 & -g_3 & -g_4 & -g_5 \\ 0 & 0 & a_1 & 0 & g_6 & g_7 & g_8 - Q_3 & f_9 \\ 0 & 0 & 0 & 0 & 0 & 0 & \alpha_2\xi_2 & -Q_4 \end{bmatrix},$$

where

$$g_0 = \omega_2 + \mu_2 + \frac{\alpha_2\beta_{e2}B_2}{k+B_2} + \frac{\alpha_2\beta_{h2}I_2}{m+I_2} \qquad g_1 = \frac{\alpha_2\beta_{h2}\Lambda_2 m}{(\mu_2+\omega_2)(m+I_2)^2}$$

$$g_2 = \frac{\alpha_2\beta_{e2}\Lambda_2 k}{(\mu_2+\omega_2)(k+B_2)^2} \qquad g_3 = \mu_2 + \frac{\eta_2\alpha_2\beta_{e2}B_2}{k+B_2} + \frac{\eta_2\alpha_2\beta_{h2}I_2}{m+I_2}$$

$$g_4 = \frac{\eta_2\alpha_2\beta_{h2}\Lambda_2\omega_2 m}{\mu_2(\mu_2+\omega_2)(m+I_2)^2} \qquad g_5 = \frac{\eta_2\alpha_2\beta_{e2}\Lambda_2\omega_2 k}{\mu_2(\mu_2+\omega_2)(k+B_2)^2}$$

$$g_6 = \frac{\alpha_2\beta_{e2}B_2}{k+B_2} + \frac{\alpha_2\beta_{h1}I_2}{m+I_2} \qquad g_7 = \frac{\eta_2\alpha_2\beta_{e2}B_2}{k+B_2} + \frac{\eta_2\alpha_2\beta_{h2}I_2}{m+I_2}$$

$$g_8 = \frac{\alpha_2\beta_{h2}\Lambda_2 m\phi_2}{\mu_2(\mu_2+\omega_2)(m+I_2^*)^2} \qquad g_9 = \frac{\alpha_2\beta_{e2}\Lambda_2\phi_2 k}{\mu_2(\mu_2+\omega_2)(k+B_2)^2}.$$

The Jacobian matrix $J(E_3)$ can be re-written in the form;

$$J(E_3) = \begin{bmatrix} J_{11} & J_{12} \\ J_{21} & J_{22} \end{bmatrix},$$

where;

$$J_{11} = \begin{bmatrix} -f_0 & 0 & -f_1 & -f_2 \\ \omega_1 & -f_3 & -f_4 & -f_5 \\ f_6 & f_7 & f_8 - Q_1 & f_9 \\ 0 & 0 & \alpha_1\xi_1 & -Q_2 \end{bmatrix}$$

and

$$J_{22} = \begin{bmatrix} -g_0 & 0 & -g_1 & -g_2 \\ \omega_2 & -g_3 & -g_4 & -g_5 \\ g_6 & g_7 & g_8 - Q_3 & g_9 \\ 0 & 0 & \alpha_2\xi_2 & -Q_4 \end{bmatrix}.$$

It's clear that $J_{11}$ and $J_{22}$ have negative real roots hence, $J(E_3)$ has negative real zeros and the interior endemic equilibrium point $(E_3)$ is locally asymptotically stable. □

## 4. Numerical Simulations

Numerical Simulations to validate the analytical findings and illustrate the long term dynamics of system (2.1) have been performed using MATLAB. This has been achieved by using parameter values which have been selected from some published literatures as shown in Table 4.1. The parameter values in Table 4.1 give $R_{V1} = 0.422452 < 1$ and $R_{V2} = 0.240175 < 1$. The results of the simulations are presented in the figures below where$I(t)$ and $B(t)$ are the number of infected individuals and the concentration of Vibrio cholerae in aquatic reservoirs in the two communities at time t respectively.

When $R_V < 1$, all the trajectories of the infected population and the concentration of *Vibrios* converge to zero regardless of the presence of intervention strategies as shown in Figure 4.1 and Figure 4.2. This pinpoints that the cholera free state can only be asymptotically stable in line with Theorem 3.3. It also shows that the epidemic size is greatly reduced when vaccination and media awareness are simultaneously deployed.

Figure 4.3 shows that both vaccination and media awareness lower the spread of cholera with time, and that each has an inverse relationship with the spread of the disease. Therefore the rates of vaccination and media awareness should be heightened in order to reduce the outbreak size and duration. Evidently, the effect of media awareness is higher in the control of cholera and it's notable that they should be applied from the start of an outbreak in order to pare the transmission of cholera in any population.

It is also evident from Figure 4.4 that vaccination and media awareness lowers the disease spread, with the first community experiencing earlier disease extinction. This clearly illustrates that the effects of the intervention strategies are unidentical in the two communities and that movement across the communities will lead to re-introduction of the disease in the community where it had been eradicated.

Figure 4.5 shows that migration affects the rate of change of the infected population since, when the rate of movement into the first/second community is higher than the movement out, then the rate of change of the infected individuals increases and vice versa. This attests the fact that migration is a vital factor in the transmission of cholera and hence, movement across cholera hit communities should be circumvented.

**Table 4.1:** Model Parameters and Values.

| Parameter | Symbol | Value | Source |
|---|---|---|---|
| Recruitment rate into community $i$ | $\Lambda_i$ | $9.6274 * 10^{-5}$ $(/day)$ | [9] |
| Vaccination rate in community $i$ | $\omega_i$ | 0.78 $(/day)$ | *Varies* |
| Vaccine efficacy in community $i$ | $\sigma_i$ | 0.68 $(/day)$ | *Estimate* |
| *Vibrios* ingestion rate in community 1 | $\beta_{e1}$ | 0.075 $(/day)$ | [26] |
| *Vibrios* ingestion rate in community 2 | $\beta_{e2}$ | 0.01694 $(/day)$ | [29] |
| Rate of contact with infectives in com. 1 | $\beta_{h1}$ | 0.0005 $(/day)$ | [25] |
| Rate of contact with infectives in com. 2 | $\beta_{h2}$ | 0.00125 $(/day)$ | *Estimate* |
| Efficacy of media awareness in com. $i$ | $\rho_i$ | 0.75 | *Varies* |
| Half saturation constant of the pathogen | $k$ | $10^6$ $cells/l$ | *Estimate* |
| Minimum contact rate with the infected | $m$ | 0.00001 | *aries* |
| Natural death rate in community 1 | $\mu_1$ | 0.02 $(/day)$ | [22],[28] |
| Natural death rate in community 2 | $\mu_2$ | $5.48 * 10^{-5}$ $(/day)$ | [27] |
| Rate of recovery in community 1 | $\gamma_1$ | 0.015 $(/day)$ | [24] |
| Rate of recovery in community 2 | $\gamma_2$ | 0.2 $(/day)$ | [29] |
| Disease induced mortality rate in com. 1 | $\delta_1$ | 0.013 $(/day)$ | [23] |
| Disease induced mortality rate in com. 2 | $\delta_2$ | $4.0 * 10^{-4}$ $(/day)$ | [9] |
| Rate of shedding of *Vibrios* in com. $i$ | $\xi_i$ | 50 $(/day)$ | [10] |
| Decay rate of pathogen in com. $i$ | $\mu_{ip}$ | 1.06 $(/day)$ | [10],[27] |
| Multiplication rate of *Vibrios* in com. $i$ | $g_i$ | 0.73 $(/day)$ | [10],[27] |

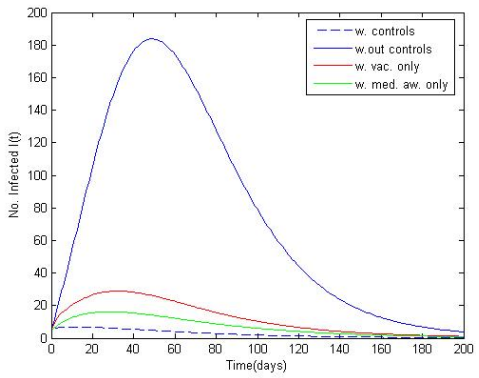


**Figure 4.1:** The number of infectives.

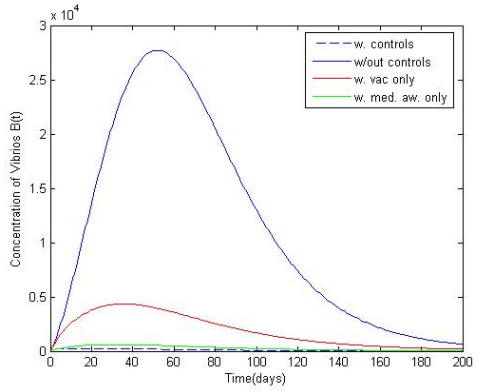


**Figure 4.2:** The concentration of *Vibrios*.

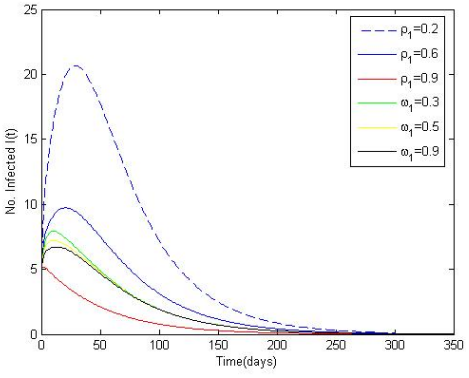


**Figure 4.3:** The number of infectives when varying $\rho$ and $\omega$.

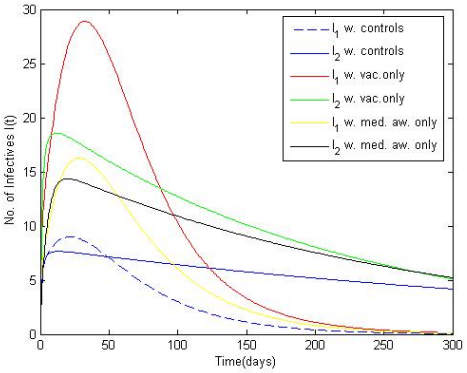


**Figure 4.4:** The number of infectives with and without controls in the two communities.

## 5. Conclusion

A metapopulation model for cholera with imperfect vaccine and variable media awareness was developed and analysed to investigate the long term transmission dynamics of cholera, in the presence of these control strategies.

The analytical results of the model indicated that there is a region where the model is mathematically and epidemiologically well posed since its solutions were positive and bounded. The vaccine reproduction numbers for the two isolated communities were computed using the next generation matrix approach. It was also shown that there was no disease transmission when the reproduction numbers were below unity. Stability analysis of the model exhibited that the disease free equilibrium is both locally and globally asymptotically stable when $R_{Vi} < 1$ $(i = 1,2)$. The model was shown to have four endemic equilibria which were shown to be locally asymptotically stable when $R_{Vi} > 1$.

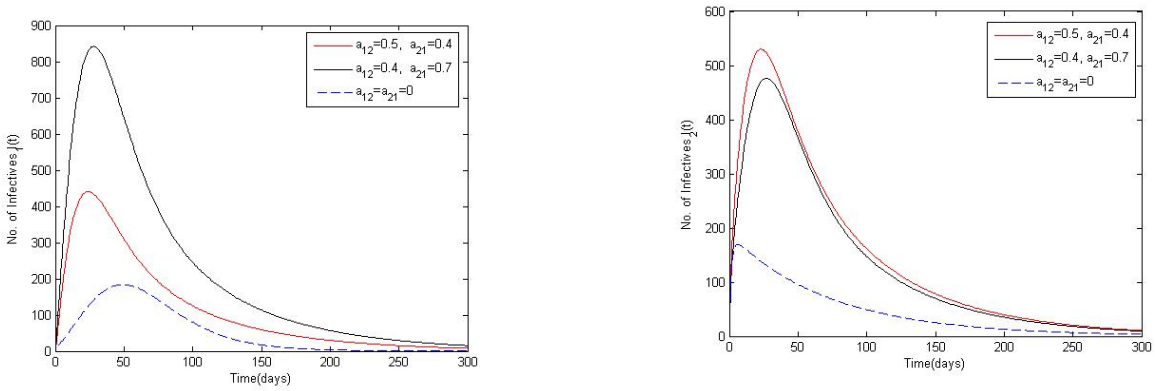


**Figure 4.5:** The rate of change of the infectives when varying the migration parameters.

From the numerical simulations, it was evident that migration of the infected individuals across communities during epidemics, greatly increased the spread of cholera in the two communities. Evidently, effective media awareness and vaccination have also been shown to lower the disease spread resulting into a faster elimination of cholera in the two communities with the first community experiencing earlier disease extinction. This asserts that, the effects of the intervention strategies are unidentical in the two communities and that even with imperfect vaccine, the spread of cholera is greatly pared. Since optimal control and cost effectiveness of vaccination and media awareness have not been done, this can be explored as a future work, to determine the intervention strategy with the least cost and highest efficiency.

## Article Information

**Acknowledgements:** The authors would like to express their sincere thanks to the editor and the anonymous reviewers for their helpful comments and suggestions.

**Author's contributions:** All authors contributed equally to the writing of this paper. All authors read and approved the final manuscript.

**Conflict of Interest Disclosure:** No potential conflict of interest was declared by the authors.



**Supporting/Supporting Organizations:** No grants were received from any public, private or non-profit organizations for this research.

**Ethical Approval and Participant Consent:** It is declared that during the preparation process of this study, scientific and ethical principles were followed and all the studies benefited from are stated in the bibliography.

**Plagiarism Statement:** This article was scanned by the plagiarism program. No plagiarism detected.

## References

[1] WHO, *Cholera Vaccines: WHO position paper - August 2017*, Weekly Epidemological Record, **92**(34) (2017), 477-500.
[2] B. Dumitru, A. Fahimeh, J. Juan, J. Amin, *On a new and generalized fractional model for a real cholera outbreak,* Alex. Eng. J., **61**(11) (2022), 9175 - 9186.
[3] C. Eric, N. Eric, L. Suzanne, Y. Abdul - Aziz, *Mathematical modeling of the influence of cultural practices on cholera infection in Cameroon,* Math. Biosci. Eng., **18**(6) (2021), 8374-8391.
[4] Cholera Vaccines, *WHO position paper,* Weekly Epidemiological Record, **85**(13) (2010),117.
[5] D. Sur et. al., *Efficacy and safety of a modified killed-whole-cell oral cholera vaccine in India: an interim analysis of a cluster-randomised, double-blind, placebo-controlled trial,* Lancet, **374**(9702) (2009), 1694-1702.
[6] E. Marcelino et. al., *Effectiveness of mass cholera vaccination in Beira, Mozambique,* N. Engl. J. Med., **352**(8) (2005), 757-767.
[7] Cholera, *V. Cholerae Infection in Africa*, Available at www.cdc.gov
[8] N. Hellen, O. Emmanuel, L. Livingstone, *Modeling optimal control of cholera disease under the interventions of vaccination, treatment and education awareness,* J. Math. Res., **10**(5) (2018), 137-152.
[9] B. Musundi, G. Lawi, F. Nyamwala, *Mathematical analysis of a cholera transmission model incorporating media coverage,* Int. J. Pure Appl. Math., **111**(2) (2016), 219 - 231.
[10] J. Njagarah, F. Nyabadza, *Modelling optimal control of cholera in communities linked by migration,* Comput. Math. Methods Med., (2015), Article ID 898264.
[11] L. Rachael, N. Miller, S. Elsa, G. Holly, K. Renee, L. Suzanne, *Modeling optimal intervention strategies for cholera,* Bull. Math. Biol., **72** (2010), 2004–2018.
[12] R. Michael, H. Joseph, C. Marisa, L. Suzanne, *The impact of spatial arrangements on epidemic disease dynamics and intervention strategies,* J. Biol. Dyn., **10**(1) (2016), 222–249.
[13] P. Amadi, *A Metapopulation Model for Cholera with Variable Media Efficacy and Imperfect Vaccine,* MSc Thesis, Maseno University (2021).
[14] Z. Xueyong, S. Xiangyun, W. Ming, *Stochastic modeling with optimal control: Dynamical behavior and optimal control of a stochastic mathematical model for cholera,* Chaos, Solutions and Fractals, **156** (2022), 111854.
[15] M. Mehmet, B. Zafer, K. Tulay, K. Tahir, *Transmission of cholera disease with Laplacian and triangular parameters,* IJMSI, **17**(2) (2022), 289-305.
[16] P. Prabir, K. Shyamal, C. Joydev, *Dynamical study in fuzzy threshold dynamics of a cholera epidemic model,* Fuzzy Inf. Eng., **9**(3) (2017), 381-401.
[17] J. Harris, *Cholera: Immunity and prospects in vaccine development,* J. Infect. Dis., **218**(3) (2018), 141-146 .
[18] C. Codeco, *Endemic and epidemic dynamics of cholera: The role of the aquatic reservoir,* BMC Infect. Dis., **1**(1) (2001). DOI:10.1186/1471-2334-1-1.
[19] P. Driessche, W. James, *Reproduction numbers and sub-threshold endemic equilibria for compartmental models of disease transmission,* Math. Biosci., **180** (2002), 29-48.

[20] C. Leopard, K. Damian, A. Emmanuel, *Modeling and stability analysis for measles metapopulation model with vaccination,* Appl. Comput. Math., **4**(6) (2015), 431-444.
[21] C. Castillo-Chavez, Z. Feng, W. Huang, *On the computation of $R_0$ and its role on global stability,* Mathematical Approaches for Emerging and Reemerging Infectious Diseases, **125** (2002), 229-250.
[22] J. Njagarah, F. Nyabudza, *A metapopulation model for cholera transmission dynamics between communities linked by migration,* Appl. Math. Comput., **241** (2014), 317 - 331.
[23] C. Jing'an, W. Zhanmin, Z. Xueyong, *Mathematical analysis of a cholera model with vaccination,* J. Appl. Math, **2014**, Article ID 324767, 16 pages.
[24] M. Jennifer, N. Farai, M. Josiah, *Modelling cholera transmission dynamics in the presence of limited resources,* BMC Res. Notes, **12**(475) (2019).
[25] H. Nyaberi, D. Malonza, *Mathematical model of cholera transmission with education campaign and treatment through quarantine,* J. Adv. Math. Comput., **32**(3) (2019), 1-12.
[26] J. Wang, M. Charairat, *Modeling cholera dynamics with controls,* Can. Appl. Math. Q., **19**(3) (2011).
[27] M. Al-Arydah, A. Mwasa, J. Tchuenche, *Modelling cholera disease with education and chlorination,* J. Biol. Syst., **21**(4) (2013), Article number 1340007.
[28] M. Yanli, L. Jia-Bao, L. Haixia, *Global dynamics of an SIQR model with vaccination and elimination hybrid strategies,* Mathematics, **6**(12), (2018), 328.
[29] P. Ana, J. Cristiana, F. Delfim, *A cholera mathematical model with vaccination and the biggest outbreak of world's history,* AIMS Mathematics, **3**(4)(2018), 448 - 463.

*Journal of Mathematical Sciences and Modelling*, 7(1) (2024) 33-44
*Research Article*

**Journal of Mathematical Sciences and Modelling**

*Journal Homepage: www.dergipark.gov.tr/jmsm*
*ISSN 2636-8692*
*DOI: http://dx.doi.org/10.33187/jmsm.1417160*

# Improving Tuberculosis Diagnosis using Explainable Artificial Intelligence in Medical Imaging

**Cem Özkurt**[1,2]

[1]*Department of Computer Engineering, Faculty of Technology,Sakarya University of Applied Science, Sakarya, Turkey*
[2]*AI and Data Science Research and Application Center, Sakarya University of Applied Science, Sakarya, Turkey*

**Article Info**

***Keywords:*** *Artificial Intelligence, Deep Learning, Explainable AI, Medical Imaging, Tuberculosis Diagnosis*
***2010 AMS:*** *68T07, 68T10*
***Received:*** *9 January 2024*
***Accepted:*** *1 March 2024*
***Available online:*** *9 March 2024*

**Abstract**

The integration of artificial intelligence (AI) applications in the healthcare sector is ushering in a significant transformation, particularly in developing more effective strategies for early diagnosis and treatment of contagious diseases like tuberculosis. Tuberculosis, a global public health challenge, demands swift interventions to prevent its spread. While deep learning and image processing techniques show potential in extracting meaningful insights from complex radiological images, their accuracy is often scrutinized due to a lack of explainability.

This research navigates the intersection of AI and tuberculosis diagnosis by focusing on explainable artificial intelligence (XAI). A meticulously designed deep learning model for tuberculosis detection is introduced alongside an exploration of XAI to unravel complex decisions.

The core belief is that XAI, by elucidating diagnostic decision rationale, enhances the reliability of AI in clinical settings. Emphasizing the pivotal role of XAI in tuberculosis diagnosis, this study aims to impact future research and practical implementations, fostering the adoption of AI-driven disease diagnosis methodologies for global health improvement.

## 1. Introduction

In today's healthcare landscape, the integration of artificial intelligence (AI) applications is heralding a significant transformation. This transformation is particularly focused on developing more effective strategies for the early diagnosis and treatment of contagious diseases, such as tuberculosis. Tuberculosis, as a global public health challenge, requires rapid diagnosis and effective treatment to prevent its spread. In this context, the potent capabilities of deep learning and image processing techniques to extract meaningful insights from complex radiological images come to the forefront. However, the accuracy of these sophisticated models and their roles in disease diagnosis processes are frequently scrutinized due to a lack of explainability.

This research endeavors to navigate the intersection of AI and tuberculosis diagnosis by delving into the realm of explainable artificial intelligence (XAI). The study is grounded in the premise that elucidating the decision-making processes of AI models is imperative, especially in critical domains like healthcare. Our exploration unfolds with the introduction of a meticulously designed deep learning model tailored for tuberculosis detection. Concurrently, in this study an investigative journey into the realm of XAI is embarked upon, with methods being sought to unravel the intricate decisions formulated by the model.

The crux of our inquiry lies in the conviction that XAI, by shedding light on the rationale behind diagnostic decisions, holds the potential to augment the dependability and acceptance of AI applications in clinical settings. By accentuating the pivotal role of explainable artificial intelligence in the context of tuberculosis diagnosis, this study aspires to cast a meaningful ripple effect on forthcoming research endeavors and practical implementations in the field. The broader embrace of AI-driven methodologies for disease diagnosis holds promise in advancing global initiatives aimed at curtailing the impact of tuberculosis through the optimization of early intervention and treatment protocols.

*Email address and ORCID number*: cemozkurt@subu.edu.tr, 0000-0002-1251-7715
**Cite as "Cem Özkurt, *Improving Tuberculosis Diagnosis using Explainable Artificial Intelligence in Medical Imaging*, J. Math. Sci. Model., 7(1) (2024), 33-44"**

## 2. Related Works

The TX-CNN method is a proposed approach for detecting tuberculosis in chest X-ray images [1]. In this method, convolutional neural networks are trained to learn and detect the characteristic features of TB in chest X-ray images. It is believed that TX-CNN has the potential to surpass existing methods in TB screening and diagnosis.

Pre-trained CNNs are convolutional neural networks trained on large datasets beforehand and successful in general object recognition tasks. In this study, pre-trained CNNs have been utilized as feature extractors for TB detection, and competitive results have been achieved when used for this purpose [2]. Pre-trained models can be trained with less labeled data and can yield successful results on more general datasets as well. Due to these characteristics, they require fewer computational resources and can be applied more quickly compared to models trained from scratch, especially for specific tasks such as TB detection.

The potential of XAI within the industry has been thoroughly examined, particularly focusing on the implementation of natural language processing solutions at companies like Trivago, shedding light on the challenges faced by commercial AI solutions in this field [3].

Research on the use of chest X-ray images for tuberculosis diagnosis and localization has been reviewed [4]. In these studies, the value and effectiveness of chest X-rays as a primary screening tool for tuberculosis diagnosis have been addressed. Additionally, emphasis has been placed on how chest X-ray images can be utilized to determine the localization of TB lesions and monitor the progression of the disease.

It demonstrates the significant role that Convolutional Neural Networks (CNNs) can play in the accurate and automatic detection and classification of TB. The use of pre-trained CNNs highlights the potential applications for early and accurate diagnosis of TB [5]. This approach may enable healthcare professionals and medical systems to identify and manage TB cases more effectively, leading to faster treatment of patients and preventing the spread of the disease.

They have presented an innovative methodology for the temporal and spatial characterization of toxic substances known as BTEX. Utilizing receptor-oriented air circulation modeling and AI techniques, they have demonstrated the possibility of extracting valuable information from a single measurement point [6].

A method for predicting the impact of climate change on building cooling energy consumption using XAI has been developed. Through scenario-based approaches, meaningful and reliable projections have been provided to decision-makers, aiming to achieve climate-resilient and sustainable development goals [7].

The application of XAI in deep learning-based medical image analysis has been extensively explored. Emphasizing the importance of transparency, particularly in high-risk areas such as medical image analysis, their overview highlights the increasing demand in this field [8].

The use of machine learning techniques as a tool for tuberculosis (TB) diagnosis represents a significant advancement in the healthcare sector [9]. It suggests that machine learning algorithms could be utilized to provide additional assistance to healthcare professionals in TB diagnosis, thereby improving the treatment process by enabling faster and more accurate recognition of TB.

Automated machine learning models have also been successful in predicting TB [10]. Machine learning models trained on synthetic data have shown the ability to predict TB with high accuracy and sensitivity. This could play a crucial role in the early detection and treatment of the disease.

TB-Net is a proposed deep learning model for screening high-risk populations and early detection of TB using chest X-ray imaging [11]. This customized deep learning model could be integrated into widespread screening programs for TB and play a significant role in community-based healthcare services. TB-Net is considered to be a critical tool in ensuring early diagnosis and initiating treatment.

They have examined a new dataset using deep learning algorithms and visualized outputs with Grad-CAM, demonstrating the application of XAI in diagnosing paratuberculosis from histopathological images [12].

Three different XAI methods have been evaluated on CNN models designed for classifying lung cancer from histopathological images. These studies are considered a significant step towards transparency in black-box models [13].

A clinician-assisted intelligent workflow for retinal imaging has been proposed. This approach aims to enhance transparency in decisions related to systemic disease detection, thereby increasing reliability in clinical practice [14].

Tuberculosis detection in chest X-rays is an important method for recognizing the disease [15]. Machine learning and deep learning methods have been systematically addressed in this area. This study may facilitate the development of new and improved algorithms for accurately identifying TB in chest X-rays.

Efforts have been made to develop multi-scale Local Interpretable Model-Agnostic Explanations (LIME) for image classification. This work demonstrates the ability of XAI methods applied to CNN models to provide explanations through heatmaps at coarse to finer scales [16].

The utility of current neuroscience knowledge in designing biologically hierarchical and modular architecture (BHMA) models of the brain has been the focus. This perspective offers insights into the use of these models in spatial learning tasks [17].

Modern deep learning methods and XAI approaches have been employed to address skin cancer detection. These studies are evaluated as a significant step in improving diagnosis in medical image analysis and laying the groundwork for future developments [18].

## 3. Materials and Methods

### 3.1. Dataset

A collaborative team of researchers from Qatar University in Doha, Qatar, and Dhaka University in Bangladesh, in partnership with collaborators from Malaysia and medical experts from Hamad Medical Corporation and Bangladesh, has created a comprehensive chest X-ray database. This database encompasses a collection of images, including Tuberculosis (TB) positive cases as well as Normal images. In our latest release, 700 TB images are publicly available, while an additional 2800 TB images can be accessed through a straightforward negotiation process via the NIAID TB portal [19]. Additionally, the database contains 3500 images representing normal cases. Image samples from the dataset are provided, as seen in Figure 3.1.

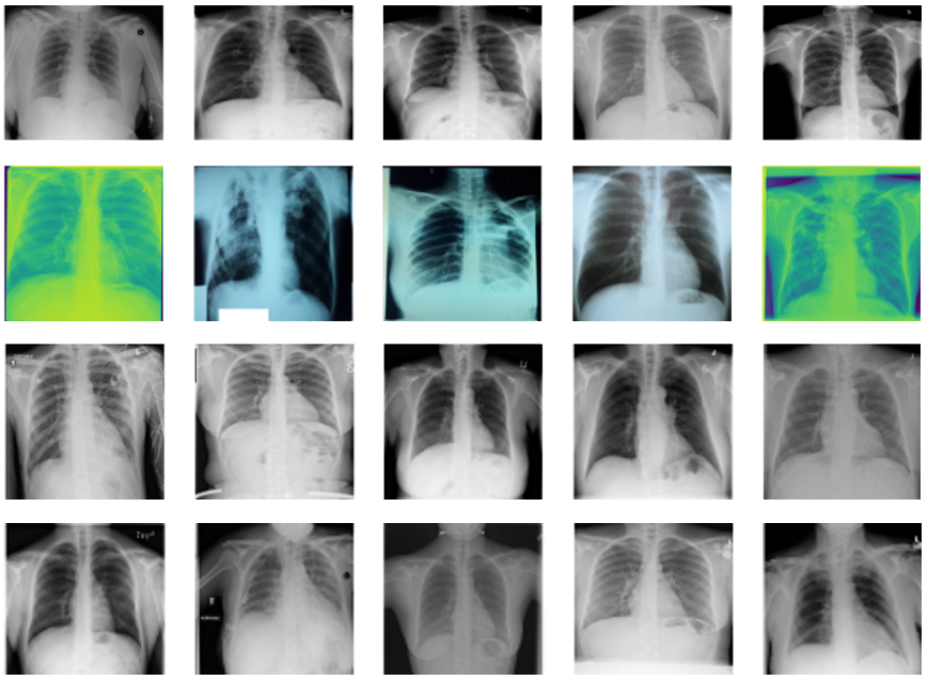

**Figure 3.1:** Tuberculosis (TB) Chest X-ray Database dataset examples

### 3.2. Convolutional Neural Network (CNN)

Convolutional Neural Networks (CNNs) play a critical role, especially in medical imaging applications. Despite their effectiveness in learning complex patterns from image data, understanding the internal decision-making processes of these networks is challenging [20]. Therefore, the internal decision-making processes of these networks are referred to as a ”black box” and criticized. For example, an illustration of a ”black box” example of this Convolutional Neural Network model is seen in Figure 3.2.
In the model used in our research, there are three Convolutional Layers (Conv2D). The sizes of these layers are 32, 64, and 128 respectively. These layers are used to extract feature maps of size (3x3) from input images of size (150x150) and to learn these features hierarchically. Following each convolutional layer, there is a MaxPooling Layer (MaxPooling2D). Max pooling is applied to reduce the size of feature maps and focus on important features. Subsequently, Fully Connected Layers (Dense) come into play. The Flatten layer flattens the feature maps extracted by the convolutional layers, making these features suitable for the utilization of fully connected layers. The location of these layers is referred to as a ”black box.” The output layer of the model includes a sigmoid activation function for the binary classification task, allowing the model to express the result as a probability between 0 and 1. For a better understanding of the model used in this study, it is modeled as seen in Figure 3.3.

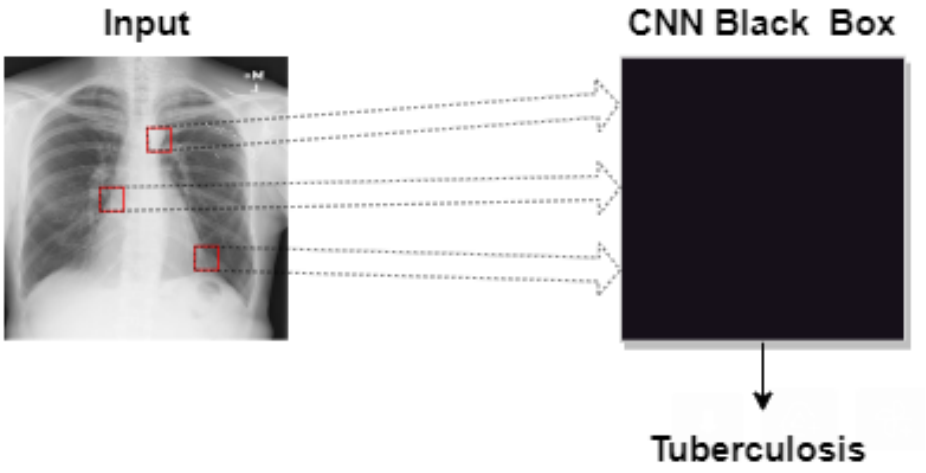


**Figure 3.2:** Example of the ”black box” model of Convolutional Neural Network

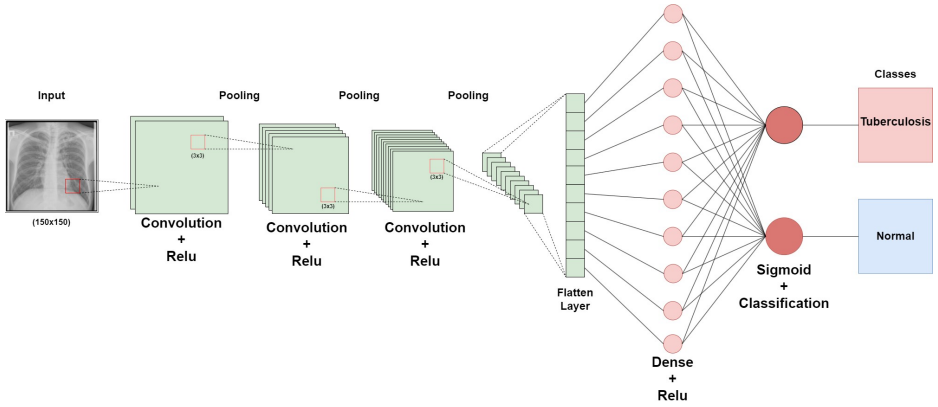


**Figure 3.3:** Used convolutional neural network (CNN) model

### 3.3. Explainable Artificial Intelligence (XAI)

Explainable Artificial Intelligence (XAI) is an effort aimed at elucidating the internal workings of complex artificial intelligence models, often referred to as black boxes. Understanding these models can be challenging due to their intricate structures and millions of parameters [21]. XAI has been developed to overcome this challenge and make the decisions of these models transparent and understandable for humans. Transparency contributes significantly to reliability and broader acceptance, particularly in industries like healthcare. The example illustrated in Figure 3.4 visually depicts the impact of Explainable Artificial Intelligence on a black box model.
While advanced deep learning models, particularly in fields like medical imaging, can be effective, uncertainties about how these models make decisions may undermine their reliability. XAI techniques, such as SHAP and LIME, are employed to reduce these uncertainties and elucidate the internal decision processes of black box models. In this context, techniques like SHAP and LIME provide effective tools to understand which features a model focuses on when making a specific prediction or diagnosis.

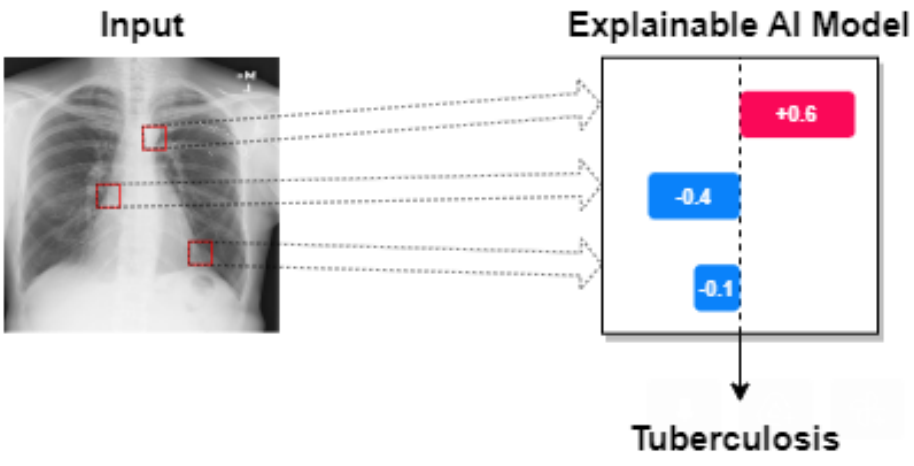


**Figure 3.4:** The impact of explainable AI on the black box

### 3.4. SHAP (SHapley Additive exPlanations)

Explainable Artificial Intelligence (XAI), particularly when using SHAP (SHapley Additive exPlanations), allows us to discern the contribution of each feature in chest X-ray data to the model's predictions. For example, in the case of Tuberculosis diagnosis, SHAP can explain pixel by pixel which features in X-ray images make the most significant contribution, either negatively or positively, to the model's decision [22]. Transparency in this decision-making process reinforces confidence in the capabilities of the artificial intelligence model.

$$\phi_i = \sum_{S \subseteq N\{i\}} \frac{|S|!(M-|S|-1)!}{M!}[f_x(S \cup i) - f_x(S)] \tag{3.1}$$

As seen in Equation 3.1, Shapley values are a method that fairly assesses the impact of a feature on the model output in the presence of other features. $\Delta\omega_i$ represents the Shapley value for feature $i$, and to compute this value, the sum of the contributions of the feature's impact on the model output across coalitions is calculated. The set $S$ represents the total number of variables affecting the model output, and $N$ denotes the number of levels of variables influencing the model output. $M$ specifies the number of variable selections for a particular feature. The calculation is performed over the entire set $S$, excluding the $i$ feature, with the condition $S \subseteq N \setminus \{i\}$. The contribution of each coalition is weighted based on the size of the $S$ set, and the result relies on the difference between the union of the variables influencing the model output $(S \cup \{i\})$ and the previous state with the $S$ set. These contributions are then summed with appropriate weights to obtain the Shapley value for feature $i$. These computations are used to fairly measure the contribution of a feature to the model prediction.

$$f_x(S) = E[f(x)|x_s] \tag{3.2}$$

As seen in Equation 3.2, $f_x$ represents the change in the output included by Shapley values for a specific feature. $x_S$ represents the set of observed conditions in the event of the occurrence, and $\mathbb{E}$ symbolizes the expectation operator. The formula is used to calculate the expected value of the model output under a specific feature set, expressing the concept of conditional expectation in probability theory.

$$g(z^{'}) = \phi_0 + \sum_{i=1}^{M} \phi_i Z_i^{'} = bias + \sum featureContribution \tag{3.3}$$

In Equation 3.3, $g(z')$ represents the output of a prediction, which is computed as the sum of a constant term $\phi_0$ (usually representing a bias value) and the contributions of each input feature $Z_i'$, typically expressed as weights $\phi_i$, multiplied and summed. This formulation is used to understand to what extent each input feature contributes to a prediction. The SHAP method utilizes Shapley values to determine these contributions, elucidating the net effect of an input feature on the prediction. This is a useful tool for understanding how predictions are generated by a model and determining which features are important, particularly in the analysis of complex models and large datasets.

Let's take an example from the Tuberculosis (TB) Chest X-ray Database to better understand how SHAP works. When applied to this example, SHAP generates explanations as seen in Figure 3.5 and Figure 3.6.

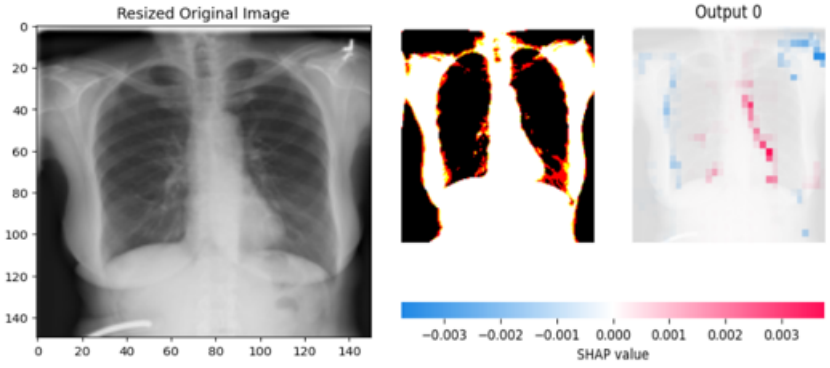


**Figure 3.5:** SHAP interpretation of the first randomly selected image from the dataset.

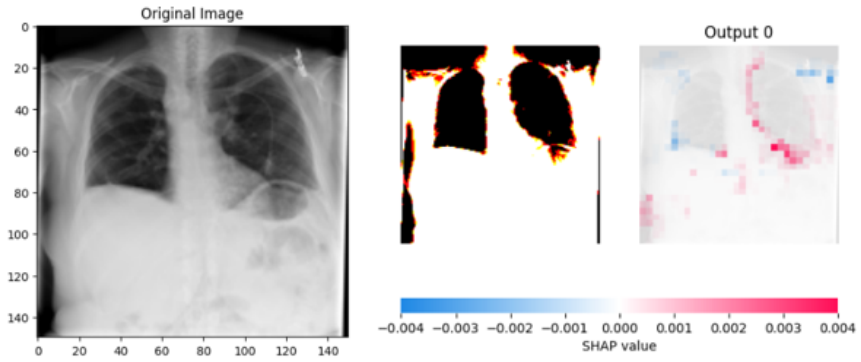


**Figure 3.6:** SHAP interpretation of the second randomly selected image from the dataset.

## 3.5. LIME (Local Interpretable Model-agnostic Explanations)

Local Interpretable Model-agnostic Explanations (LIME) is a technique specifically designed in the field of Explainable Artificial Intelligence (XAI) to make the decisions of complex artificial intelligence models, commonly referred to as "black boxes," more understandable. This method is adapted to locally explain the prediction decision of a model for a specific data point or instance.

$$\xi(x) = \underset{g \in G}{\operatorname{argmax}}\, \Im(f, g, \pi_x) + \Omega(g) \tag{3.4}$$

As seen in Equation 3.4, when $g$ is selected, it chooses the best explanation model within the set $G$ using the arg max operator. The selected model is determined by the part $I(f, g, \pi_x)$ that measures how well $g$ mimics $f$ in the $\pi_x$ region of $g$. The $I(f, g, \pi_x)$ function measures how successfully $G$ imitates $f$ in the region defined by $\pi_x$, and demonstrates the interpretability of the model's behavior around a specific input example. Additionally, the $\Omega(g)$ function measures the complexity of the selected explanation model and determines how simple or complex the explanation is.

To better understand how LIME works, the differences between the images taken from the Tuberculosis (TB) Chest X-ray Database and used in Figures 3.5 and 3.6 are highlighted by applying LIME. The generated explanations by LIME are depicted in Figures 3.7 and 3.8.

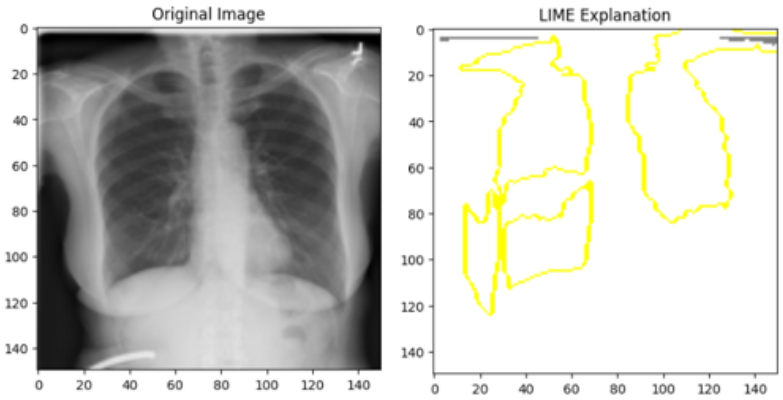


**Figure 3.7:** LIME output of the image taken in figure 3.5.

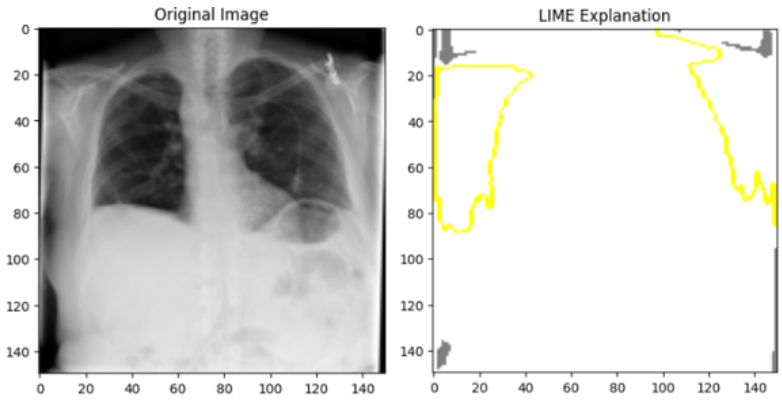


**Figure 3.8:** LIME output of the image taken in figure 3.6

### 3.6. Experimental study and results

In this study, the classified Tuberculosis (TB) Chest X-ray Database using a Convolutional Neural Network (CNN) model is used. The interpretability of the classification model is enhanced by integrating two explainable artificial intelligence techniques, namely SHAP and LIME. By comparing the results, it was observed that SHAP could better explain the classification of X-ray images related to Tuberculosis (TB) compared to LIME.
The training of the proposed convolutional neural network model and the interpretability of explainable artificial intelligence models were conducted. This process took place on a computer with the hardware specifications as seen in Table (3.1).

| **Class** | **Image Number** |
|---|---|
| Memory (RAM) | 16GB (2x8GB) DDR4 2933MHz |
| Processor | Intel i7-10750H-2,60GHz Turbo Boost 5,0GHz |
| Graphics Card, Memory | Nvidia GTX1650 Ti 4GB GDDR6 |

**Table 3.1:** Hardware specifications of the computer used in the paper.

A confusion matrix is used to evaluate the performance of a classification model. This matrix is created by comparing the predictions of a classification model on a set of test data for which the true values are known. It allows for a clear analysis of the model's successes, errors, and mispredictions. The confusion matrix of the model, along with the values TP (True Positive) 3494, TN (True Negative) 692, FP (False Positive) 6, FN (False Negative) 8, is presented in Figure 3.9. These values provide detailed insights into the reliability and accuracy of the classification model.

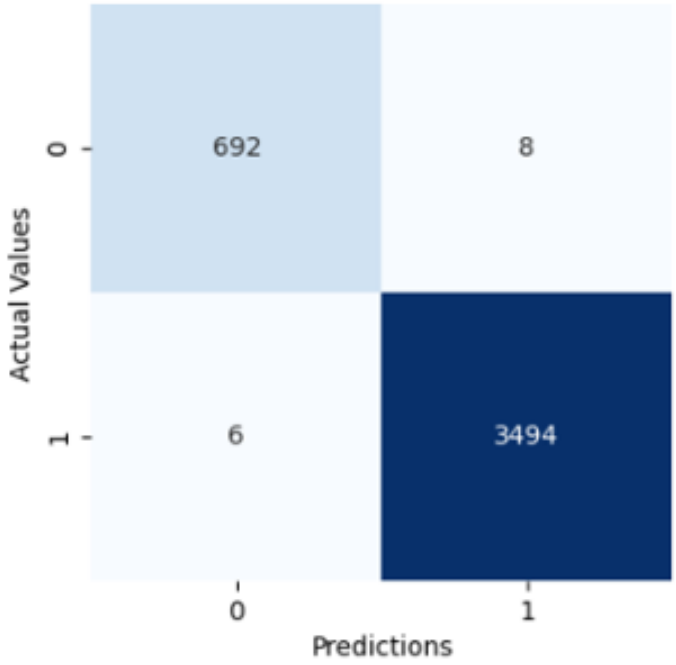


**Figure 3.9:** Convolutional neural networks confusion matrix outputs.

**TP (True Positive):** Instances where the model correctly predicts the positive class.
**TN (True Negative):** Instances where the model correctly predicts the negative class.
**FP (False Positive):** Instances where the model incorrectly predicts the positive class.
**FN (False Negative):** Instances where the model incorrectly predicts the negative class.
Performance metrics such as precision, recall, and accuracy are obtained from the confusion matrix values. Precision measures how many of the samples predicted as positive are actually positive. It expresses the ratio of true positives to the total positive predictions, as shown in Formula 3.5.

$$\text{Precision} = \frac{TP}{TP+FP} \tag{3.5}$$

Recall measures how many of the true positives are detected. It expresses the ratio of true positives to the total number of positive examples, as shown in Formula 3.6.

$$\text{Recall} = \frac{TP}{TP+FN} \tag{3.6}$$

Accuracy expresses the ratio of correctly predicted examples to the total number of examples. It is a metric that evaluates the overall model performance, as shown in Formula 3.7.

$$\text{Accuracy} = \frac{TP+TN}{TP+TN+FP+FN} \tag{3.7}$$

F1-score balances precision and recall. This metric tends to minimize both false positives and false negatives, especially in balanced classification problems. Formula 3.8 illustrates the F1-score.

$$F1 = 2 \times \frac{\text{Precision} \times \text{Recall}}{\text{Precision} + \text{Recall}} \tag{3.8}$$

The evaluation metrics for the Convolutional Neural Network (CNN) model used in the study, including F1 score, precision, recall, and support, are provided in Table 3.2.

| | precision | recall | f1-score | support |
|---|---|---|---|---|
| NORMAL | 0.91 | 0.87 | 0.89 | 234 |
| TUBERCULOSIS | 0.93 | 0.95 | 0.94 | 390 |

**Table 3.2:** Classification report

**An example of artificial intelligence explainable to the TP example of the confusion matrix:**

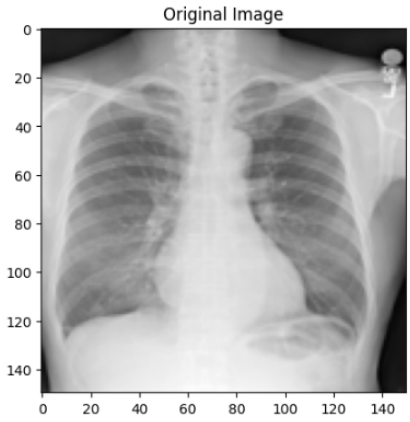


**Figure 3.10:** Original image

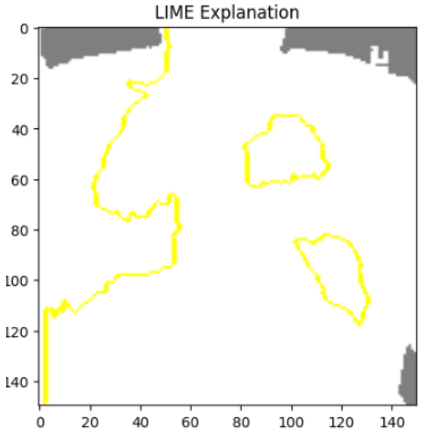


**Figure 3.11:** LIME output

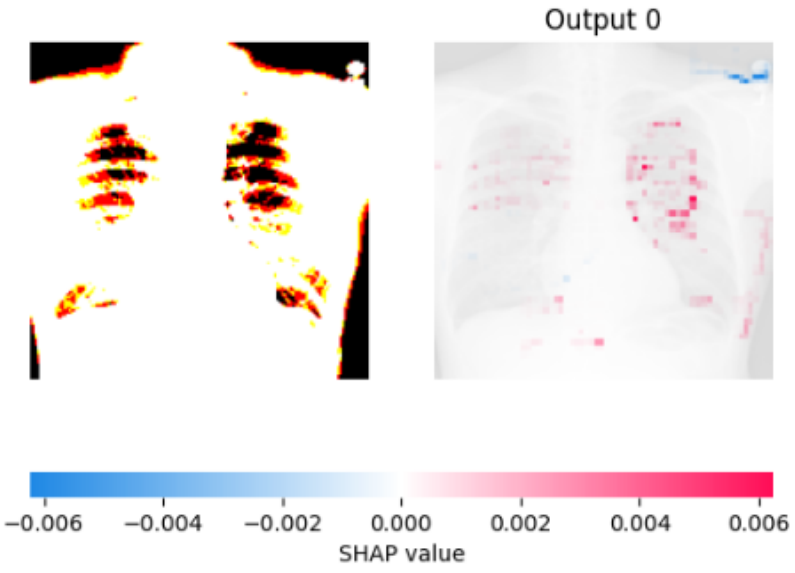


**Figure 3.12:** SHAP output

The confusion matrix derived from the results of our CNN model applied to the Tuberculosis (TB) Chest X-ray Database is specifically illustrated with a randomly selected example of Tuberculosis-free (TP) instances in Figure 3.10. The results obtained by applying two

interpretable artificial intelligence models, SHAP and LIME, to this example are presented in Figures 3.11 and 3.12, respectively. As observed in Figure 3.11, the SHAP model comprehensively explains the areas where Tuberculosis disease may exist in both negative and positive directions, providing more detailed information about whether the individual has Tuberculosis. In Figure 3.12, the LIME model outlines the regions where Tuberculosis disease could be present. Upon examining these results, it is observed that, compared to LIME, SHAP provides better results in explaining Tuberculosis disease.

**An example of artificial intelligence explainable to the FP example of the confusion matrix:**

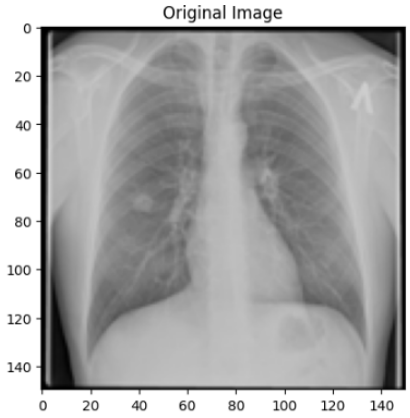


**Figure 3.13:** Original image

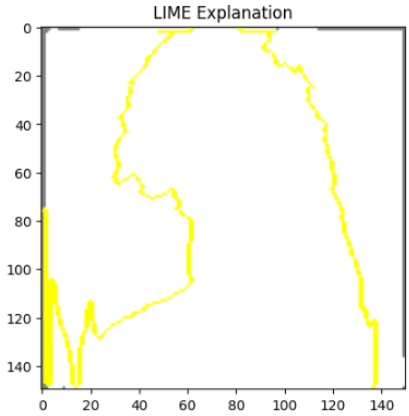


**Figure 3.14:** LIME output

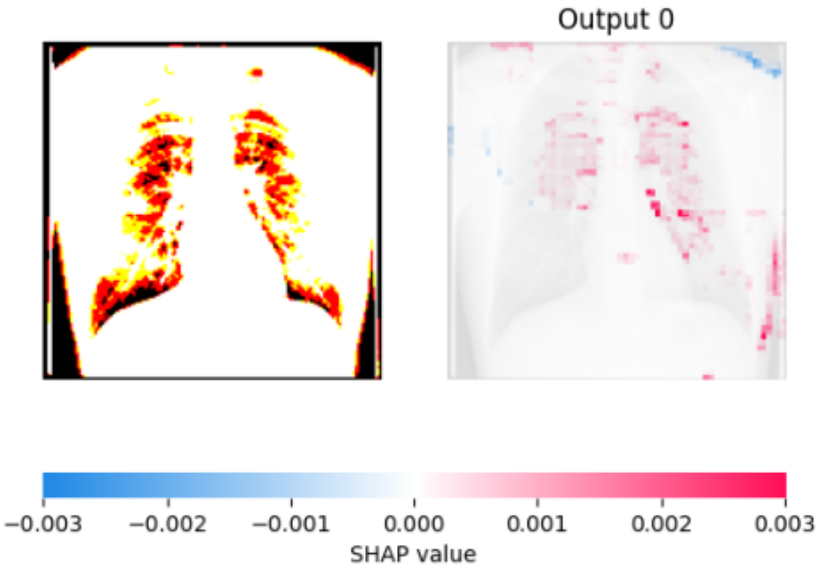


**Figure 3.15:** SHAP output

The confusion matrix derived from the results of our CNN model applied to the Tuberculosis (TB) Chest X-ray Database specifically showcases a randomly selected example of instances with Tuberculosis disease (FP) in Figure 3.13. The results obtained by applying explainable artificial intelligence models, SHAP and LIME, to this example are presented in Figures 3.14 and 3.15, respectively. As seen in Figure 3.15, the applied SHAP model elaborately explains the areas where Tuberculosis disease may be present in the positive direction, providing more detailed information about the likelihood of the individual having Tuberculosis. In Figure 3.14, the applied LIME model outlines the boundaries where Tuberculosis disease could exist. Upon examining these results, it is observed that SHAP performs better in explaining Tuberculosis disease compared to LIME.

**An example of artificial intelligence explainable to the FN example of the confusion matrix:**

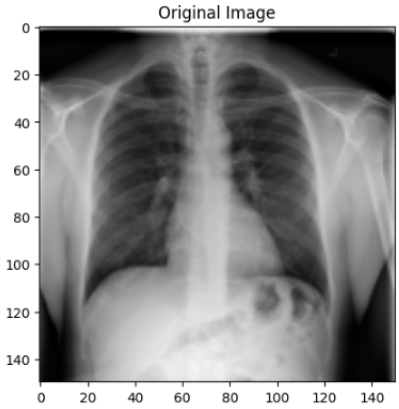


**Figure 3.16:** Original image

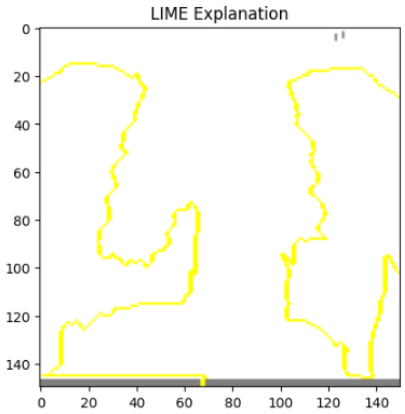


**Figure 3.17:** LIME output

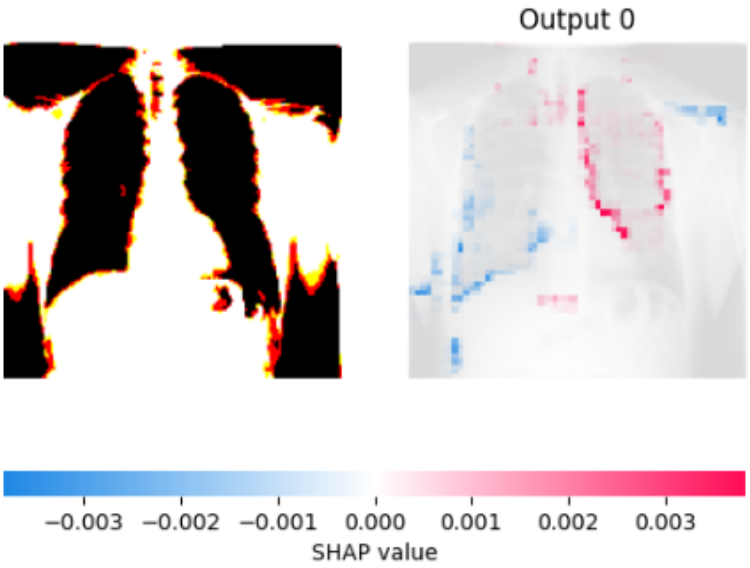


**Figure 3.18:** SHAP output

An image representing a case of Tuberculosis (TB) with false predictions of the absence of the disease, randomly selected from FN instances in the confusion matrix of our applied CNN model on the Tuberculosis Chest X-ray Database, is presented in Figure 3.16. Results obtained by applying explainable artificial intelligence models, SHAP and LIME, to this example are shown in Figures 3.17 and 3.18, respectively. As seen in Figure 3.18, the applied SHAP model elaborately explains the areas where Tuberculosis disease may be present in both negative and positive directions, providing more detailed information about the individual's likelihood of not having Tuberculosis. In Figure 3.17, the applied LIME model outlines the boundaries where Tuberculosis disease could exist, as shown in Figure 3.16. Upon examining these results, it is observed that SHAP performs better in explaining the absence of Tuberculosis compared to LIME.

**An example of artificial intelligence explainable to the TN example of the confusion matrix:**

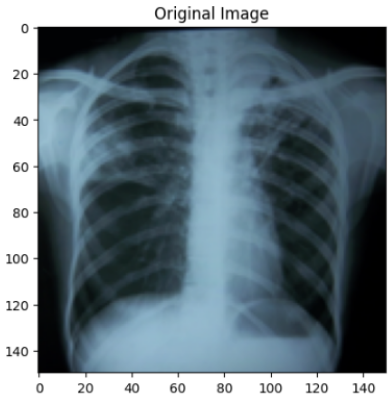


**Figure 3.19:** Original image

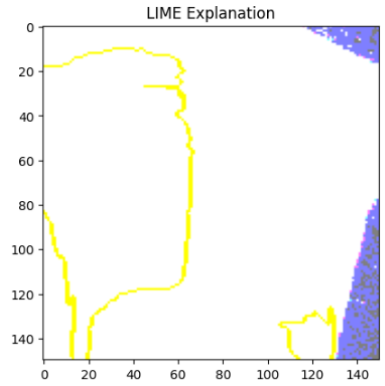


**Figure 3.20:** LIME output

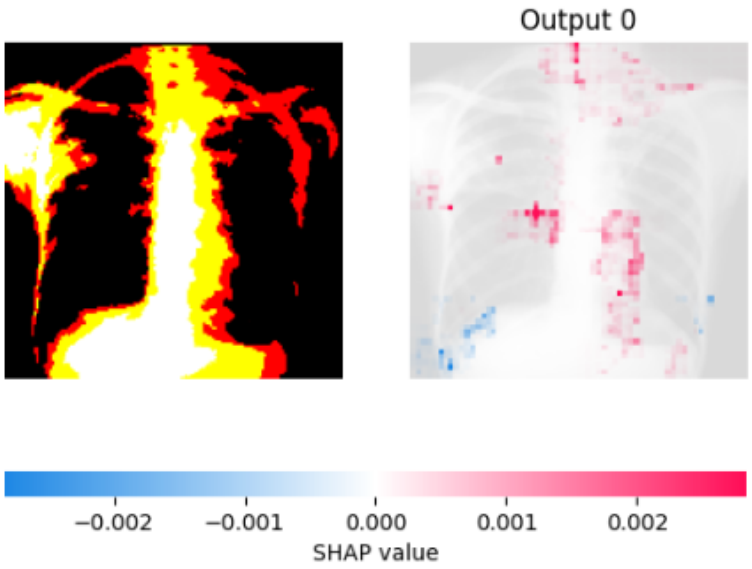


**Figure 3.21:** SHAP output

An image illustrating a case randomly selected from the TN instances of the confusion matrix of our CNN model applied to the Tuberculosis (TB) Chest X-ray Database, where the disease is not present but a wrong prediction of the individual being diseased has been made, is provided in Figure 3.19. Results obtained by applying explainable artificial intelligence models, SHAP and LIME, to this example are presented in Figures 3.20 and 3.21, respectively. As seen in Figure 3.21, the applied SHAP model elaborately explains the areas where Tuberculosis disease may be present in both negative and positive directions, providing more detailed information about the absence of Tuberculosis in the individual. In Figure 3.20, the applied LIME model outlines the boundaries where Tuberculosis disease could exist, as shown in Figure 3.19. Upon examining these results, it is observed that SHAP performs better in explaining the absence of Tuberculosis compared to LIME.

## 4. Conclusions

In this study, artificial intelligence (AI) applications in the diagnosis of tuberculosis (TB) were examined in depth. Specifically, the focus was on developing a Convolutional Neural Network (CNN) model for the classification of TB chest X-ray images. Explainable artificial intelligence (XAI) techniques such as SHAP (SHapley Additive exPlanations) and LIME (Local Interpretable Model-agnostic Explanations) were integrated to make the decision-making processes of this model more understandable.

Such mathematical model-based techniques contribute to making models used in medical imaging applications more transparent, understandable, and trustworthy.

The research addressed a significant issue faced by AI applications in the healthcare domain: lack of transparency and reliability. Through the use of XAI techniques, it was demonstrated that the decisions of AI models can be made more understandable. This increases trust in AI-supported diagnostic systems in clinical settings and enables healthcare professionals to make more informed decisions.

In particular, through the comparison of XAI techniques such as SHAP and LIME, SHAP was found to be more effective in TB diagnosis. SHAP provided more reliable and detailed information on the presence or absence of TB disease by offering detailed explanations in the

classification of X-ray images.

Future research should focus on further development and integration of XAI techniques for medical imaging applications. This can enhance the reliability of AI models and enable their more effective use in clinical applications. Additionally, conducting in-depth analyses with larger datasets and using different XAI techniques is critical for improving the performance of AI models.

The results of this study demonstrate that enhancing the reliability and effectiveness of AI-based diagnostic methods in medical imaging can positively contribute to patient treatment and recovery processes. Therefore, future research should focus on broader and more effective use of XAI techniques and making AI models more reliable.

## Article Information

**Author's contributions:** or The article has a single author. The author has read and approved the final manuscript.

**Conflict of Interest Disclosure:** The author declare that he has no known competing financial interests or personal relationships that could have appeared to influence the work reported in this paper.



**Supporting/Supporting Organizations:** The author gratefully acknowledge the financial support of Sakarya University of Applied Sciences AI And Data Science Research And Application Center.

**Ethical Approval and Participant Consent:** This research adheres to ethical principles and guidelines in conducting the comparative analysis of Explainable Artificial Intelligence (XAI) techniques, specifically SHAP (SHapley Additive exPlanations) and LIME , on tuberculosis x-ray dataset.

**Plagiarism Statement:** This article was scanned by the plagiarism program. No plagiarism detected.

**Availability of data and materials:** tawsifurrahman/tuberculosis-tb-chest-xray-dataset".

## References

[1] C. Liu, Y. Cao, M. Alcantara, B. Liu, M. Brunette, J. Peinado, *W. Curioso, TX-CNN: Detecting tuberculosis in chest x-ray images using convolutional neural network*, IEEE Int. Conf. Image Process. (ICIP), 2017.
[2] U.K. Lopes, J.F. Valiati, *Pre-trained convolutional neural networks as seature extractors for tuberculosis detection*, Comput. Biol. Med., 2017.
[3] S. Mahamood, Explainable artificial intelligence and its potential within industry, in Proc. 1st Workshop Interactive Nat. Lang. Technol. Explainable Artif. Intell. (NL4XAI), J.M. Alonso, A. Catala (Eds.), Association for Computational Linguistics, 2019.
[4] R. Guo, K. Passi, C.K. Jain, *Tuberculosis diagnostics and localization in chest x-rays via deep learning models*, Front. Artif. Intell., **3** (2020), 583427.
[5] B. Oltu, S. Güney, B. Dengiz, M. Ağıldere, *Automated tuberculosis detection using pre-trained CNN and SVM*, 44th Int. Conf. Telecommun. Signal Process. (TSP), 2021.
[6] S. Stanišić, M. Perišić, G. Jovanović, D. Maletić, D. Vudragović, A. Vranić, A. Stojić, *What Information on Volatile Organic Compounds Can Be Obtained from the Data of a Single Measurement Site Through the Use of Artificial Intelligence?*, Artificial Intelligence: Theory Appl., E. Pap (Ed.), Springer International Publishing, 2021.
[7] D. Chakraborty, A. Alam, S. Chaudhuri, H. Başağaoğlu, T. Sulbaran, S. Langar, *Scenario-based prediction of climate change impacts on building cooling energy consumption with explainable artificial intelligence*, Appl. Energy, **291** (2021), 116807.
[8] B.H.M. van der Velden, H.J. Kuijf, K.G.A. Gilhuijs, M.A. Viergever, *Explainable artificial intelligence (XAI) in deep learning-based medical image analysis*, Med. Image Anal., **79** (2022), 102470.
[9] A.D. Orjuela-Cañón, A.L. Jutinico, C. Awad, E. Vergara, A. Palencia, *Machine learning in the loop for tuberculosis diagnosis support*, Front. Public Health, **10** (2022, 876949.
[10] H.H. Rashidi, I.H. Khan, L.T. Dang, S. Albahra, U. Ratan, N. Chadderwala, W. To, P. Srinivas, J. Wajda, N.K. Tran, *Prediction of tuberculosis using an automated machine learning platform for models trained on synthetic data*, J. Pathol. Inform., **13** (2022), 100172.
[11] A. Wong, J.R.H. Lee, H. Rahmat-Khah, A. Sabri, A. Alaref, H. Liu, *TB-Net: A tailored, self-attention deep convolutional neural network design for detection of tuberculosis cases from chest x-ray images*, Front. Artif. Intell., **5** (2022), 827299.
[12] T. Yiğit, N. Şengöz, Ö. Özmen, J. Hemanth, A.H. Işık, *Diagnosis of paratuberculosis in histopathological images based on explainable artificial intelligence and deep learning*, Traitement du Signal, **39**(3), 2022, 863-869.
[13] J. Purohit, I. Shivhare, V. Jogani, S. Attari, S. Surtkar, *Adversarial Attacks and Defences for Skin Cancer Classification*, *2023 Int. Conf. Adv. Technol. (ICONAT)*, IEEE, Jan. 2023.
[14] A.R. Bhatt, R. Vaghashiya, M. Kulkarni, P. Kamaraj, *Explainable artificial intelligence in retinal imaging for the detection of systemic diseases*, 2022.
[15] S. Hansun, A. Argha, S.-T. Liaw, B.G. Celler, G.B. Marks, *Machine and deep learning for tuberculosis detection on chest x-rays: systematic literature review*, J. Med. Internet Res., **23** (2023), e43154.
[16] H. Hajiyan, M. Ebrahimi, *Multi-scale local explanation approach for image analysis using model-agnostic explainable artificial intelligence (XAI)*, in Med. Imaging 2023: Digital Comput. Pathol., J.E. Tomaszewski, A.D. Ward (Eds.), SPIE, 2023.
[17] N.E. Jaimes, C. Zeng, R. Simha, *Using biologically hierarchical modular architecture for explainable, tunable, generalizable, spatial AI*, in Disruptive Technol. Inf. Sci. VII, M. Blowers, J. Holt, B.T. Wysocki (Eds.), 2023.
[18] F. Mahmud, M.M. Mahfiz, M.Z.I. Kabir, Y. Abdullah, An Interpretable deep learning approach for skin cancer categorization, 2023.
[19] NIAID TB portal program dataset [Online]. Available: https://tbportals.niaid.nih.gov/download-data.
[20] M.M. Hasan, M.M. Hossain, M.M. Rahman, A.K. Azad, S.A. Alyami, M.A. Moni, *FP-CNN: Fuzzy pooling-based convolutional neural network for lung ultrasound image classification with explainable AI*, Comput. Biol. Med., **165** (2023), 107407.
[21] E. Shoemaker, H. Malik, H. Narman, J. Chaudri, *Explaining the unseen: Leveraging XAI to enhance the trustworthiness of black-box models in performance testing*, Proc. Comput. Sci., **224** (2023), 83-90.
[22] R. Younisse, A. Ahmad, Q. Abu Al-Haija, *Explaining intrusion detection-based convolutional neural networks using Shapley additive explanations (SHAP)*, Big Data Cogn. Comput., **6**(4) (2022), 126.

*Journal of Mathematical Sciences and Modelling*, 7(1) (2024) 45-50
*Research Article*

**Journal of Mathematical Sciences and Modelling**

*Journal Homepage: www.dergipark.gov.tr/jmsm*
*ISSN 2636-8692*
*DOI: http://dx.doi.org/10.33187/jmsm.1466687*

# Higher Dimensional Leibniz-Rinehart Algebras

**Mahmut Koçak**[1] **and Selim Çetin**[2*]

[1]*Department of Mathematics and Computer Science, Faculty of Sciences, Eskişehir Osmangazi Üniversitesi, Eskişehir, Türkiye*
[2]*Department of Mathematics, Faculty of Sciences & Humanities, Burdur Mehmet Akif Ersoy Üniversitesi, Burdur, Türkiye*
[*]*Corresponding author*

**Article Info**

***Keywords:*** *Crossed module, Leibniz algebra, Leibniz algebroid, Leibniz-Rinehart algebra, Lie-Rineart algebra*
***2010 AMS:*** *18G45, 17A32, 16W25*
***Received:*** *8 April 2024*
***Accepted:*** *8 May 2024*
***Available online:*** *8 May 2024*

**Abstract**

In this article, we delve into the realm of higher dimensional Leibniz-Rinehart algebras, exploring the intricate structures of Leibniz algebroids and their applications. By generalizing the concept of Lie algebroids and incorporating a Leibniz rule for the anchor map, the study sheds light on the fundamental principles underlying connections and underscores their significance. Through a comprehensive analysis of Leibniz-Rinehart algebras, this study paves the way for advancements and applications, offering a deeper understanding of the intricate relationship between algebraic and geometric structures.

## 1. Introduction

A Leibniz algebroid is a mathematical structure that generalizes the concept of a Lie algebroid by incorporating a Leibniz rule for the anchor map. Regarding the Lie bracket on algebroid sections, the anchor map in a Leibniz algebroid satisfies a Leibniz rule. This indicates that the Leibniz product of sections which joins the Lie bracket and the anchor map, is preserved by the anchor map. In generalized geometry, Leibniz algebroids are essential because they offer a framework for investigating connections, torsion, and curvature in a more expansive context. Leibniz algebroids form a basic subject of research in contemporary geometric and algebraic structures because of their applicability in many branches of mathematics and physics, such as string theory, mathematical physics, and differential geometry.

Leibniz algebroids generalize the concept of Lie algebroids by incorporating a Leibniz rule for the anchor map. This generalization allows for a broader class of structures to be studied, providing a more flexible framework for geometric and algebraic investigations.

Leibniz algebroids play a crucial role in the study of connections, torsion, and curvature in a generalized setting. By introducing appropriate structures on Leibniz algebroids, one can analyze geometric properties and derive meaningful results related to curvature and other geometric quantities. The study of Leibniz algebroids has applications in various areas of mathematics and theoretical physics. They are used in differential geometry, mathematical physics, and string theory to describe geometric structures and symmetries, making them essential tools for understanding fundamental principles in these fields. Leibniz algebroids provide a bridge between algebraic structures, such as Lie algebras, and geometric objects, such as vector bundles and tangent bundles. This connection allows for a deeper understanding of the interplay between algebraic and geometric concepts, leading to new insights and discoveries. Their study leads to advanced research topics in modern mathematics, including generalized geometry, Poisson geometry, and higher structures. Researchers use Leibniz algebroids to explore cutting-edge ideas and develop new theories that push the boundaries of mathematical knowledge.

The algebraization of Leibniz algebroids, known as Leibniz-Rinehart algebras, are mathematical structures that generalize the relationship between the Leibniz algebra of smooth vector fields on a manifold and the algebra of smooth functions. They are composed of a commutative algebra and a Leibniz algebra with extra structure. This concept provides a categorical framework for addressing problems related to left (right) Kähler quantization and reduction. Leibniz-Rinehart algebras play a crucial role in capturing infinitesimal symmetries and have applications in various mathematical areas, offering a deeper understanding of the relationship between algebraic and geometric structures. The study of Lebniz-Rinehart algebras opens up avenues for exploring connections between classical and quantum theories, paving the way for advancements in mathematical research and applications.

***Email addresses and ORCID numbers*: mkocak@ogu.edu.tr, 0000-0001-7774-0144 (M. Koçak), seliimcetin@gmail.com, 0000-0002-9017-1465 (S. Çetin),**
**Cite as "Mahmut Koçak, Selim Çetin, *Higher dimensional Leibniz-Rinehart algebras*, J. Math. Sci. Model., 7(1) (2024), 45-50"**

## 2. Leibniz-Rinehart Algebras

Leibniz-Rinehart algebras are algebraic structures that combine the properties of Leibniz algebras and modules over a commutative ring. Specifically, a Leibniz-Rinehart algebra over a commutative algebra $C$ consists of a Leibniz algebra $\mathfrak{g}$ together with a $C$-module structure on $\mathfrak{g}$ and a map $\rho$ from $\mathfrak{g}$ to derivations of $C$ that respects both the Leibniz algebra bracket and the module action. Leibniz-Rinehart algebras generalize Leibniz algebras by incorporating module structures, allowing for a richer interplay between algebraic and geometric properties. They play a significant role in various mathematical areas, offering a framework for studying differential operators, deformations, and geometric structures with algebraic underpinnings.
We indicate that for the rest of the paper, $\mathbb{K}$ is fixed as the ground field and $C$ is fixed as a commutative algebra over $\mathbb{K}$. Here, $\mathrm{Der}(C)$ is the set of all $\mathbb{K}$-derivations over the set $C$, given by

$$Der(C) = \{D : C \longrightarrow C | D(cc') = cD(c') + D(c)c'\},$$

where it forms the set of all $\mathbb{K}-$linear transformations.

**Definition 2.1.** *[1] A Leibniz algebra $\mathfrak{g}$ over $\mathbb{K}$ is a $\mathbb{K}$-vector space equipped with a $\mathbb{K}$-bilinear map $[-,-] : \mathfrak{g} \times \mathfrak{g} \longrightarrow \mathfrak{g}$ satisfying the Leibniz identity*

$$\left[\varsigma, [\varsigma', \varsigma'']\right] = \left[\left[\varsigma, \varsigma'\right], \varsigma''\right] + \left[\varsigma', \left[\varsigma, \varsigma''\right]\right],$$

*for all $\varsigma, \varsigma', \varsigma'' \in \mathfrak{g}$.*

**Definition 2.2.** *[1] Let $\mathfrak{g}$ be a Leibniz algebra and $\varphi := (d, D)$ be a pair of $\mathbb{K}$-linear maps $d, D : \mathfrak{g} \longrightarrow \mathfrak{g}$ such that*

$$\begin{array}{rcl} D[\varsigma, \varsigma'] & = & [D(\varsigma), \varsigma'] - [D(\varsigma'), \varsigma], \\ d[\varsigma, \varsigma'] & = & [d(\varsigma), \varsigma'] + [\varsigma, d(\varsigma')], \\ [\varsigma, d(\varsigma')] & = & [\varsigma, D(\varsigma')], \end{array}$$

*for all $\varsigma, \varsigma' \in \mathfrak{g}$. The pair $\varphi = (d, D)$ is called a biderivation of $\mathfrak{g}$.*

The set of all biderivations of $\mathfrak{g}$ is denoted by $Bider(\mathfrak{g})$. Following [1], $Bider(\mathfrak{g})$ is endowed with a Leibniz algebra structure with respect to the bracket $[\varphi, \varphi']$ where

$$\left[\varphi, \varphi'\right] = (dd' - d'd, Dd' - d'D),$$

for all $\varphi = (d, D), \varphi' = (d', D') \in Bider(\mathfrak{g})$ .

**Definition 2.3.** *[2] Let $\mathfrak{g}, \mathfrak{g}'$ be Leibniz algebras. An action of $\mathfrak{g}$ on $\mathfrak{g}'$ is a pair of $\mathbb{K}$-bilinear maps,*

$$\mathfrak{g} \otimes \mathfrak{g}' \longrightarrow \mathfrak{g}', \ \left(\varsigma, \varsigma'\right) \longmapsto \left[\varsigma, \varsigma'\right], \ \mathfrak{g}' \otimes \mathfrak{g} \longrightarrow \mathfrak{g}', \ \left(\varsigma', \varsigma\right) \longmapsto \left[\varsigma', \varsigma\right],$$

*such that*

$$\begin{array}{rcl} [\varsigma, [\varepsilon, \varepsilon']] & = & [[\varsigma, \varepsilon], \varepsilon'] + [\varepsilon, [\varsigma, \varepsilon']], \\ [\varsigma, [\varepsilon', \varepsilon]] & = & [[\varsigma, \varepsilon'], \varepsilon] + [\varepsilon', [\varsigma, \varepsilon]], \\ [\varepsilon', [\varsigma, \varepsilon]] & = & [[\varepsilon', \varsigma], \varepsilon] + [\varsigma, [\varepsilon', \varepsilon]], \\ [\varsigma, [\varsigma', \varepsilon']] & = & [[\varsigma, \varsigma'], \varepsilon'] + [\varsigma', [\varsigma, \varepsilon']], \\ [\varsigma', [\varsigma, \varepsilon']] & = & [[\varsigma', \varsigma], \varepsilon'] + [\varsigma, [\varsigma', \varepsilon']], \\ [\varsigma', [\varepsilon', \varsigma]] & = & [[\varsigma', \varepsilon'], \varsigma] + [\varepsilon', [\varsigma', \varsigma]], \end{array}$$

*for all $\varsigma, \varepsilon \in \mathfrak{g}$ , $\varsigma', \varepsilon' \in \mathfrak{g}'$.*

**Definition 2.4.** *[3] A Leibniz-Rinehart algebra over $(\mathbb{K}, C)$ is a Leibniz $\mathbb{K}$-algebra $\mathfrak{g}$ together with a structure of $C$-module on $\mathfrak{g}$ and the map, called anchor map, $\rho : \mathfrak{g} \longrightarrow \mathrm{Der}(C)$ which are simultaneously Leibniz algebra and $C$-module homomorphisms such that*

$$\left[\varsigma, c\varsigma'\right] = c[\varsigma, \varsigma'] + \rho\left(\varsigma\right)(c)\,\varsigma',$$

$$\rho\left[\left|\varsigma, \varsigma'\right|\right] = \left[\rho\left(\varsigma\right), \rho\left(\varsigma'\right)\right],$$

*for all $c \in C$, $\varsigma$, $\varsigma' \in \mathfrak{g}$.*

Let $(\mathfrak{g}, \rho), (\mathfrak{g}', \rho')$ be Leibniz-Rinehart algebras. A Leibniz-Rinehart algebra homomorphism $f : (\mathfrak{g}, \rho) \longrightarrow (\mathfrak{g}', \rho')$ consists of a simultaneously Leibniz $\mathbb{K}$-algebra and $C$-module homomorphism $f : \mathfrak{g} \longrightarrow \mathfrak{g}'$ such that $\rho' \circ f = \rho$. Consequently, we have the category of Leibniz-Rinehart algebras over $(\mathbb{K}, C)$ which will be denoted here by $\mathfrak{Lb}\mathfrak{R}(C)$.

**Example 2.5.**

1. *If $\rho = 0$, then a Leibniz-Rinehart algebra $\mathfrak{g}$ is a Leibniz $C$-algebra.*
2. *If $C = \mathbb{K}$, then $Der(C) = 0$, and a Leibniz-Rinehart algebra $\mathfrak{g}$ is a Leibniz algebra.*
3. *Every Lie-Rinehart algebra [4]-[9] is a Leibniz-Rinehart algebra, in fact there is an inclusion functor $inc : \mathfrak{LR}(C) \hookrightarrow \mathfrak{Lb}\mathfrak{R}(C)$ from the category of Lie-Rinehart algebras, which is left adjoint to the Liezation functor that assigns to a Leibniz-Rinehart algebra $(\mathfrak{g}, \rho)$ the Lie-Rinehart algebra $\mathfrak{g}_{\mathrm{Lie}} = \mathfrak{g}/\mathfrak{g}^{\mathrm{ann}}$, where $\mathfrak{g}^{\mathrm{ann}} = \langle\{[\varsigma, \varsigma] : \varsigma \in \mathfrak{g}\}\rangle$, and anchor map $\widetilde{\rho} : \mathfrak{g}_{\mathrm{Lie}} \longrightarrow \mathrm{Der}(C)$ induced from $\rho$.*

4. *A right NP-algebra over a ring $\mathbb{K}$ is an algebra $P$ which is an associative and Leibniz algebra and satisfies the right Poisson identity*

$$[p', p\cdot p''] = p\cdot[p', p''] + [p', p]\cdot p'',$$

*for all $p, p', p'' \in P$. (The notion introduced in [10] as a noncommutative analogue of classical Poisson algebras). Let $P$ be commutative. Define $\rho : P \longrightarrow Der(P)$, by $p \longmapsto [p, \_]$, for all $p \in P$. Then we have*

$$\begin{aligned}[p', p\cdot p''] = &\quad p\cdot[p', p''] + [p', p]\cdot p'' \\ = &\quad p\cdot[p', p''] + \rho(p')(p)\,p'',\end{aligned}$$

*which makes $(P, \rho)$ a Leibniz-Rinehart algebra.*

*Poisson algebras are of significant importance in mathematics and theoretical physics for several reasons, Poisson algebras are closely related to symplectic geometry, where they provide a framework for studying classical mechanical systems. The Poisson bracket structure on a Poisson algebra captures the essential properties of symplectic manifolds, allowing for the formulation of Hamiltonian dynamics and symplectic geometry in a purely algebraic setting. Moreover, Poisson algebras play a crucial role in the process of quantization, which is the mathematical procedure of transitioning from classical mechanics to quantum mechanics. By understanding the Poisson bracket structure of a system, one can derive quantum operators that correspond to classical observables, leading to a deeper understanding of quantum systems. And, in geometric quantization, Poisson algebras provide a bridge between classical and quantum mechanics by quantizing symplectic manifolds. This process involves associating a Hilbert space to the space of functions on a symplectic manifold, with the Poisson bracket structure guiding the quantization procedure. In addition to the study of Poisson algebras also involves investigating Poisson cohomology, which captures the algebraic structure of Poisson brackets. Poisson cohomology provides insights into the underlying geometry of Poisson manifolds and plays a role in understanding the deformation theory of Poisson structures.Therefore, the following example is significant.*

5. *[3] A Leibniz algebroid over a vector bundle $E$ over a base manifold $M$ is an anchor $\rho : E \longrightarrow M$ together with an $\mathbb{R}$-bilinear Leibniz bracket on the $C^\infty(M)$-module $Sec(E)$ of smooth sections of $E$, which satisfy*

$$[\varsigma, f\varsigma'] = f[\varsigma, \varsigma'] + \rho(\varsigma)(f)\varsigma',$$

*for all $f \in C^\infty(M)$, $\varsigma, \varsigma' \in Sec(E)$ .*

6. *Let $(\mathfrak{g}, \rho)$ be a Leibniz-Rinehart algebra. Then $C \rtimes \mathfrak{g}$ is a Leibniz-Rinehart algebra with the bracket*

$$\left[(c, \varsigma), (c', \varsigma')\right] = \left(\rho(\varsigma)(c') - \rho(\varsigma')(c), [\varsigma, \varsigma']\right)$$

*and*

$$\widetilde{\rho}(c, \varsigma) = \rho(\varsigma),$$

*for all $(c, \varsigma), (c', \varsigma') \in C \rtimes \mathfrak{g}$.*

7. *Let $T : Der(C) \longrightarrow Der(C)$ , be a $\mathbb{K}$-linear and a $C$-module homomorphism such that*

$$T(D_1)T(D_2) = T(T(D_1)D_2) = T(D_1, T(D_2)),$$

*for all $D_1$, $D_2 \in Der(C)$. Then $Der(C)$ is a Leibniz $\mathbb{K}$-algebra with the bracket*

$$\begin{aligned}[,] : Der(C)\times Der(C) &\longrightarrow Der(C) \\ (D_1, D_2) &\longmapsto [\![D_1, D_2]\!] = T(D_1)D_2 - D_2T(D_1),\end{aligned}$$

*which satisfies*

$$[\![D_1, cD_2]\!] = c[\![D_1, D_2]\!] + T(D_1)(c)D_2,$$

*for all $c \in C$, $D_1$, $D_2 \in Der(C)$ . On the other hand, we have*

$$\begin{aligned}T[\![D_1, D_2]\!] &= T(T(D_1)D_2 - D_2T(D_1)) \\ &= T(T(D_1)D_2) - T(D_2T(D_1)) \\ &= T(D_1)T(D_2) - T(D_2)T(D_1) \\ &= [T(D_1), T(D_2)],\end{aligned}$$

*for all $D_1, D_2 \in Der(C)$, which makes $Der(C)$ a Leibniz-Rinehart algebra with the anchor map $T$.*

The action of algebra refers to the application of algebraic structures and operations to analyze mathematical objects and solve problems. Algebraic structures such as groups, rings, fields, and vector spaces provide a framework for understanding symmetries, transformations, and relationships within mathematical systems. The action of algebra is essential in various areas of mathematics and its applications, including physics, cryptography, computer science, and engineering, where algebraic techniques are used for modeling, problem-solving, and optimization. Additionally, algebraic concepts serve as the theoretical foundation for many branches of mathematics, uncovering deep connections and fundamental principles underlying mathematical structures and phenomena.The following definition provides the action of $\mathfrak{g}$, the Leibniz-Rinehart algebra, on $R$, the Leibniz $C$-algebra.

**Definition 2.6.** *Let $\mathfrak{g}$ be a Leibniz-Rinehart algebra and $\Upsilon$ be a Leibniz $C$-algebra. An action of $\mathfrak{g}$ on $\Upsilon$ is a pair of $\mathbb{K}$-bilinear maps*

$$\begin{aligned}&\mathfrak{g}\otimes\Upsilon \longrightarrow \Upsilon, \qquad && \Upsilon\otimes\mathfrak{g} \longrightarrow \Upsilon \\ &(\varsigma, \upsilon) \longmapsto [\varsigma, \upsilon] && (\upsilon, \varsigma) \longmapsto [\upsilon, \varsigma]\end{aligned}$$

*which define a Leibniz action of $\mathfrak{g}$ on $\Upsilon$ in the category of Leibniz $\mathbb{K}$-algebras such that*

$$[\upsilon, c\varsigma] = c[\upsilon, \varsigma],$$

$$[\varsigma, c\upsilon] = c[\varsigma, \upsilon] + \rho_\varsigma(c)\,\upsilon,$$

*for all $c \in C$, $\varsigma \in \mathfrak{g}$ , $\upsilon \in \Upsilon$.*

Let $\mathfrak{g}$ be a Leibniz-Rinehart algebra and $\Upsilon$ be an abelian Leibniz $C$-algebra (i.e. a Leibniz algebra with trivial bracket) on which $\mathfrak{g}$ acts in the category of $\mathbb{K}$-algebras. Then $\Upsilon$ is called a Leibniz-Rinehart representation or a right module over $\mathfrak{g}$. We denote the category of Leibniz-Rinehart modules over $\mathfrak{g}$ by $\mathscr{MOD}_{(\mathfrak{g},C)}$.
Let $\mathfrak{g}$ be a Leibniz-Rinehart algebra and $\Upsilon$ be a Leibniz-Rinehart representation over $\mathfrak{g}$. An abelian extension of $\mathfrak{g}$ by $\Upsilon$ is a split exact sequence

$$0 \longrightarrow \Upsilon \longrightarrow \mathfrak{g}' \overset{s}{\underset{}{\leftrightarrows}} \mathfrak{g} \longrightarrow 0$$

where $\mathfrak{g}'$ is a Leibniz-Rinehart algebra such that the action, which defined by

$$[\varsigma, \upsilon] = [s(\varsigma), i(\upsilon)],$$

$$[\upsilon, \varsigma] = [i(\upsilon), s(\varsigma)],$$

for all $\varsigma \in \mathfrak{g}, \upsilon \in \Upsilon$, of $\mathfrak{g}$ on $\Upsilon$ induced by the extension is the prescribed one.
Let $\mathfrak{g}$ be a Leibniz-Rinehart algebra, $\Upsilon$ be a Leibniz $C$-algebra with an action of $\mathfrak{g}$ on $\Upsilon$. Consider the set $\Upsilon \oplus \mathfrak{g}$ and the bracket

$$\left[(\upsilon, \varsigma), (\upsilon', \varsigma')\right] = \left([\upsilon, \upsilon'] + [\varsigma, \upsilon'] + [\upsilon, \varsigma'], [\varsigma, \varsigma']\right),$$

for all $\upsilon, \upsilon' \in \Upsilon$, $\varsigma, \varsigma' \in \mathfrak{g}$. $\Upsilon \oplus \mathfrak{g}$ is a Leibniz-Rinehart algebra with anchor map

$$\begin{aligned} \widetilde{\rho} \quad : \quad & \Upsilon \oplus \mathfrak{g} \longrightarrow Der(C), \\ & \widetilde{\rho}(\upsilon, \varsigma) = \rho(\varsigma) \end{aligned}$$

. This constructed Leibniz-Rinehart algebra will be called as the semi-direct product of $\Upsilon$ and $\mathfrak{g}$ which will be denoted by $\Upsilon \rtimes \mathfrak{g}$.
Indeed, $\widetilde{\rho}$, is a Leibniz algebra and $C$-module homomorphism. On the other hand,

$$\begin{aligned} [(\upsilon, \varsigma), c(\upsilon', \varsigma')] &= [(\upsilon, \varsigma), (c\upsilon', c\varsigma')] \\ &= ([\upsilon, c\upsilon'] + [\varsigma, c\upsilon'] + [\upsilon, c\varsigma'], [\varsigma, a\varsigma']) \\ &= (c[\upsilon, \upsilon'] + c[\varsigma, \upsilon'] + \rho(\varsigma)(c)\upsilon' + c[\upsilon, \varsigma'], c[\varsigma, \varsigma'] + \rho(\varsigma)(c)\varsigma') \\ &= (c([\upsilon, \upsilon'] + [\varsigma, \upsilon'] + [\upsilon, \varsigma']) + \rho(\varsigma)(c)\upsilon', c[\varsigma, \varsigma'] + \rho(\varsigma)(c)\varsigma') \\ &= (a([\upsilon, \upsilon'] + [\varsigma, \upsilon'] + [\upsilon, \varsigma'], [\varsigma, \varsigma']) + (\rho(\varsigma)(c)\upsilon', \rho(\varsigma)(c)\varsigma') \\ &= a([\upsilon, \varsigma], [\upsilon', \varsigma']) + \widetilde{\rho}(\upsilon, \varsigma)(c)(\upsilon', \varsigma'), \end{aligned}$$

for all $(\upsilon, \varsigma), (\upsilon', \varsigma') \in \Upsilon \rtimes \mathfrak{g}$, $c \in C$, as required.
If $\Upsilon$ is abelian then the canonical embeddings $i_\Upsilon : \Upsilon \longrightarrow \Upsilon \rtimes \mathfrak{L}$, $i_\mathfrak{g} : \mathfrak{g} \longrightarrow \Upsilon \rtimes \mathfrak{g}$, as well as the canonical projection $p_\mathfrak{g} : \Upsilon \rtimes \mathfrak{L} \longrightarrow \mathfrak{L}$ are Leibniz-Rinehart homomorphisms. Consequently, we have the abelian extension

$$\Upsilon \overset{i_\Upsilon}{\rightarrowtail} \Upsilon \rtimes \mathfrak{g} \overset{p_\mathfrak{g}}{\longrightarrow} \mathfrak{g}$$

which splits by $i_\mathfrak{g} : \mathfrak{g} \longrightarrow \Upsilon \rtimes \mathfrak{g}$. The induced representation structure on the kernel from the sequence coincides with the previous one.

**Definition 2.7.** *Let $\mathfrak{g}$ be a Leibniz-Rinehart algebra and $\Upsilon$ be a representation of $\mathfrak{g}$. A derivation from $\mathfrak{g}$ to $\Upsilon$ consists of a map $\delta : \mathfrak{g} \longrightarrow \Upsilon$ such that*

$$\delta(c\varsigma) = c\delta(\varsigma),$$

$$\delta\left([\varsigma, \varsigma']\right) = [\delta(\varsigma), \varsigma'] + [\varsigma, \delta(\varsigma')],$$

*for all $c \in C$, $\varsigma, \varsigma' \in \mathfrak{g}$.*

The set of all derivations from $\mathfrak{g}$ to $\Upsilon$ gives rise to an $C$-module structure which will be denoted by $Der_C(\mathfrak{g}, \Upsilon)$.

**Theorem 2.8.** *There is a 1-1 correspondence between the elements of $Der_C(\mathfrak{g}, \Upsilon)$ and the Leibniz-Rinehart homomorphisms $\sigma : \mathfrak{g} \longrightarrow \mathfrak{g} \rtimes \Upsilon$, for which $p_\mathfrak{g} \circ \sigma = id_\mathfrak{g}$.*

*Proof.* A map $\sigma$ satisfying $p_\mathfrak{g} \circ \sigma = id_\mathfrak{g}$ gives rise to a derivation $\delta_\sigma = p_\Upsilon \circ \sigma : \mathfrak{g} \longrightarrow \Upsilon$. On the other hand, for a given derivation $\delta : \mathfrak{g} \longrightarrow \Upsilon$. we have the Leibniz-Rinehart homomorphism $\sigma_\delta : \mathfrak{g} \longrightarrow \mathfrak{g} \rtimes \Upsilon$, $\varsigma \mapsto (\varsigma, \sigma(\varsigma))$, for all $\varsigma \in \mathfrak{g}$. The maps $\sigma \mapsto \delta_\sigma$ , $\delta \mapsto \sigma_\delta$ are inverse to each other, as required. □

Let $\Upsilon$ be a Leibniz $C$-algebra and $\mathfrak{g}$ be a Leibniz-Rinehart algebra. Let $DO(C, \mathfrak{g}, \Upsilon)$ be the vector space of pairs $(\varphi, \varsigma)$ where $\varphi = (d, D) \in Bider_\mathbb{K}(\Upsilon)$ and $\varsigma \in \mathfrak{g}$ such that

$$d(c\upsilon) = cd(\upsilon) + \rho(\varsigma)(c)\upsilon,$$

$$D(c\upsilon) = cD(\upsilon),$$

for all $c \in C$, $\upsilon \in \Upsilon$. Then the componentwise operations make $DO(C, \mathfrak{g}, \Upsilon)$ a $C$-module and Leibniz $\mathbb{K}$-algebra. In addition, $DO(C, \mathfrak{g}, \Upsilon)$ is a Leibniz-Rinehart algebra where the anchor map defined as the composition of

$$DO(C, \mathfrak{g}, \Upsilon) \overset{pr}{\longrightarrow} \mathfrak{g} \overset{\rho}{\longrightarrow} Der(C),$$

Indeed,

$$[(\varphi, \varsigma), c(\varphi', \varsigma')] \quad = \quad c[(\varphi, \varsigma), (\varphi', \varsigma')] + (\varphi, \varsigma)(c)(\varphi', \varsigma'),$$

for all $c \in C$, $(\varphi, \varsigma)$, $(\varphi', \varsigma') \in DO(C, \mathfrak{g}, \Upsilon)$.

Let $Bider_C(\Upsilon)$ be the Leibniz $C$-algebra of all $C$-biderivations of the Leibniz $C$-algebra $\Upsilon$. Then we have the following exact sequence

$$0 \longrightarrow Bider_C(\Upsilon) \xrightarrow{\beta} DO(C,\mathfrak{g},\Upsilon) \xrightarrow{p} \mathfrak{g},$$

where $p((d,D),\varsigma) = \varsigma$ and $\beta(d,D) = ((d,D),0)$, for all $(d,D) \in Bider_C(\Upsilon)$, $((d,D),\varsigma) \in DO(C,\mathfrak{g},\Upsilon)$.
Let $\mathfrak{g}$ has an action on $\Upsilon$. We have the Leibniz-Rinehart algebra homomorphism $f : \mathfrak{g} \longrightarrow DO(C,\mathfrak{g},\Upsilon)$ which makes

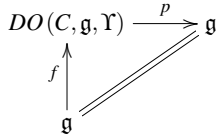


commutative.
For any Leibniz-Rinehart algebra homomorphism $f : \mathfrak{g} \longrightarrow DO(C,\mathfrak{g},\Upsilon)$, $\varsigma \longmapsto (\varphi^{\varsigma},\varsigma)$, the maps $\mathfrak{g} \times \Upsilon \longrightarrow \Upsilon$, $(\varsigma,\upsilon) \longmapsto [\varsigma,\upsilon] := d^{\varsigma}(\upsilon)$ and $\Upsilon \times \mathfrak{g} \longrightarrow \Upsilon$, $(\upsilon,\varsigma) \longmapsto [\upsilon,\varsigma] := D^{\varsigma}(\upsilon)$ defines an action of $\mathfrak{g}$ on $\Upsilon$. Indeed,

$$\begin{aligned} [\varsigma, c\upsilon] &= d^{\varsigma}(c\upsilon) \\ &= d^{\varsigma}(\upsilon) + \varsigma(c)\upsilon \\ &= c[\varsigma,\upsilon] + \varsigma(c)\upsilon \end{aligned}$$

On the other hand, since

$$\begin{aligned} (d^{c\varsigma}, D^{c\varsigma}) &= f(c\varsigma) = cf(\varsigma) \\ &= c(d^{\varsigma}, D^{\varsigma}) \\ &= (cd^{\varsigma}, cD^{\varsigma}) \end{aligned}$$

we have

$$[\upsilon, c\varsigma] = cD^{\varsigma}(\upsilon) = c[\upsilon,\varsigma] \ ,$$

for all $c \in C$, $\upsilon \in \Upsilon, \varsigma \in \mathfrak{g}$, as required.
Various algebraic structures of crossed modules are given in [11]-[21]. Similarly, we have provided our definition of crossed module in the following.

## 3. Crossed Modules of Leibniz-Rinehart Algebras

A crossed module of Leibniz-Rinehart algebras over a base ring $C$ consists of a Leibniz-Rinehart algebra $\mathfrak{g}$, a Leibniz $C$-algebra $\Upsilon$, an action of $\mathfrak{g}$ on $\Upsilon$, and a Leibniz algebra homomorphism $\partial$ from $\Upsilon$ to $\mathfrak{g}$ satisfying certain compatibility conditions. This concept generalizes the notion of crossed modules for Leibniz algebras and provides a framework for studying the interactions between Leibniz-Rinehart algebras. The classification of crossed modules of Leibniz-Rinehart algebras is closely related to the third cohomology of Leibniz-Rinehart algebras, highlighting the deep connection between algebraic structures and cohomological invariants in this setting. The study of crossed modules for Leibniz-Rinehart algebras offers insights into the algebraic and geometric properties of these structures, contributing to a deeper understanding of their behavior and applications in various mathematical contexts.

**Definition 3.1.** *A crossed module $\partial : \Upsilon \longrightarrow \mathfrak{g}$ in the category of Leibniz-Rinehart algebras, which will be called as Leibniz- Rinehart crossed module hereafter, is a homomorphism of Leibniz $\mathbb{K}$-algebras consisting of a Leibniz-Rinehart algebra $\mathfrak{g}$ and a Leibniz $C$-algebra $\Upsilon$ together with an action of $\mathfrak{g}$ on $\Upsilon$ such that*

$$\begin{aligned} &\partial[\varsigma,\upsilon] = [\varsigma,\partial(\upsilon)], \\ &\partial[\upsilon,\varsigma] = [\partial(\upsilon),\varsigma], \\ &[\partial(\upsilon'),\upsilon] = [\upsilon',\upsilon] = [\upsilon',\partial(\upsilon)], \\ &\partial(c\upsilon) = c\partial(\upsilon), \\ &\partial(\upsilon)(c) = 0, \end{aligned}$$

*for all $\upsilon,\upsilon' \in \Upsilon$, $\varsigma \in \mathfrak{g}$, $c \in C$.*

Let $(\mathfrak{g},\rho)$ be a Leibniz-Rinehart algebra. A Leibniz-Rinehart subalgebra $\mathscr{I}$ of $\mathfrak{g}$ is a Leibniz $\mathbb{K}$-subalgebra $\mathscr{I}$, which is a Leibniz-Rinehart algebra with anchor map induced from $\rho$. A Leibniz-Rinehart subalgebra $\mathscr{I}$ of $\mathfrak{g}$ is an ideal if $\mathscr{I}$ is an ideal of $\mathfrak{g}$ as Leibniz $\mathbb{K}$-algebra and the compositions,

$$\mathscr{I} \hookrightarrow \mathfrak{g} \xrightarrow{\rho} Der(C)$$

is trivial.

**Example 3.2.** *Let $\mathfrak{g}$ be a Leibniz-Rinehart algebra and $\mathscr{I}$ is an ideal of $\mathfrak{g}$. Then $(\mathscr{I},\mathfrak{L},\mathrm{inc}.)$ is a crossed module with the actions of $\mathfrak{g}$ on $\mathscr{I}$ defined by*

$$\begin{array}{ccccccc} \mathfrak{g}\times\mathscr{I} & \longrightarrow & \mathscr{I} & \qquad & \mathscr{I}\times\mathfrak{g} & \longrightarrow & \mathscr{I} \\ (\varsigma,\upsilon) & \mapsto & [\varsigma,\upsilon] & & (\upsilon,\varsigma) & \mapsto & [\upsilon,\varsigma]. \end{array}$$

**Proposition 3.3.** *If $\partial : \Upsilon \longrightarrow \mathfrak{g}$ is a crossed module then $Im(\partial)$ is an ideal of $\mathfrak{g}$*

*Proof.* Since $\partial : \Upsilon \longrightarrow \mathfrak{g}$ is a crossed module, we have

$$[\varsigma,\partial(\upsilon)] = \partial[\varsigma,\upsilon],$$

$$\partial[\upsilon,\varsigma] = [\partial(\upsilon),\varsigma]$$

, for all $\upsilon \in \Upsilon$ and $\varsigma \in \mathfrak{g}$. Then $\partial[\varsigma,\upsilon]$, $\partial[\upsilon,\varsigma] \in Im(\partial)$, and $Im(\partial) \trianglelefteq \mathfrak{g}$ □

**Example 3.4.** *Let $\Upsilon$ be a representation over $\mathfrak{g}$. Then the zero morphism $0:\Upsilon\longrightarrow\mathfrak{g}$ is a Leibniz-Rinehart crossed module.*

**Proposition 3.5.** *Let $\partial:\Upsilon\longrightarrow\mathfrak{g}$ be a Leibniz-Rinehart crossed module. Then we have the following:*
*(i) $ker(\partial)\trianglelefteq\Upsilon$*
*(ii) $ker(\partial)$ is a $\mathfrak{g}/\partial(\Upsilon)$-module.*

*Proof.* Direct checking. □

Under the light of this information, we can think Leibniz-Rinehart crossed modules as the generalizations of Leibniz-Rinehart algebras and ideals.

**Example 3.6.** *Let $\mathfrak{g}$ be a Leibniz-Rinehart algebra, $\theta:\Upsilon\longrightarrow\Upsilon'$ be a homomorphism of representations over $\mathfrak{g}$. We have the action of $\Upsilon'\rtimes\mathfrak{g}$ on $\Upsilon$ defined by*

$$\big[(\upsilon',\varsigma),\upsilon\big]=[\varsigma,\upsilon],\ \big[\upsilon,(\upsilon',\varsigma)\big]=[\upsilon,\varsigma],$$

*for all $\varsigma\in\mathfrak{g}$, $\upsilon\in\Upsilon$ and $\upsilon'\in\Upsilon'$. Define*

$$\begin{array}{rcl}\partial:\Upsilon & \longrightarrow & \Upsilon'\rtimes\mathfrak{g}\\ \upsilon & \longmapsto & (\theta(\upsilon),0).\end{array}$$

*Then $(\Upsilon,\Upsilon'\rtimes\mathfrak{g},\partial)$ is a Leibniz-Rinehart crossed module with the defined action of $\Upsilon'\rtimes\mathfrak{g}$ on $\Upsilon$.*

## 4. Conclusion

In this section, the exploration of higher dimensional Leibniz-Rinehart algebras in our article has provided valuable insights into the intricate structures of Leibniz algebroids and their applications. By generalizing the concept of Lie algebroids and incorporating a Leibniz rule for the anchor map, the study has deepened our understanding of connections in algebraic structures. The findings not only pave the way for advancements in the field but also offer a bridge between algebraic and geometric concepts, leading to new insights and discoveries. The study of higher dimensional Leibniz-Rinehart algebras holds promise for further research in areas such as generalized geometry, Poisson geometry, and higher structures, contributing to the ongoing exploration of advanced mathematical theories and applications.

## Article Information

**Acknowledgements:** The authors would like to express their sincere thanks to the editor and the anonymous reviewers for their helpful comments and suggestions.

**Author's contributions:** All authors contributed equally to the writing of this paper. All authors read and approved the finalmanuscript.

**Conflict of Interest Disclosure:** No potential conflict of interest was declared by the authors.



**Supporting/Supporting Organizations:** No grants were received from any public, private or non-profit organizations for this research.

**Ethical Approval and Participant Consent:** It is declared that during the preparation process of this study, scientific and ethical principles were followed and all the studies benefited from are stated in the bibliography.

**Plagiarism Statement:** This article was scanned by the plagiarism program. No plagiarism detected.

**Availability of data and materials:** Not applicable.

## References

[1] J.-L. Loday, *Une version non commutative des algèbres de Lie: les algèbres de Leibniz*, L'Enseignement Mathématique **39** (1993), 269–292.
[2] J.-L. Loday, T. Pirashvili, *Universal enveloping algebras of Leibniz algebras and (co)homology*, Math. Ann., **296** (1993), 139–158.
[3] T. Jubin, Benoî, N. Poncin, K. Uchino, *Free Courant and derived Leibniz pseudoalgebras*, J. Geom. Mech., **8**(1) (2016) 71–97.
[4] A. Aytekin, *Categorical structures of Lie-Rinehart crossed module*, Turkish J. Math., **43**(1) (2019), 511–522.
[5] A. B. Hassine, T. Chtioui, M. Elhamdadi, S. Mabrouk, *Extensions and Crossed Modules of n-Lie-Rinehart Algebras*, Adv. Appl. Clifford Algebr., **32**(3) (2022),31.
[6] J. M. Casas, M. Ladra, T. Pirashvili, *Crossed modules for Lie-Rinehart algebras*, Cent. Eur. Journal of Algebra, **274**(1) (2004) 192–201.
[7] Chen, Liangyun, M. Liu, J. Liu, *Cohomologies and crossed modules for pre-Lie Rinehart algebras*, J. Geom. Phys., **176** (2022)
[8] A. Çobankaya, S. Çetin, *Homotopy of Lie-Rinehart Crossed Module Morphisms*, Adıyaman University Journal of Science, **9**(1) (2019) 202–212.
[9] J. Huebschmann, *Poisson cohomology and quantization*, J. Reine Angew. Math., **408** (1990), 57–113.
[10] J. M. Casas, T. Datuashvili, M. Ladra, *Left-right noncommutative Poisson algebras*, Cent. Eur. J. Math., **12**(1) (2014) 57–78.
[11] M. Alp, B. Davvaz, *Crossed polymodules and fundamental relations*, Politehn. Univ. Bucharest Sci. Bull. Ser. A Appl. Math. Phys., **77**(2) (2015), 129–140.
[12] H. G. Akay, İ. İ. Akça, *Completeness of the category of rack crossed modules*, Ikonion J. Math., **4**(2) (2022), 56–68.
[13] S. Çetin, Utku Gürdal, *A characterization of crossed self-similarity on crossed modules in L-algebras*, Logic Journal of the IGPL, **jzae003** (2024).
[14] J. M. Casas, S. Çetin, E. Ö. Uslu, *Crossed modules in the category of Loday QD-Rinehart algebras*, Homology Homotopy Appl., **22**(2) (2020) 347–366.
[15] S. Çetin, Leibniz-Rinehart cebirleri ve genellemeleri, Phd Thesis, Eskişehir Osmangazi Üniversitesi, Türkiye, (2017)
[16] U. Gürdal, *A Jordan-Hölder theorem for crossed squares*, Kuwait J. Sci., **50**(2) (2023) 83–90.
[17] M. H. Gürsoy, H. Aslan, İ. İcen, *Generalized crossed modules and group-groupoids*, Turkish J. Math., **41**(6) (2017) 1535–1551.
[18] J. Huebschmann, *On the history of Lie brackets, crossed modules, and Lie-Rinehart algebras*, J. Geom. Mech., **13**(3) (2021) 385–402.
[19] O. Mucuk, T. Şahan, *Coverings and crossed modules of topological groups with operations*, Turkish J. Math., **38**(5) (2014) 833–845.
[20] A. Mutlu, *Join for (Augmented) Simplicial Group*, Math. Comput. App., **5**(2) (2000) 105–112.
[21] S. Öztunç, N. Bildik, A. Mutlu, *The construction of simplicial groups in digital images*, J. Inequal. Appl., (2013) 1–13.